Summer 2019

Damage Evaluation of Concrete Structures Using Acoustic Emission

Rafal Anay

DAMAGE EVALUATION OF CONCRETE STRUCTURES USING ACOUSTIC EMISSION

by

Rafal Anay

Bachelor of Science
University of Mosul, 2003

Master of Science
University of Mosul, 2006

Submitted in Partial Fulfillment of the Requirements

For the Degree of Doctor of Philosophy in

Civil Engineering

College of Engineering and Computing

University of South Carolina

2019

Accepted by:

Paul Ziehl, Major Professor

Juan Caicedo, Committee Member

Fabio Matta, Committee Member

John Rose, Committee Member

Cheryl L. Addy, Vice Provost and Dean of the Graduate School

Dedication

To my wife, sons and daughter. To my father and mother

Acknowledgments

This work would have not been achieved without the help, support, and motivation of many people who contributed or accompanied me during this work. It is to them that I owe my deepest gratitude.

First, I would like to express the deepest gratitude to my advisor, Dr. Paul Ziehl who has always guided me during all times and difficulties. His insight and suggestions have always enhanced my thinking of a given problem and allowed me to see it from a different perspective.

I would like to thank my committee members, Dr. Fabio Matta, Dr. Juan Caicedo and Dr. John Rose for their guidance and comments during my research. Special thanks to my fellow graduate students and friends at the University of South Carolina, especially Dr. Mohamed ElBatanouny, Lateef Assi and Vafa Soltangharaei who helped me during my PhD journey. Also special thanks to the civil engineering laboratory manager and lab technician, Russell Inglett and Robert Moore for their support.

The financial support provided by the Iraqi government, U. S. Department of Energy, SCDOT, NMDOT, PCI and NASA are greatly acknowledged.

I thank Mr. Eddie Deaver of Holcim Cement for his support. The technical support provided by Mistras group Inc., Mr. Richard Gostautas, is appreciated.

I owe my deepest appreciation to my wife, Sara. Your love and support have always lighted my way. Thanks to all my family and friends in Iraq and US.

Abstract

The deterioration and aging of the infrastructure in the U.S. have become a crucial issue, especially for highway bridges and nuclear power plants. The reliability and safety of existing structures are affected by growing populations and limited resources. This issue has gained significant concern during the last two decades and efforts are being conducted to accelerate the improvement of nondestructive testing (NDT) and structural health monitoring (SHM) methods. Additional information regarding the condition of existing structures and the early detection of damage can aid in reducing overall maintenance costs. The studies presented in this dissertation employ acoustic emission (AE) as a non-destructive evaluation technique, leveraging its extreme sensitivity to mechanical waves generated by damage and progressive deterioration mechanisms within these structures. The objective of the research is to characterize damage conditions of existing structures using a stress wave-based approach including two cases of study: a) detect and identify the extent of microcrack initiation and progression occurring due to different compressive loading levels applied on small scale cement paste specimens using acoustic emission, and b) monitor and evaluate damage growth in a prestressed concrete girder bridge with shear cracks under truck loading and varying load positions. Three studies were performed in an effort to achieve the objectives and are presented in a series of journal articles as chapters in this dissertation. The first and second studies present a two-part paper which discusses damage mechanisms in cement paste under compression loading based on AE (Part I) and fracture mechanics (Part II). In this study, cement paste specimens having dimension of

38.1 mm x 38.1 mm x 152.4 mm (1.5 in. x 1.5 in. x 6 in.) were cast using Portland cement Type I/II and a water to cement ratio of 0.5, which was then cured for 28 days in lime water. Part I presents and discusses the results from compression tests while monitoring with AE. Active crack growth was detected and classified using amplitude and cumulative signal strength (CSS), and unsupervised pattern recognition was utilized to separate AE data into clusters. Then the source of AE data was verified using micro-CT scanning.

Part II included a three-point bending test conducted on 38.1 mm × 38.1 mm × 152.4 mm (1.5 in. × 1.5 in. × 6 in.) cement paste specimens to measure the fracture toughness property. Also, the compression test of the cement paste prism was simulated using the Abaqus finite element program to determine the stress intensity factor (SIF) along a predefined crack tip at different levels of loading. The SIF is to be compared with the fracture toughness to define the limit at which a crack grows in an unstable manner. The results of this study show that under the conditions of unstable crack extension (defined in Part I by the AE method), the calculated SIF reached the fracture toughness of cement paste. This verifies the defined damage mechanisms described in part I.

In the third study, acoustic emission (AE) data was investigated to better understand damage conditions in a three-span prestressed concrete girder bridge during a load test. The innovation lies in classification of crack extensions (stable or unstable) during the loading and holding processes. The gap in current literature addressed is a paucity of data and findings on bridges in operation and having inclined cracks. This study addresses the collection and processing of AE signals recorded by piezoelectric sensors attached on two interior girders toward the obtuse corner of an exterior span of the bridge while under loading. Results showed signs of crack propagation beyond the existing cracks. Damage

classification procedures based on AE data recorded during one loading and holding step provided an indication of diminishing crack extensions as the load hold was continued in one girder. Concurrently, signs of unstable crack propagation were shown in the other girder. The use of previously developed AE analysis methods to evaluate the condition of each girder is discussed. Finally, shear strength analysis using modified compression field theory (MCFT) was performed to place the results in context.

The outcomes of the studies described in this dissertation demonstrate the potential of using AE as a feasible technique for condition assessment and structural health monitoring through two main points including: a) stress wave-based data acquisition can be used to inform the microscale damage compression model as it relates to the degradation of cement paste, and b) a stress wave based approach may be used to define the level of shear damage in prestressed bridge girders due to applied loading.

Table of Contents

List of Tables

List of Figures

Chapter 1

Introduction

1.1 Background

The deterioration of concrete structures is a crucial issue, especially for highway bridges and nuclear power plants. The quality of life, economic prosperity, and development of communities are all affected by the condition of the local infrastructure. Growing populations and limited resources may influence the reliability and safety of existing structures. Common forms of deterioration, such as cracking in concrete materials are caused by the heterogeneous nature of concrete, its low tensile strength, and severe environments. The condition of the infrastructure can be addressed through the enhancement of resilience and sustainability for new construction and employing active structural health monitoring and maintenance strategies for existing structures.

The 2017 American Society of Civil Engineers (ASCE) Infrastructure Report Card shows that some incremental progress toward restoring the nation's infrastructure has been made. However, more must be done to raise America's cumulative GPA, which was rated D+ as of 2013. Grades of C+ and D were assigned to the conditions of bridges and energy structures in US respectively. Thus, there is a growing need for reliable monitoring techniques with which to assess the state of existing structures. Such assessments may also aid in reducing the overall maintenance costs since postponing maintenance may increase the cost of repairs and ultimately require replacement of the damaged structure.

Structural health monitoring (SHM) is the process of detecting damage and tracking the condition of a structure over time. In the case of infrastructures, damage is defined as a change to the material and/or geometric properties of a structure which adversely affect the structure's performance [1]. The SHM process involves monitoring a structural system using an array of sensors to collect data periodically, the extraction of damage-sensitive

features from this data, and the statistical analysis of these features to determine the current health of the structural system. Depending on the objective of the SHM system and the information of interest, the decision of choosing a local or global monitoring approach is made. For example, global monitoring provides information about the behavior of the structure as a whole, and local monitoring affords information about behavior at critical locations in the structure [2]. Long term SHM provides a historical database regarding the ability of the structure to perform its planned function considering imperative aging and degradation resulting from operational environments or extreme events. Through the system an owner is able to keep abreast of issues such as when certain parameters have reached their preset threshold. Where damages to structures are concerned, there are stages of increasing difficulty that require the knowledge of previous stages. These include detecting and locating the presence of damage to a structure as well as identifying the types of damage and quantifying the severity of the damage. Once this information is collected, signal processing and statistical classification must be performed to translate the sensor data into damage information for assessment.

Several factors may affect the selection of the most appropriate response measurements including the type of structure, inspection data related to the structure's existing condition, cost, availability, ease of installation, accuracy, and resources for data interpretation. Recent advances in technology provide several different solutions for monitoring and assessing the condition of a structure's system. Among those solutions is non-destructive testing (NDT), which uses a passive technique. NDE techniques have been performed in many industries to evaluate the properties of a material, component, or system without impairing its future usefulness or causing damage [3]. Acoustic Emission (AE)

technique, used in this study, is one example of a passive NDT technique defined by ASTM E1316 as “transient elastic waves generated by a rapid release of energy from localized sources within a material” [4]. AE monitoring has the potential to detect and quantify internal damage progression at the microscale level, making it useful for the detection and quantification of damage growth in real time. The high sensitivity of AE sensors makes them capable of detecting cracks long before they are visible. Moreover, this method provides the capability to effectively monitor the internal condition of a structure under increasing loads and can potentially assist in establishing safe load limits [5, 6]. One common challenge associated with AE monitoring and assessment is the proper interpretation of damage (e.g., crack growth events) and distinction from other sources, such as reflections from boundaries, in the data.

1.1.1 Applications of AE in monitoring of nuclear facilities

The treatment and conditioning processes of nuclear waste before disposal are used to convert radioactive waste materials into forms that are suitable for transportation, storage, and final disposal. One of the conditioning processes is cementation (using specially formulated grouts) which provides a means to immobilize radioactive material [7]. Since microcracks in the cement-based materials allow for enhanced leaching and transport of nuclear waste materials, it is important to develop a methodology for detecting and classifying micro and macro cracks as well as understanding where the cracks initiate and in which direction they expand. This will support and enhance the long-term assessments of concrete and reinforced concrete structures used in nuclear facilities.

Degradation of reinforced concrete structures used in the construction of nuclear reactor buildings, spent fuel pools, and related nuclear facilities have been reported over

time [8, 9]. The possible damage mechanisms that adversely affect durability include thermal cracking, corrosion of steel reinforcement, alkali-silica reaction, freeze-thaw cycling, creep and shrinkage and sulfate attack.

Reliable online monitoring of such damage can provide valuable information related to the current state of a structure which is useful to decide whether facility maintenance or shutdown the building is required. For nuclear facilities monitoring, special attentions should be considered due to the safety and relatively long half-life of nuclear waste products [8].

Two main studies have been conducted at the University of South Carolina to explore the feasibility of using AE for the detection and evaluation of damage related to cracking and material degradation in nuclear facilities including 1) Remote monitoring and evaluation of damage at a decommissioned nuclear facility using acoustic emission [8], and 2) Nondestructive evaluation: investigation of acoustic emission technologies for monitoring inaccessible regions of dry fuel storage systems [10]. Based on the outcomes of these studies and the work done on the cement paste prisms [11] during this research, the following recommendations should be considered when monitoring nuclear facilities with AE.

- Conducting a site visit to investigate the condition of a structure visually and to get better idea what to do in the next step.
- Choosing monitoring techniques beside AE such as strain measurement to support AE interpretation if possible.

- Using wireless system with solar power paired with cellular connections for the remote monitoring, makes employing AE method suitable for long-term monitoring efforts.
- Protecting the electrical components from environmental conditions is required especially in humid environments.
- Selecting various AE sensors should be performed to determine which resonant frequencies provide the highest amplitude response, using various artificial sources to simulate cracking activities such as pencil lead breaks.
- Sensors locations are chosen such that both undamaged (control) and damaged areas are covered.
- The environmental effects on AE sensors such as such as temperature variation and radiation should be checked.
- Correlate AE with damage, which is defined based on the structure types and expected mechanisms (e.g. shear wall, dry cask storage system (DCSS) canisters etc.).
- Evaluate the level of damage based on the extensive analysis using experimental data and theoretical models.
- Provide recommendation to decide whether long-term monitoring or shutdown the facility is required.

1.1.2 Applications of AE in monitoring of bridge girders

Although laboratory reinforced and prestressed concrete beam specimens representative of in-service bridges with various configurations and structural details have been tested using AE [12-15], more field tests are needed to develop evaluation criteria for

on-site condition assessment of in-service bridges having inclined cracks and to limit subjectivity in the interpretation of AE data. This document aims to address these gaps as described in the following sections.

1.2 Research Significance

There is a growing need for effective non-destructive tests that can assess the condition of concrete structures. Additional information regarding the condition of existing structures can aid in reducing the overall maintenance cost. This study aims to advance the use of AE as a method of damage evaluation as well as a way to monitor the structural health of concrete structures by detecting and classifying structural damage.

This research targets two of the main challenges associated with AE as a method for structural health monitoring and evaluating damage. The first challenge is verifying the source of AE data collected during compressive loading of cement paste specimens. Micro-CT scanning is employed to investigate the dimensional extent of micro-cracking and to correlate the images with AE data. Additionally, experimental and theoretical investigation of fracture mechanics in cement paste are performed to (1) define the limit at which unstable crack extension and coalescence starts and (2) corelate that to AE data. This can support the efforts that have been exerted to perform long-term evaluations of concrete and reinforced concrete structures used in nuclear waste disposal systems.

The second challenge is investigating AE for field evaluations of prestressed concrete bridge girders that are currently in service and which contain inclined cracks. This challenge was motivated by the lack of information available in existing literature related the use of AE in monitoring existing bridges with inclined cracks. Therefore, it is important to develop a methodology to evaluate the condition of pre-cracked structure elements and

to extrapolate the results collected from the load test to predict future damage. This application establishes the suitability of AE monitoring for field conditions and provides further insight for potential complications.

1.3 Objective

The objective of the research is to characterize damage conditions of existing structures using a stress wave-based approach including two cases of study:

1. Use AE to detect and identify the extent of microcrack initiation and progression caused by different compressive loading levels applied on small scale cement paste specimens.
2. Monitor and evaluate damage growth on a prestressed concrete girder bridge with shear cracks under truck loading and different load positions.

Three studies were performed to target these topics; each study has its own sub-objectives as summarized below.

1.3.1 Identification of damage mechanisms in cement paste based on acoustic emission

Acoustic emission monitoring was applied in an experimental study to identify damage mechanisms and observe microcrack formation of cement paste prisms. Different load levels were applied to observe damage growth and identify different damage mechanisms. The objectives of this study are to:

1. Categorize acoustic emission events based on their amplitude and cumulative signal strength (CSS) to establish a correlation between mechanical damage and acoustic emission activity.

2. Separate the AE data into clusters by employing unsupervised pattern recognition, which are then assigned to different mechanisms.
3. Investigate the source of AE data by utilizing micro-CT scanning to image microcrack and crack formation at the end of each loading test.

1.3.2 Damage mechanisms of cement paste prisms under compression using acoustic emission and fracture mechanics approaches

Experimental and theoretical investigations based on the fracture mechanics approach were performed on cement paste specimens. The objectives are to:

1. Predict crack growth state based on fracture mechanics approaches in conjunction with experimental observations.
2. Identify the correlation between previously defined damage mechnisims (described in the first study) and AE activity.

1.3.3 On-site acoustic-emission monitoring of a prestressed concrete BT-54 AASHTO girder bridge

This study was conducted to monitor and evaluate damage growth of bridge girders with inclined cracks under dump truck loading and different load positions using piezoelectric AE sensors. The objectives of this study are to:

1. Assess the condition of the prestressed concrete bridge girders exhibiting diagonal cracks, particularly since most of them now extend past epoxy injection and some girders have developed new cracks.
2. Offer more field test data of the pre-cracked structure elements due to the lack of available data.
3. Propose a rating method based on AE historic index to relate the AE data to the bridge condition.

4. Expand the defect definitions given in the AASHTO Manual for Bridge Element Inspection (AASHTO 2013) for cracking of prestressed concrete members to more thoroughly evaluate the extent of cracking which is currently based primarily on crack width, as opposed to crack propagation.
5. Extrapolate the results collected from the load test to predict future damage and provide recommendations to the NMDOT for future steps.

1.4 Layout of Dissertation

The dissertation consists of six chapters. In Chapter 2, background information as gathered through a review of available literature regarding acoustic emission (AE) is presented along with additional background of AE damage quantification methods used in this study.

Chapters 3 through 6 were written in paper form and submitted for publication as journal articles. Therefore, some information may be repeated in certain cases.

Chapter 3 and 4 present a two-part paper which discusses damage mechanisms in cement paste under compression loading based on AE (Part I) and fracture mechanics (Part II). In this study, cement paste specimens having dimension of 38.1 mm x 38.1 mm x 152.4 mm (1.5 in. x 1.5 in. x 6 in.) were cast using Portland cement Type I/II (Lafarge Holcim) and water to cement ratio of 0.5, and then cured for 28 days in lime water. Part I titled "Identification of damage mechanisms in cement paste based on acoustic emission" is presented in Chapter 3. In this chapter the results from compression tests while monitoring with AE are presented and discussed. Active crack growth was detected and classified using amplitude and cumulative signal strength (CSS), and unsupervised pattern

recognition was utilized to separate AE data into clusters. Then the source of AE data was verified using micro-CT scanning.

Part II titled "Experimental and theoretical investigation of fracture properties of cement-paste prisms under compression" is presented in Chapter 4. In this chapter, a three-point bending test was conducted on 38.1 mm × 38.1 mm × 152.4 mm (1.5 in. × 1.5 in. × 6 in.) cement paste specimens to measure the fracture toughness property. Also, the compression test of the cement paste prism was simulated using the Abaqus finite element program to determine the stress intensity factor (SIF) along a predefined crack tip at a specific level of loading. The SIF is to be compared with the fracture toughness to define the limit at which a crack grows in an unstable manner. The results of this study show that under the conditions of unstable crack extension (defined in Part I by the AE method), the calculated SIF reached the fracture toughness of cement paste. This verifies the defined damage mechanisms described in the part I.

Chapter 5 is titled "On-site acoustic-emission monitoring of a prestressed concrete BT-54 AASHTO girder bridge", where AE was utilized to evaluate the condition of a three-span, prestressed concrete girder bridge located in Guadalupe County, New Mexico during a load test. The 15-year-old bridge has inclined cracks in four girders of the exterior spans. Some cracks were injected with epoxy, however, most of the cracks extend beyond the epoxy regions, and some girders have developed new cracks. AE data was collected from sensors attached on two girders toward the obtuse corner of an exterior span under different levels of load. The results indicated that interior girder 3 experienced more damage accumulation during load testing than interior girder 2. Additionally, shear strength

analysis using modified compression field theory (MCFT) was performed to place the results in context. The results showed that bridge closure is not necessary.

Chapter 6 summarizes the research conducted in this dissertation and provides the conclusions drawn. Recommendations for future research are also described.

1.5 References

[1] Wikipedia. Structural health monitoring, (accessed 27 January 2019). https://en.wikipedia.org/wiki/Structural_health_monitoring

[2] Abdelrahman, M. A. Evaluation of concrete degradation using acoustic emission: data filtering and damage detection, Doctoral dissertation, (2016) pp. 189.

[3] Cartz, L., Nondestructive Testing, ASM International, (1995).

[4] ASTM., Standard terminology for nondestructive examinations, ASTM E1316, West Conshohocken, PA., 2014.

[5] Olaszek, P., Swit, G., and Casas, J., Proof load testing supported by acoustic emission: an example of application, in: Bridge Maintenance, Safety, Management and Life-Cycle Optimization, Proceedings of the 5th International IABMAS Conf., Philadelphia, USA, 11-15 July 2010.

[6] Anay, R., Cortez, T. M., Jáuregui, D. V., ElBatanouny, M. K., and Ziehl, P., On-site acoustic-emission monitoring for assessment of a prestressed concrete double-tee-beam bridge without plans, Journal of Performance of Constructed Facilities, 30(4), (2015) 04015062.

[7] Rahman, R. O. A., Rakhimov, R. Z., Rakhimova, N. R., Ojovan, M. I., Cementitious materials for nuclear waste immobilization, John Wiley & Sons, (2014) pp. 230.

[8] Abdelrahman, M., ElBatanouny, M., Dixon, K., Serrato, M., & Ziehl, P., Remote monitoring and evaluation of damage at a decommissioned nuclear facility using acoustic emission. Applied Sciences, 8(9), (2018) 1663.

[9] Dolphyn, B. P., Laminar cracking in post-tensioned concrete nuclear containment buildings, Doctoral dissertation, Georgia Institute of Technology, (2016) pp. 487.

[10] EPRI, Nondestructive Evaluation: Investigation of acoustic emission technologies for monitoring inaccessible regions of dry fuel storage systems. EPRI, Palo Alto, CA: 2016. 3002007816

[11] Anay, R., Soltangharaei, V., Assi, L., DeVol, T., and Ziehl, P., Identification of damage mechanisms in cement paste based on acoustic emission, Construction and Building Materials, 164, (2018) 286-296.

[12] ElBatanouny, M. K., Ziehl, P. H., Larosche, A., Mangual, J., Matta, F., and Nanni, A., Acoustic emission monitoring for assessment of prestressed concrete beams, Construction and Building Materials, 58 (2014b) 46-53.

[13] Vidya Sagar, R., Raghu Prasad, B. K., and Sharma, R., Evaluation of damage in reinforced concrete bridge beams using acoustic emission technique, Nondestructive Testing and Evaluation, 27 (2012) 95-108.

[14] Schumacher, T., Higgins, C. C., and Lovejoy, S. C., Estimating operating load conditions on reinforced concrete highway bridges with b-value analysis from acoustic emission monitoring, Structural Health Monitoring, 10 (2011) 17-32.

[15] Shahidan, S., Pulin, R., Bunnori, N. M., and Holford, K. M., Damage classification in reinforced concrete beam by acoustic emission signal analysis, Construction and Building Materials, 45 (2013) 78-86.

Chapter 2

Literature Review

2.1 Introduction

Acoustic emission (AE) is a technique that is increasingly being used in the field of structural integrity assessment. It is defined by the American Society of Testing and Materials [1] as ‘‘the class of phenomena whereby transient elastic waves are generated by the rapid release of energy from localized sources within a material”. The sensitivity of AE for monitoring damage growth makes it promising for the detection and quantification of damage in real time. Moreover, AE monitoring can be used to monitor the internal conditions of a structure under increasing loads and potentially assist in establishing a safe load limit [2]. AE waveforms can be used to calculate parameters based on time domain such as amplitude, rise time, duration, signal strength, counts [1], and others based on frequency domain such as frequency centroid. Figure 2.1 shows a real signal with some of the parameters that are usually measured.

Earlier in AE history, major efforts were applied to investigating the fundamentals of the AE method and exploring its behavior during deformation and fracturing of several materials [3]. The first study using AE was carried out on metals by Josef Kaiser in Germany in 1950. After that, especially in the last two decades, many researchers examined the feasibility of using the acoustic emission technique for assessing the condition of concrete structures and monitoring their structural health. The method can be used for damage detection and localization of carbon fiber composites [4, 5], assessing the condition of existing structures during load tests [6-9], concrete material degradation (such as alkali silica reaction) [10, 11], corrosion of steel in concrete [12, 13], and damage growth in concrete and cementitious materials [14-16]. However, one common challenge associated with AE monitoring and assessment is the proper interpretation of damage (e.g., crack

growth events) and distinction from other sources, such as reflections from boundaries, in the data. This chapter presents a detailed literature review of the main topics of this dissertation.

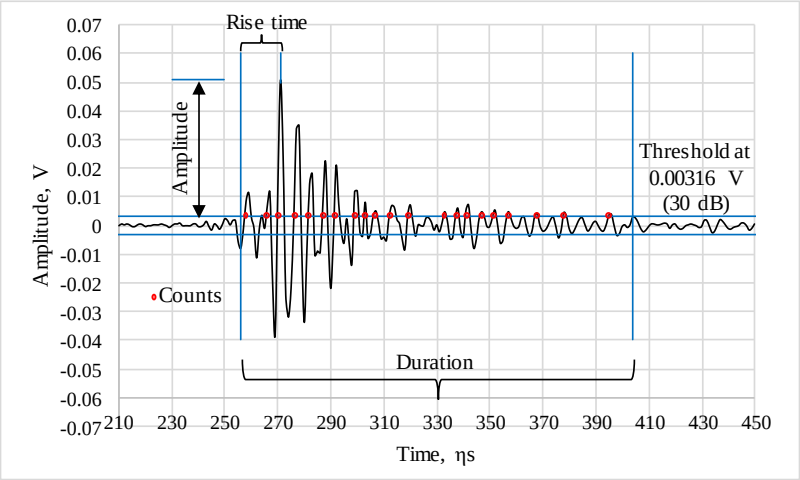

(a) time domain

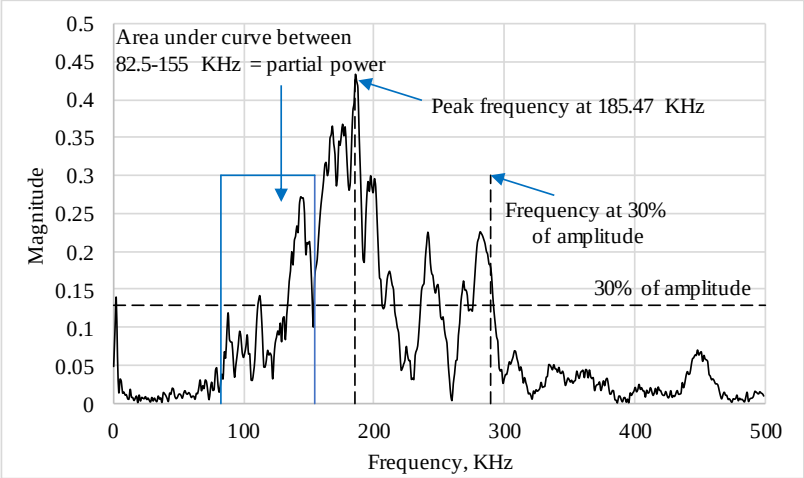

(b) frequency domain

Figure 2.1 Sample of a real signal

2.2 Acoustic Emission Source Location Methods

Several AE source location techniques were developed to enable the localization of damage during load tests including zonal, 2D (planar), and 3D methods. Source

localization techniques are essential in AE analysis to extract the source coordinates of AE events [17]. Location techniques have become an important tool for structural health monitoring (SHM) in research and field applications. AE localization can be applied to all kinds of construction materials [17]. AE sources are located using a known wave velocity in conjunction with the amount of time that it takes for a generated AE signal to reach the sensors [18]. For a source location to be justified, signals must be detected in a minimum number of sensors: one for zonal, two for linear, three for planar and four for volumetric. AE source localization methods, which will be presented in the following sections, were developed based on earthquake seismology with some modifications [17, 19-21]. Knowing the exact origin of an AE wave can help in determining: (1) the source type, such as friction between different parts of a structure, impact damage, etc., (2) evaluating the damage and (3) understanding the damage mechanism and propagation [22].

2.2.1 Zonal and one-dimensional source location

Zonal location is the simplest way to locate the source of AE. The sensor that detects the first arrival or the highest amplitude of the wave is said to be the closest to the source [22], or it just considers the coordinates of the first sensor in the list of hits that make up the event [23]. This method is adequate when the area or sensor spacing being inspected is small or the damage initiation point is known [22]. However, an exact source location determination is not possible. Therefore, it is often used in inspecting large scale structures such as buildings, bridges, and pipes. If AE is recorded by a particular sensor, the technician should look for damage near the sensor [24, 25]. The inspection of the structural element is divided into zones which can be lengths, areas, or volumes depending on the dimensions of the array. The source may be assumed to be within the region and

less than halfway between sensors (one sensor covers each zone). Based on the study conducted by Golaski et al. 2002 [7], it was difficult to assign each recorded signal to a crack because of the large scale of the tested element. Therefore, a zonal location was applied by dividing the tested element into ten measuring areas (one AE sensor/area), and each area was evaluated separately.

Another method uses two sensors to locate an AE source on a line which is called 1D or linear source location. It is a step up from zonal location that performs linear interpolation between two sensors' coordinates based on the differences in the arrival times of the first two hits in the event [23]. Its disadvantage is that in a 2D area limits the source to points on the line segments that connect the sensors when real sources do not face that restriction. However, it is still good enough for the source location of long structures such as pipelines [23].

2.2.2 2D Source location

The next improvement in localization techniques is to perform a 2D source location to determine the x and y coordinates of an AE event. This method is applied when the accuracy of zonal or linear location is not enough. It is also referred to as a planner localization, since no information about the depth of the source is provided (where the thickness of a structure is small compared to the extent of the object) [17]. At least three sensors are needed, assuming there is constant wave velocity at all of them. Once three arrival times of the propagated wave have been measured from the source to the AE sensors, the source can be determined. Sensor layout is an important factor in 2D source location and its effects on the accuracy of the solution. For example, a better solution is to use a layout that minimizes the chances of linear events being observed.

The 2D source location technique has been applied on AE data recorded during laboratory and field load tests. Source triangulation techniques were used to produce crack maps during the load testing of prestressed concrete beams [26]. AE data was recorded using 16 AE resonant sensors (R6i) mounted on each specimen. Extensive scattering in the recorded data due to wave reflections was observed. After filtering, crack maps were developed with a reasonable agreement between AE source location and visually-observed cracks.

AE source localization techniques were applied to the assessment of the condition of a 40-year-old simple-span, prestressed, concrete bridge located in southern New Mexico which had no available design plans [6]. AE data was collected under several loading conditions from two groups of sensors placed near the support and midspan of an interior double-tee beam. A 2D source localization technique using AEwin software [27] was applied to develop crack maps for the instrumented girder (see Figure 2.2) at both shear and moment regions. After applying a Swansong II filter, the AE data indicated that damage in the form of crack growth was more prevalent in the region near the supports than the midspan (Figure 2.3).

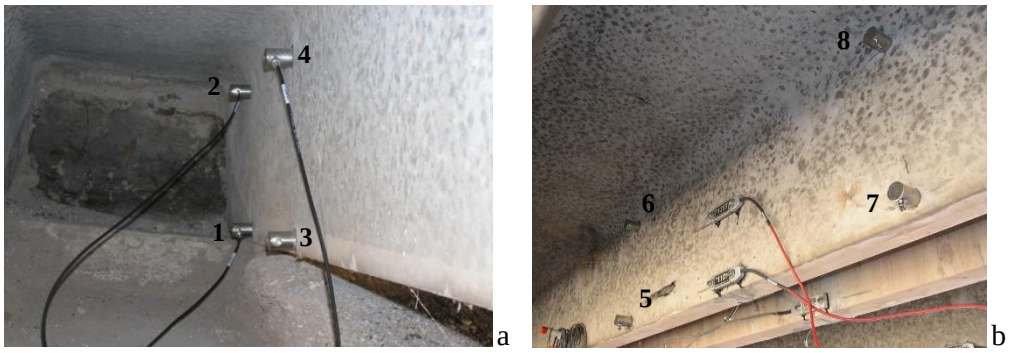

a b

Figure 2.2 AE sensor positions a: photo at support, b: photo at midspan

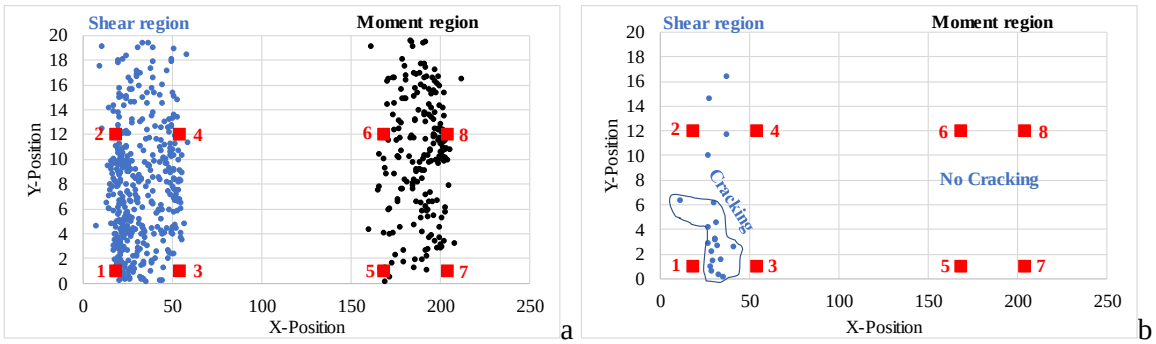

Figure 2.3 AE source location under 4 trucks back to back loading:
(a) unfiltered data; (b) filtered data

2.3 Acoustic Emission Damage Quantification Using Intensity Analysis

Intensity analysis is a method originally developed to classify damage based on AE data in composite pressure vessels [28]. With this method, two parameters (historic index and severity) are calculated based on signal strength. Historic index, H(t), given by function 2a, is sensitive to the change in slope of the CSS curve with respect to time using an historical approach (ratio of the CSS of recent hits to the CSS from all hits). Severity, Sr, is the average of the 50 events having the highest signal strength given by function 2b [7]. Tracking the changes over time of these two parameters provided an indication of the level of damage in a structural element. The intensity analysis chart of AE activity is generated by plotting the severity values versus the maximum historic index (HI) [7]. Events related to increased damage plot toward the top right corner of the intensity analysis chart [7, 26]. Formulas 2a and 2b for HI and severity are given below:

$$H(t) = \frac{N}{N\text{-}K} \frac{\sum_{i=K+1}^{N} S_{oi}}{\sum_{i=1}^{N} S_{oi}} \quad \text{..... (2.1a)}$$

$$S_r = \frac{1}{50} \sum_{i=1}^{i=50} S_{oi} \quad \text{.....(2.2b)}$$

where N = number of hits up to a specific time (t); Soi = signal strength of the ith event; and K = empirically derived constant that varies with the number of hits. The value for K that has been suggested in the literature is as follows [6, 26, 29]: (1) not applicable if $N \leq 50$; (2) $N - 30$ if $51 \leq N \leq 200$; (3) $0.85N$ if $201 \leq N \leq 500$; and (4) $N - 75$ if $N \geq 501$.

Intensity analysis was applied in Anay et al. [6] to quantify the damage of double-tee prestressed concrete bridge girders under two and four trucks back-to-back loading. The results showed that the shear region (at support) experienced more significant damage in the form of crack formation and growth than the moment region (midspan), (see Figure 2.4). Golaski et al. [7] examined the use of intensity analysis under different loading conditions to measure bridge deterioration for different types of bridge construction including reinforced concrete, prestressed concrete, and combined concrete-steel construction. The intensity analysis chart was divided into zones based on the gradation scale and the boundary values of severity and historic index given by Fowler et al. [28] (see Figure 2.5). The general descriptions of the plotted zones are shown in Table 2.1. The colored dots indicate different measuring zones or sensor positions.

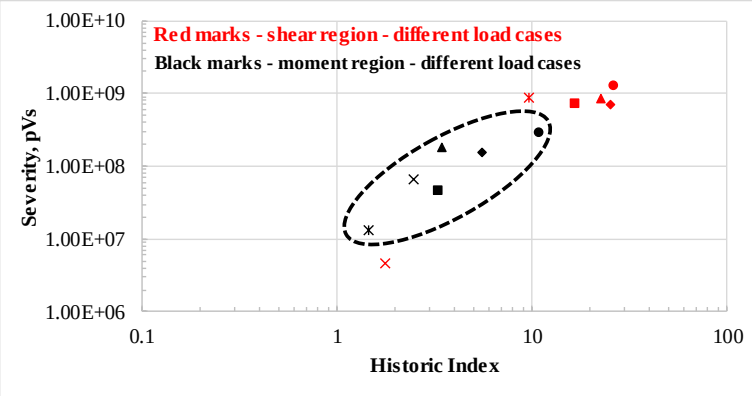

Figure 2.4 Intensity analysis condition assessment under different levels of loading (After Anay et al. 2015 [6])

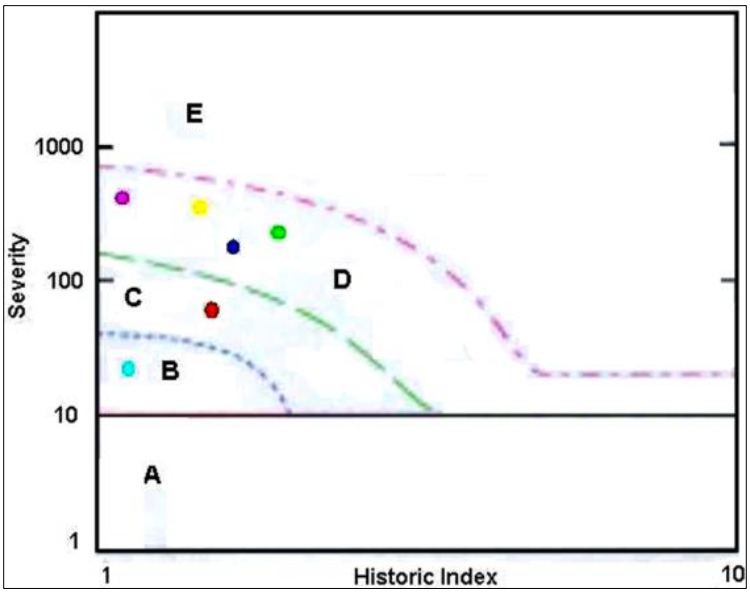

Figure 2.5 Intensity analysis chart of girder tested under different levels of loading [7] (with permission)

Table 2.1 Descriptions of the plotted zones [7]

Zone	Description
A	minor emission, not for further reference
B	"small" defect
C	significant defect, further evaluation required
D, E	major defect, immediate shutdown and follow-up nondestructive examination needed

El-Batanouny et al. [26] performed an intensity analysis to characterize damage in prestressed, T-shaped beams under cyclic loading. The intensity analysis chart was divided into two zones: uncracked (within design criteria) and cracked (failed design criteria). The zones were based on the experimental observation of loading uncracked specimens (Figure 2.6). The method was successful in quantifying existing damage of beams having different initial conditions.

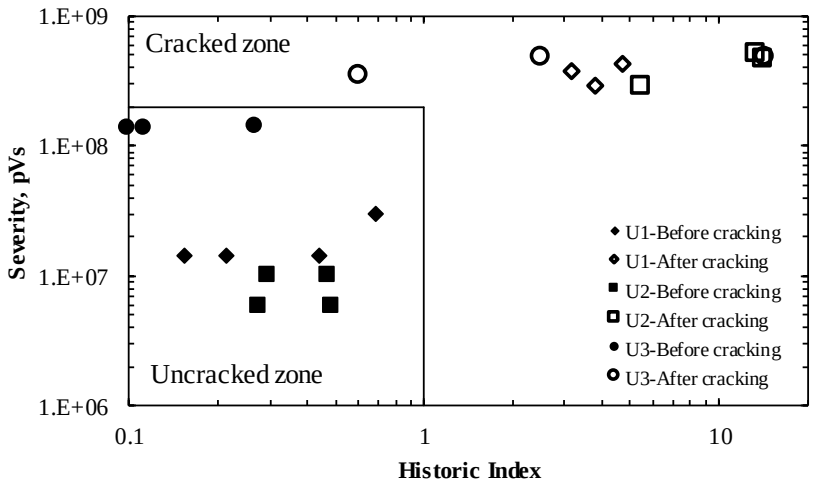

Figure 2.6 Intensity Analysis condition assessment charts of control (pristine) specimens (After ElBatanouny et al. [26])

2.4 Crack Growth Classification Using Acoustic Emission

2.4.1 AE parameters

Damage growth in concrete and cementitious materials have been studied previously through AE monitoring during loading. Sagar et al. [15] investigated the micro-cracking activity and fracture behavior of concrete and cement mortar on notched three-point bending specimens. AE parameters such as event rate, energy release rate, amplitude distribution, cumulative energy, and counts were used in the analysis. It was reported that microcracks initiated and grew at an early stage in mortar before getting to the peak load. For concrete, microcrack growth occurred during the peak load. Three distinct stages of microcrack activity (initiation, stable growth, and nucleation prior to final failure) were observed in both concrete and mortar. Elaqra et al. [16] used AE and 3D X-ray tomography image analysis to identify the mechanisms of damage and the fracture process on mortar specimens. It was reported that Poisson's ratio and cumulative AE counts as a function of stress level could be used to define four different stages (local crack closure, linear elastic behavior, stable crack growth, and unstable crack growth). Puri, S. and Weiss, J. [30]

divided the stress–strain response of concrete cylinders under compression into five different zones and identified them based upon mechanical and acoustic emission characteristics including amplitude and duration. These zones are dispersed microcracking, uniform microcracking, nonuniform damage, the beginning of stiffness degradation, localized damage, and continued compression damage zone to failure. Haneef, T. et al. [31] investigated crack growth behavior of plain and fly ash concretes during uniaxial compression testing using AE parameter analysis including AE counts and amplitude. Three distinct stages of AE activity in both concretes were observed (crack closure/microcracking, steady crack propagation, and unstable crack propagation).

2.4.2 Pattern recognition techniques

Pattern recognition is the automated recognition of patterns by which features in the data are recognized to be used in classifying the data into clusters based on knowledge already gained or on statistical information extracted from patterns.

The procedure consists of three steps including data perception, feature extraction, and classification [32]. Features are derived from the waveform. Some are calculated based on the time domain (measured directly from the waveform) such as amplitude and duration, and others are calculated based on the frequency domain (calculated through signal processing of the waveform) such as frequency centroid. Once features are extracted, the classification process is performed to assign each group to a cluster. There are two classification procedures:

1. When any prior knowledge or labeled database is not available, unsupervised pattern recognition is performed to classify the data into clusters depending on their features and similarities. The number of the clusters has to be defined by

the user to achieve satisfactory results. The most popular unsupervised clustering methods include principal component analysis (PCA) and the k-means algorithm.

2. In many cases, pattern recognition systems are trained from labeled "training" data (supervised pattern recognition), where each new unknown pattern is classified to a predefined cluster. Different supervised classifier algorithms can be used for AE data including K-Nearest Neighbors method (K-NNC), the linear classifier, and the Back Propagation Neural Network.

Cluster analysis has been studied to investigate damage severity and identify damage modes in different structural materials such as cementitious [33–35], composite [36–40] and steel materials [41]. Calabrese et al. [33] applied two types of unsupervised clustering methods: principal component analysis (PCA) and the self-organized map (Kohonen map) for evaluating AE data obtained during 4-point bending tests on concrete beams. It was possible to quantify the damage severity and to identify the evolution of the damage during the test. Calabrese et al. [34] described a multi-step procedure to identify clusters of AE signals recorded during the loading of concrete structures, which could be related to specific damage mechanisms (e.g. tensile cracks, shear cracks, microcracking, or macrocracking). A procedure based on cluster analysis to minimize noise was developed. Farhidzadeh et al. [35] conducted small-scale fracture experiments to impose controlled cracking modes and evaluate the performance of proposed classifiers. The results showed that the classification boundaries for AE features and their associated uncertainties could be successfully estimated. Świt [42] reported the application of AE techniques for identifying active destructive processes and tracking their development during the routine

operation of various types of structures including a steel bridge, steel columns supporting a structure for a cable car, a gas pipeline, and the My Thuan cable-stayed bridge. The recorded AE signals from each field test were grouped into classes to which various mechanisms were assigned based on the structure type using unsupervised and supervised pattern recognition methods.

2.5 Fracture Mechanics

Fracture mechanics is the field of mechanics which deals with fracture and failure processes in engineering materials and constructions [43]. To characterize the material's resistance to fracture, analytical solid mechanics methods are used to calculate the driving force on a crack and those of experimental solid mechanics.

There are three ways of applying a force to enable a crack to propagate defined as follows [43], (Figure 2.7):

1. Mode I: Opening mode (the crack opens perpendicular to the crack plane by tensile loading).
2. Mode II: In-plane sliding mode (the crack faces are displaced on their plane by a shear stress acting parallel to the plane of the crack and perpendicular to the crack front).
3. Mode III: Out-of-plane tearing mode (the crack faces are displaced on their plane by a shear stress acting parallel to the plane of the crack and parallel to the crack front).

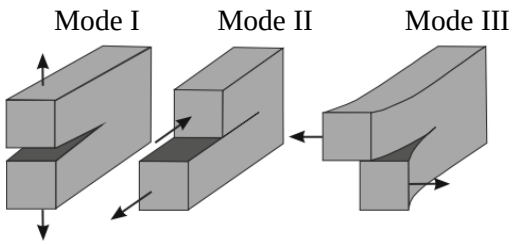

Figure 2.7 Definition of the three-crack opening modes

Since the crack formation and growth in cementitious materials are major mechanisms affecting the strength as well as the durability of the materials and structures, investigation of the mechanical properties of fractures is significant. Studies to determine the fracture properties of concrete were first conducted by Kaplan in 1961 [44]. His study was based on linear elastic fracture mechanics (LEFM), which proposes a single parameter (the critical stress intensity factor K_{IC}). However, several experimental investigations conducted in the 1970s showed that LEFM for quasi-brittle materials such as concrete is no longer valid [45]. This is due to the presence of a relatively large inelastic zone in front of and around the tip of the main cracks in concrete which is ignored by LEFM [46]. Since then, various non-linear fracture mechanics models have been proposed to determine the fracture toughness of concrete materials including the fictious crack model [47], the crack band model [48], the two-parameter model [49, 50], the size-effect model [51], the effect crack model [52-55], and the double-K fracture model [56-58]. The goal of each model is to determine the critical crack extension which depends on the structural size because of its tendency to converge with the initial crack length as the size increases [51]. For this reason, at least two fracture parameters are required for concrete fracture.

2.6 References

[1] ASTM., Standard terminology for nondestructive examinations, ASTM E1316, West Conshohocken, PA., 2016.

[2] Olaszek, P., Swit, G., and Casas, J. Proof load testing supported by acoustic emission: an example of application, in: Bridge Maintenance, Safety, Management and Life-Cycle Optimization, Proceedings of the 5th International IABMAS Conf., Philadelphia, USA, 11-15 July 2010.

[3] Ohtsu, M. The history and development of acoustic emission in concrete engineering. Magazine of concrete research, 48 (1996) 321-330.

[4] Soltangharaei, V., Anay, R., Begrajka, D., Bijman, M., ElBatanouny, M. K., Ziehl, P., & Van Tooren, M. J., A minimally invasive impact event detection system for aircraft movables, In AIAA Scitech 2019 Forum (p. 1268).

[5] Anay, R., Ziehl, P., Tessema, A., Wehbe, R. Y., Assi, L., Kidane, A., ... & Gürdal, Z., An Experimental investigation concerning the effects of AFP defects on progressive failure of tensile coupons, In AIAA Scitech 2019 Forum (p. 1547).

[6] Anay, R., Cortez, T. M., Jáuregui, D. V., ElBatanouny, M. K., and Ziehl, P., On-site acoustic-emission monitoring for assessment of a prestressed concrete double-tee-beam bridge without plans, Journal of Performance of Constructed Facilities, 30 (2015) 04015062.

[7] Golaski, L., Gebski, P., and Ono, K. Diagnostics of reinforced concrete bridges by acoustic emission, Journal of acoustic emission, 20 (2002) 83-89.

[8] Takamine, H., Watabe, K., Miyata, H., Asaue, H., Nishida, T., and Shiotani, T., Efficient damage inspection of deteriorated RC bridge deck with rain-induced elastic wave, Construction and Building Materials, 162 (2018) 908-913.

[9] Świt, G. Acoustic Emission Method for Locating and Identifying Active Destructive Processes in Operating Facilities, Journal of Applied Sciences, 8 (2018) 1-20.

[10] Abdelrahman, M., ElBatanouny, M. K., Ziehl, P., Fasl, J., Larosche, C. J., & Fraczek, J. Classification of alkali–silica reaction damage using acoustic emission: A proof-of-concept study, Construction and Building Materials, 95 (2015) 406-413.

[11] Soltangharaei, V., Anay, R., Hayes, N., Assi, L., Le Pape, Y., Ma, Z., & Ziehl, P. Damage Mechanism Evaluation of Large-Scale Concrete Structures Affected by Alkali-Silica Reaction Using Acoustic Emission, Applied Sciences, 8 (2018) 1-19.

[12] Abdelrahman, M. Assessment of Damage in Concrete Structures Using Acoustic Emission, M.Sc. Thesis, University of South Carolina, (2013) pp. 132.

[13] Yoon, D. J., Weiss, W. J., & Shah, S. P. Assessing damage in corroded reinforced concrete using acoustic emission. Journal of engineering mechanics, 126 (2000) 273-283.

[14] Anay, R., Soltangharaei, V., Assi, L., DeVol, T., & Ziehl, P. Identification of damage mechanisms in cement paste based on acoustic emission, Construction and Building Materials, 164 (2018) 286-296.

[15] Vidya Sagar, R., Prasad, R.V., Raghu Prasad, B.K., Rao, M.V.M.S. Microcracking and fracture process in cement mortar and concrete: a comparative study using acoustic emission technique, Exp. Mech. 53 (2013) 1161-1175.

[16] Elaqra, H., Godin, N., Peix, G., R'Mili, M., Fantozzi, G. Damage evolution analysis in mortar, during compressive loading using acoustic emission and X-ray tomography: Effects of the sand/cement ratio, Cem. Concr. Res. 37 (2007) 703-713.

[17] Grosse, C. U., and Ohtsu, M. (Eds.). Acoustic emission testing. Springer Science & Business Media, 2008.

[18] Goszczyńska, B., Świt, G., Trampczyńsf, W., Krampikowska, A., Tworzewska, J., & Tworzewski, P. Experimental Validation of the Acoustic Emission (AE) Method for the Cracking Process Determination and Location in Concrete Element, In IABSE Symposium Report. International Association for Bridge and Structural Engineering, 99 (2013) 365-372.

[19] Bormann, P. New Manual of Seismological Observatory Practice (NMSOP). Annexes. GeoForschungsZentrum, 2002.

[20] Aid, K., & Richards, P. G. Quantitative seismology: Theory and methods. San Francisco, 1980.

[21] Shearer, P. M. (2009). Introduction to seismology. Cambridge University Press.

[22] Aljets, D., Chong, A., Wilcox, S., & Holford, K. Acoustic Emission Source Location in Plate-Like Structures Using a Closely arranged Triangular Sensor Array, Journal of Acoustic emission, 28 (2010) 85-98.

[23] AEwin Software User Manual Version E5.5, Mistras Group Inc. (2014). http://www.physicalacoustics.com/by-product/aewin/.

[24] Behnia, A., Chai, H. K., and Shiotani, T. Advanced structural health monitoring of concrete structures with the aid of acoustic emission, Construction and Building Materials, 65 (2014) 282-302.

[25] Lovejoy, S. C. Development of acoustic emissions testing procedures applicable to conventionally reinforced concrete deck girder bridges subjected to diagonal tension cracking, Doctoral dissertation, (2006) pp. 534.

[26] ElBatanouny, M. K., Ziehl, P. H., Larosche, A., Mangual, J., Matta, F., and Nanni, A., Acoustic emission monitoring for assessment of prestressed concrete beams, Construction and Building Materials, 58 (2014) 46-53.

[27] AEwin software version e4.30, Mistras Group Inc. (2004). http:// www.physicalacoustics.com/by-product/aewin/.

[28] Fowler, T., Blessing, J., and Conlsk, P., New directions in testing, In AECM-3: International Symposium on Acoustic Emission from Composite Materials, 3rd, Paris, France (1989) 16-27.

[29] Nair, A. and Cai, C. S., Acoustic emission monitoring of bridges: Review and case studies, Engineering structures, 32 (2010) 1704-1714.

[30] Puri, S., Weiss, J. Assessment of localized damage in concrete under compression using acoustic emission, J. Mater. Civ. Eng. 18 (2006) 325-333.

[31] Haneef, T.K., Kumari, K., Mukhopadhyay, C.K., Venkatachalapathy, B.P., Jayakumar Rao, T. Influence of fly ash and curing on cracking behavior of concrete by acoustic emission technique, Constr. Build. Mater. 44 (2013) 342-350.

[32] Abdelrahman, M. A. Evaluation of concrete degradation using acoustic emission: data filtering and damage detection, Doctoral dissertation, (2016) pp. 189.

[33] Calabrese L., Campanella, G., Proverbio, E. Use of cluster analysis of acoustic emission signals in evaluating damage severity in concrete structures, J. Acoust. Emiss. 28 (2010) 129–141.

[34] Calabrese, L., Campanella, G., Proverbio, E. Use of acoustic emission data clustering to identify damage mode in concrete structures, in: Nondestructive Testing of Materials and Structures, Springer, (2013) 329-334.

[35] Farhidzadeh, A., Mpalaskas, A.C., Matikas, T.E., Farhidzadeh, H., Aggelis, D.G.
Fracture mode identification in cementitious materials using supervised pattern recognition of acoustic emission features, Constr. Build. Mater. 67 (2014) 129-138.

[36] Doan, D.D., Ramasso, E., Placet, V., Zhang, S., Boubakar, L., Zerhouni, N. An unsupervised pattern recognition approach for AE data originating from fatigue tests on polymer-composite materials, Mech. Syst. Signal Process. 64-65 (2015) 465-478.

[37] Li, L., Lomov, S.V., Yan, X., Carvelli, V. Cluster analysis of acoustic emission signals for 2D and 3D woven glass/epoxy composites, Compos. Struct. 116 (2014) 286–299.

[38] Li, L., Swolfs, Y. Straumit, I., Yan, X., Lomov, S.V. Cluster analysis of acoustic emission signals for 2D and 3D woven carbon fiber/epoxy composites, J. Compos. Mater. 50 (2016) 1921-1935.

[39] McCrory, J.P., Al-Jumaili, S.K. Crivelli, D., Pearson, M.R., Eaton, M.J., Featherston, C.A., Guagliano, M., Holford, K.M., Pullin, R. Damage classification in carbon fibre composites using acoustic emission: a comparison of three techniques, Compos. Part B Eng. 68 (2015) 424430.

[40] Monti, A., El Mahi, A., Jendli, Z., Guillaumat, L. Mechanical behaviour and damage mechanisms analysis of a flax-fibre reinforced composite by acoustic emission, Compos. Part A Appl. Sci. Manuf. 90 (2016) 100-110.

[41] Envirocoustics, S.A. Pattern recognition techniques for acoustic emission based condition assessment of unfired pressure vessels, Energy. 23 (2005) 318-330.

[42] Świt, G. Acoustic Emission Method for Locating and Identifying Active Destructive Processes in Operating Facilities, Journal of Applied Sciences, 8 (2018) 1-20.

[43] Kuna, M. Finite elements in fracture mechanics, Berlin: Springer, 10 (2013) 978-94.

[44] Kaplan MF, Crack propagation and the fracture of concrete. In Journal Proceedings, 58 (1961) 591-610.

[45] Kesler CE, Naus DJ. Lott LL. Fracture mechanics – its applicability to concrete. In: Proceedings of the international conference on the mechanical behavior of materials, Kyoto, 1971, The Society of Material Science; 4 (1972) 113-24.

[46] Ince, R. Determination of concrete fracture parameters based on two-parameter and size effect models using split-tension cubes. Engineering Fracture Mechanics, 77 (2010) 2233-2250.

[47] Hillerborg A, Modeer M, Petersson PE, Analysis of crack formation and crack growth in concrete by means of fracture mechanics and finite elements, Cement Concr Res 6: (1976) 773-782.

[48] Bazant ZP, Oh BH, Crack band theory for fracture of concrete, RILEM Mater Struct 16 (1983) 155-177.

[49] Jenq Y.S., Shah S.P., A fracture toughness criterion for concrete, Eng Fract Mech 21 (1985a) 1055-1069.

[50] Jenq Y.S., Shah S.P., Two parameter fracture model for concrete, J Eng Mech 111 (1985b) 1227-1241.

[51] Bazant Z.P., Kazemi M.T. Determination of fracture energy, process zone length, and brittleness number from size effect with application to rock and concrete, Int J Fract. 44 (1990) 111-31.

[52] Swartz SE, Go CG, Validity of compliance calibration to cracked concrete beams in bending, Exp Mech. 24 (1984) 129-134.

[53] Swartz SE, Refai TME. Influence of size on opening mode fracture parameters for precracked concrete beams in bending, In: Shah SP, Swartz SE (eds) Proceedings of SEMRILEM international conference on fracture of concrete and rock. Houston, Texas, (1987) 242-254.

[54] Karihaloo BL, Nallathambi P. An improved effective crack model for the determination of fracture toughness of concrete, Cement Concr Res 19: (1989) 603-610.

[55] Karihaloo BL, Nallathambi P., Effective crack model for the determination of fracture toughness (KIc s) of concrete, Eng Fract Mech. 35 (1990) 637-645.

[56] Xu SL, Reinhardt HW. Determination of double−K fracture parameters in standard three-point bending notched beams, In: Mihashi H, Rokugo K (eds) Fracture mechanics of concrete structures, Proc. of FRAMCOS-3. Aedificatio, Freiburg, Germany, 1 (1998) 431-440.

[57] Xu SL, Reinhardt HW. Determination of double−K criterion for crack propagation in quasi-brittle materials, part II: analytical evaluating and practical measuring methods for three-point bending notched beams, Int J Fract. 98 (1999) 151-177.

[58] Xu SL, Reinhardt HW. A simplified method for determining double–K fracture parameters for three-point bending tests, Int J Fract 104 (2000) 181-209.

Chapter 3

Identification of Damage Mechanisms in Cement Paste Based on Acoustic Emission[1]

[1]Anay, R., Soltangharaei, V., Assi, L., DeVol, T., and Ziehl, P. (2018). Identification of damage mechanisms in cement paste based on acoustic emission. *Construction and Building Materials*, *164*, 286-296

3.1 Abstract

Acoustic emission (AE) monitoring during compressive loading was employed to investigate micro-crack formation and coalescence in cement paste specimens. To establish a correlation between damage and AE activity, the data was categorized on the basis of amplitude and cumulative signal strength (CSS). Three distinct stages of crack behavior, illuminated by changes in the slope of the cumulative signal strength versus time relationship, were identified. Micro-crack initiation, crack extension, and unstable crack growth (crack coalescence) were assigned to these stages. An unsupervised pattern recognition approach was employed to separate the data into signal subsets which were then classified and assigned to differing mechanisms. To gain further insight into the crack growth network and behavior, specimens were loaded to varying levels of ultimate capacity and micro-CT scanning was employed to investigate the dimensional extent of micro-cracking and to correlate the images with AE data.

Keywords: Acoustic emission; cement paste; damage mechanism; unsupervised pattern recognition; micro-CT scanning

3.2 Introduction

Concrete is a quasi-brittle material whose properties depend on its constituents, such as cement, aggregate and mineral admixtures. Because of the heterogeneous and multi-scale nature of concrete, several factors play a significant role in its compressive strength including the binder type, aggregate type, extent of the interfacial transition zone, and air content [1]. Researchers have conducted several experiments on cement paste, mortar and concrete to evaluate their behavior under different loading conditions. For example, Choi and Shah [2] have examined fracture processes in cement-based materials

(cement paste, mortar, and concrete) subjected to compressive loading. Material composition and end conditions were found to affect the observed non-uniform deformations at the early stage of loading, and cracks propagated parallel to the loading direction for all specimens.

Micro-cracking in cement-based materials initiates soon after hydration and continues under applied loading. As the load increases, additional cracks form and eventually coalesce and propagate through failure. Micro-crack initiation and damage evaluation of concrete, mortar and cement paste have been studied using nondestructive approaches including ultrasonic pulse velocity and AE. AE, the focus of this study, is defined as "transient stress waves generated by a rapid release of energy from localized sources within a material" [3, 4]. The sensitivity of AE monitoring to damage growth makes it promising for the detection and quantification of damage in real time. Moreover, AE monitoring can be used to monitor internal conditions of a structure under increasing load and potentially assist in establishing a safe load limit [5]. AE waveforms can be used to calculate parameters such as amplitude, rise time, duration, signal strength, and counts [3, 6, 7]. These types of parameters have been previously utilized to provide insight to failure mechanisms at varying stress levels in cement-based materials [8].

Damage growth in concrete and cementitious materials have been studied previously through AE monitoring during loading. Sagar et al. [9] investigated the micro-cracking activity and fracture behavior of concrete and cement mortar on notched three-point bending specimens. It was reported that microcracks initiated and grew at an early stage in a mortar before getting to the peak load. For concrete, microcrack growth occurred during the peak load. Three distinct stages of microcrack activity (initiation, stable growth,

and nucleation prior to final failure) were observed in both concrete and mortar. Elaqra et al. [10] used AE and CT image analysis to identify the mechanisms of damage and the fracture process on mortar specimens. It was reported that Poisson's ratio and AE activities as a function of stress level could be used to define four different stages (local crack closure, linear-elastic behavior, stable crack growth and unstable crack growth). Puri, and Weiss [11] divided the stress–strain response of concrete cylinders under compression into five different zones and identified them based upon mechanical and acoustic emission characteristics (dispersed microcracking, uniform microcracking, nonuniform damage and starting of stiffness degradation, localized damage and continued compression damage zone to failure). Haneef et al. [12] investigated crack growth behavior of plain and fly ash concretes during uniaxial compression testing using AE. Three distinct stages of AE activity in both concretes were observed (crack closure/microcracking, steady crack propagation and unstable crack propagation).

Cluster analysis has been studied to investigate damage severity and identify damage modes in different structural materials such as cementitious [13-15], composite [16-20] and steel materials [21]. Calabrese et al. [13] applied two types of unsupervised clustering methods: principal component analysis (PCA) and the self-organized map (Kohonen map) for evaluating AE data obtained during 4-point bending tests on concrete beams. It was possible to quantify the damage severity and to identify the evolution of the damage during the test. Calabrese et al. [14] described a multi-step procedure to identify clusters of AE signals, recorded during loading of concrete structures, to be related to specific damage mechanisms (e.g. tensile cracks, shear cracks, microcracking, or macrocracking). A procedure based on cluster analysis to minimize noise was developed.

Farhidzadeh et al. [15] conducted small-scale fracture experiments to impose controlled cracking modes and evaluate the performance of proposed classifiers. The results showed that the classification boundaries for AE features and their associated uncertainties could be successfully estimated.

While cluster analysis has been applied to identify damage mechanisms in concrete and cementitious materials in bending, additional work is beneficial to classify damage mechanisms in compression. Moreover, parameters such as amplitude, duration, counts and signal strength have been used to classify AE activity into subsets. This present study addresses detection and classification of microcrack initiation and progression in real time, with focus on two methods: cumulative signal strength and cluster analysis through unsupervised pattern recognition. These methods were utilized to identify the level of damage due to different compressive loading levels. Because cement paste is the binder of cementitious materials, insight into detection of microcrack initiation and growth of cement paste will help to understand the corresponding behavior of mortar and concrete.

Treatment and conditioning processes of nuclear waste before disposal are used to convert radioactive waste materials into forms that are suitable for transportation, storage, and final disposal [22]. One of the conditioning processes is cementation (using specially formulated grouts) which provides a means to immobilize radioactive material [22].

As microcracks in the cement-based materials allow for enhanced leaching and transport of nuclear waste materials, it is important to develop a methodology for detecting and classifying micro and macro cracks and understand in which direction they initiate and expand. This can help for long-term assessments of concrete and reinforced concrete structures used in nuclear waste disposal systems [23].

To explore the potential of AE for detection of microcrack initiation and damage growth, investigations have been conducted on cement paste samples (both during the curing process as well as in the hardened state) including characterization of the hydration process [24] and behavior in compression. This is the motivation to devote our focus to cement paste.

3.3 Materials and Methods

Portland cement Type I/II (Lafarge Holcim) was used. The cement paste specimens were made with water to cement weight ratio of 0.5 and prepared according to ASTM C305 [25]. The mixtures were then cast vertically, to obtain smooth surfaces for better sensors attachment, in 38.1mm × 38.1mm × 152.4mm (1.5 inch × 1.5 inch × 6 inches) acrylic molds and vibrated for ten seconds. After 24 hours, the specimens were taken from the molds and put in lime water for 28 days.

3.4 Experimental Test Setup

Two types of mini-sensors were used; eight micro-30 resonant sensors from MISTRAS Group and two B-1025 broadband sensors from Digital Wave Corp. with an operating frequency range between 150-400 kHz and 50-2000 kHz, respectively. In this study, only the AE data recorded by resonant sensors were selected and post processed due to their high sensitivity. Double bubble epoxy and hot glue were used as the coupling agents to fix the sensors on the surface of the specimens. A thin layer of the epoxy was applied on the specimens to provide a smooth surface. After curing of epoxy for two minutes, a layer of hot glue was applied to fix the sensors in place. Two sensors were attached on each face at 25.4 mm (1") from both ends except for the front face which had two additional sensors attached at 12.7 mm (0.5") from the specimen ends as guard sensors for AE noise filtering.

Stainless steel caps and polyurethane pads with 50.8 mm× 50.8 mm (2" × 2") were used at both ends and the ends of the prisms had smooth, parallel bearing surfaces. A Teflon sheet was used on the top side of the specimens to decrease AE activity caused by friction, as shown in Figure 3.1.

AE signal preamplifiers (type 2/4/6, MISTRAS Group) were used. They were supplied with 20/40/60 dB gain (40 dB was used) and plug-in band pass filters from 100 to 1200 kHz. The AE system used in this experiment was a 16-channel Sensor Highway II (SHII) data acquisition system (Mistras Group, Inc.). AEwin software was used in the data analysis [26]. A background noise check was conducted to identify the threshold, which was set to 30 dB. Pencil lead breaks (PLB) were utilized to check the sensitivity of each sensor and to make sure that the coupling was consistent for all sensors.

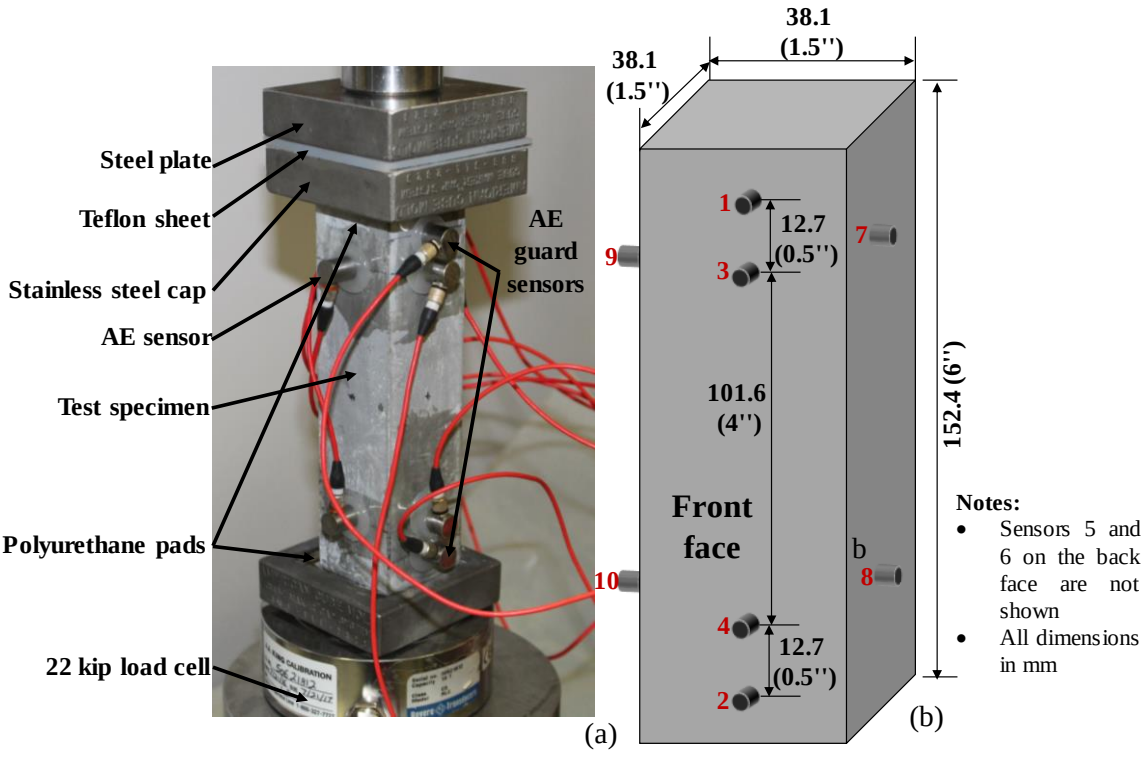

Figure 3.1 Test setup: (a) photograph of test specimen, and (b) sketch of sensors layout

Compression tests were conducted using a material testing system (MTS) of 20-kip capacity with a servo-controlled hydraulic loading frame. The specimens were loaded in displacement control at rate of 0.1 mm/min. Load data was recorded by the 20-kip load cell, which was connected to the Micro-Measurements System 7000 from the Vishay Precision Group. Four specimens (A1, A2, A3 and A4) were loaded to ultimate capacity without attaching AE sensors for three reasons: to observe the critical damage load (a load causes first visible longitudinal crack), to observe crack initiation and progression, and to determine ultimate capacity. The results served as a guide for the second part of the test as the specimens (B60, B80, and B100) were loaded at different percentages, 60%, 80% and 100% of the critical damage load while AE data was recorded. These percentages were chosen depending on the observed behavior of cement paste specimens A1, A2, A3 and A4. Therefore, 6.6 kN (1.5 kip), 8 kN (1.8 kip), and 10.2 kN (2.3 kip) were chosen as maximum loads for the B60, B80 and B100 specimens, respectively.

3.5 Results and Discussion

3.5.1 Cement paste behavior under compression

Behavior of cement paste under compression in terms of crack initiation position, distribution of cracks on the loading surface, and crack propagation along the length is discussed for specimens A1, A2, A3 and A4. Crack identification and classification using signal parameters and data cluster analysis with unsupervised pattern recognition is discussed for specimens B60, B80 and B100.

Load-displacement relationships and modes of failure are shown in Figures 3.2 and 3.3. Cracks initiated from the loading surfaces (either top or bottom) before the peak load and propagated toward the other surface vertically, as cracks in cement paste tend to

propagate parallel to the loading direction [2]. Discrete drops in the load-displacement curves were associated with visible crack initiation and progression. Cracks did not uniformly develop over the loading surfaces. Rather they were concentrated in the corners and side of the loading area, Figure 3.3. The average value of the first visible longitudinal cracking load was 10.5 kN (2370 lb), which was used as a maximum value for the specimens monitored with AE sensors. Due to the use of neoprene pads, the load-displacement relationship began non-linearly, and was followed by a nearly linear relationship up to failure (Figure 3.2). Table 3.1 shows the values of the first visible longitudinal cracking load. The behavior matched the expectations in terms of crack initiation from the top and bottom and surface crack distribution concentrated near the corners.

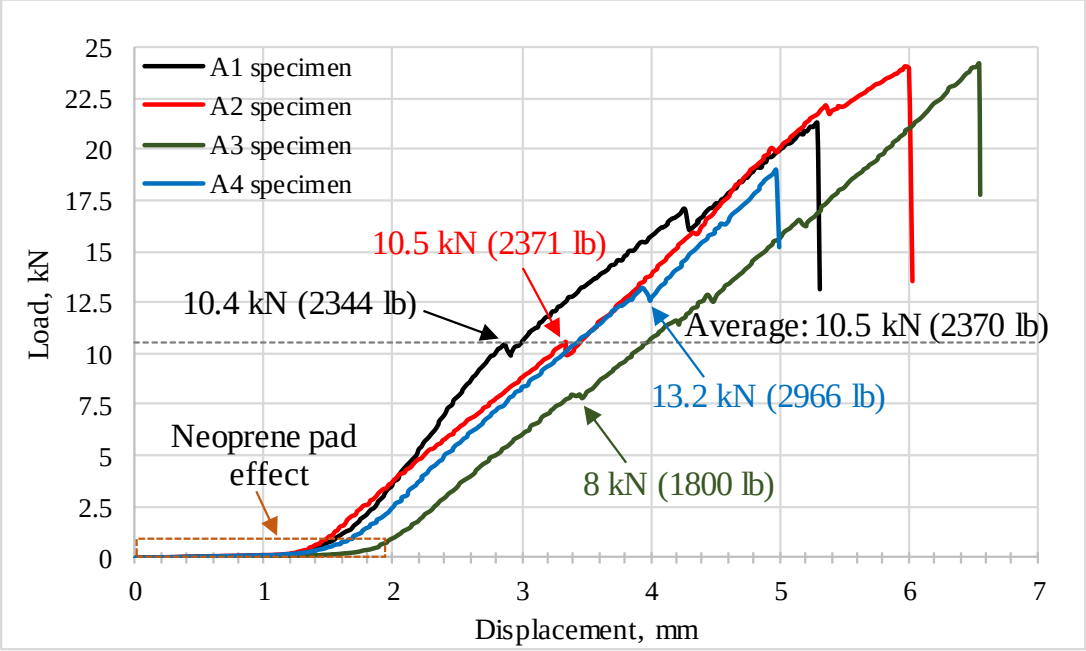

Figure 3.2 Load-displacement relationship

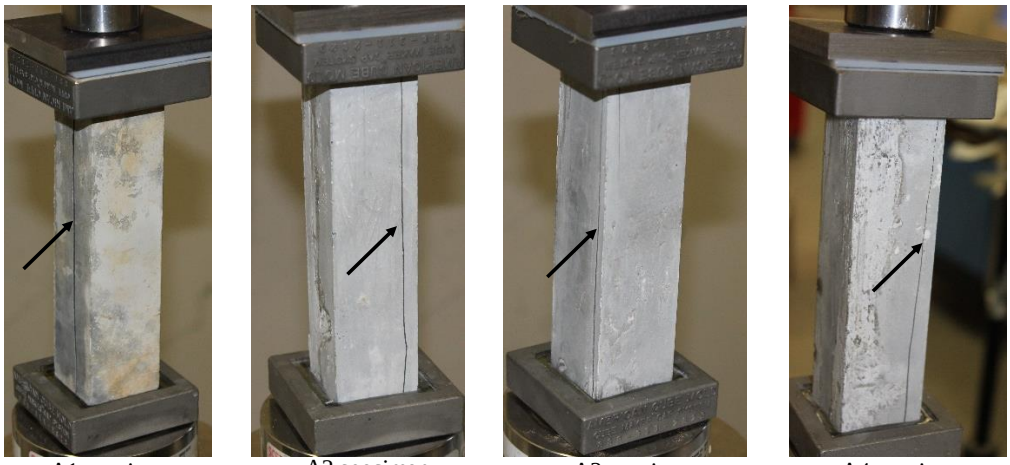

A1 specimen A2 specimen A3 specimen A4 specimen

Figure 3.3 Photographs of failure modes

Table 3.1 Longitudinal cracking load

Specimen ID	**Load, kN (lb)**
A1	10.4 (2344)
A2	10.5 (2371)
A3	8 (1800)
A4	13.2 (2966)
Average	**10.5 (2370)**

3.5.2 Crack identification based on AE

AE data was recorded and post-processed via AEwin [26]. The results for specimens B60, B80 and B100 were analyzed for identification of fracture process stages using AE parameters such as amplitude and signal strength. Figure 3.4 illustrates AE activity versus load in the three specimens. Microcracks initiated and propagated to form visible cracks at the times referenced by the arrows shown in Figure 3.4 for specimens B80 and B100. No visible cracks were seen in the B60 specimen; it is believed that the AE data was due to microcrack initiation and growth. In addition to the several bursts of AE

activities highlighted by arrows, AE activity increased over time during testing of the B80 and B100 specimens, indicating that more micro-crack growth and coalescence occurred throughout the loading. Figure 3.5 shows visible crack networks at maximum applied load for B80 and B100 specimens while no visible crack is seen for B60 specimen.

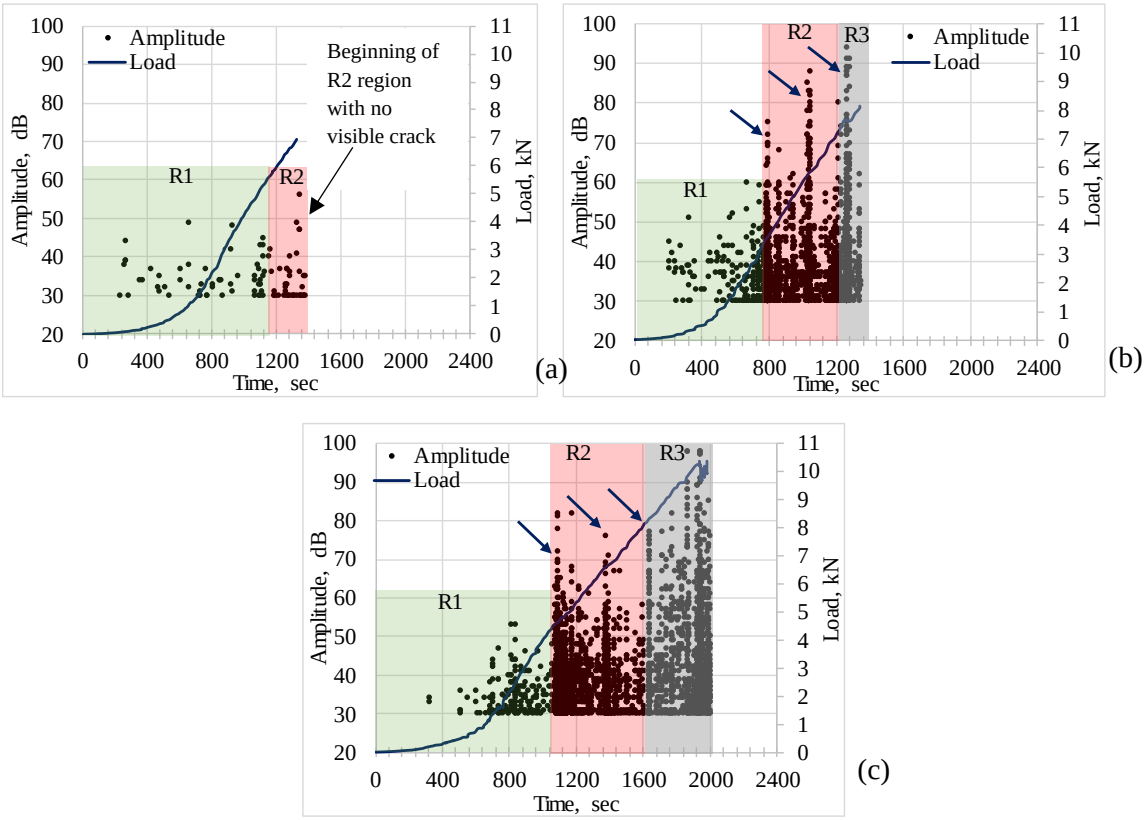

Figure 3.4 AE data activity versus load: (a) B60 specimen, (b) B80 specimen and (c) B100 specimen

3.5.3 Classification of crack growth based on cumulative signal strength

CSS as a function of load is shown in Figure 3.6. The number of AE hits and associated CSS show clearly defined regions as shown in Figures 3.4 and 3.6. Four ranges of crack behavior, illuminated by changes in the slope of the cumulative signal strength curve, can be observed for the B80 and B100 specimens in comparison with only two in the B60 specimen. Significant jumps in CSS compared with the previous stages were observed and used to distinguish between the divided regions in the B80 and B100

specimen, while only one significant jump was observed at the end of B60 specimen test. The jump in AE event rate has been attributed to the localization of micro-cracking and macro-cracking into a single critical crack [27, 28]. The first region (R1), represented by the early stage (elastic deformation stage), showed very little AE activity which can be assigned to micro-crack initiation (no visible crack was seen at this stage). As the load increased, the second region (R2), represented by the stable stage, showed increases in the AE activity due to formation of stable visible cracks for the B80 and B100 specimens. The maximum cracks lengths of approximately 0.85-1 inch were seen at the beginning of this stage and other one of two-inches was observed within this region. Therefore, this region can be assigned to formation and extension of cracks and micro-cracks. At the end of the B60 specimen test, an increase in the rate of AE data was observed and contributed to the beginning of the R2 region as no visible crack was observed. The third region (R3), represented by the unstable stage, showed abrupt increases in AE activity. The maximum crack length of approximately three-inches was observed at the beginning of this stage and propagated to the whole specimen length at the end of this region. This region can be assigned to unstable crack extension and coalescence, leading to eventual failure. Additional evidence is the cracks observed on the samples' surfaces at different times during the test. For example, at the end of the tests, the cracks observed on the surfaces of the B80 specimen showed signs of the beginning of unstable cracks (R3 region) as shown in Figure 3.5b. More and even wider cracks observed on the surfaces of B100 specimen showed unstable cracks that led to specimen failure (Figure 3.5c). The B60 specimen had no evidence of surface cracks during loading (Figure 3.5a), however, minor AE activity and one significant jump in the CSS curve were observed at the end of the test (Figures

3.4a and 3.6a) compared with the B80 and B100 specimens. These activities were attributed to non-visible micro-crack formation which is supported by micro-CT scanning (Figure 3.10).

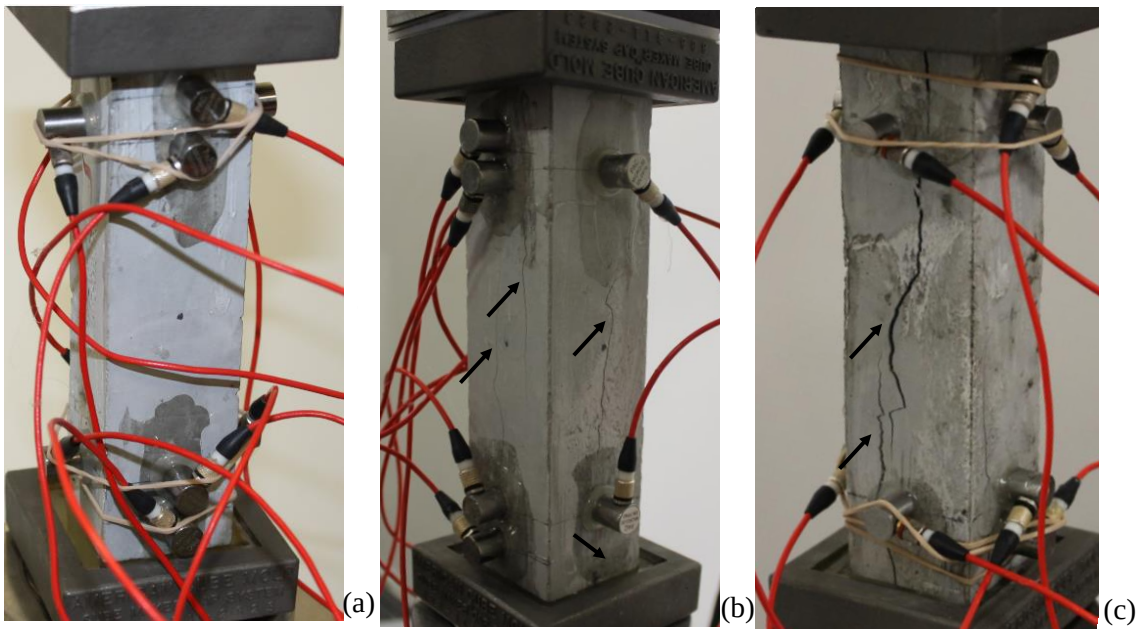

Figure 3.5 Photographs at maximum applied load: (a) B60 specimen, (b) B80 specimen and (c) B100 specimen

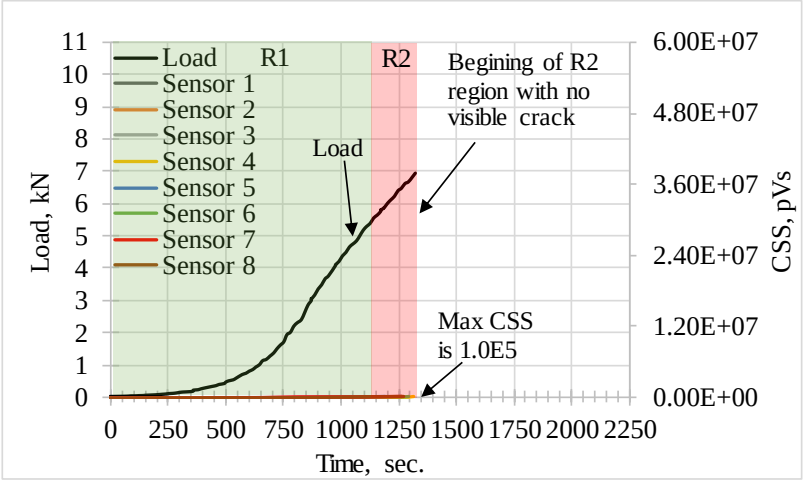

(a) B60 specimen

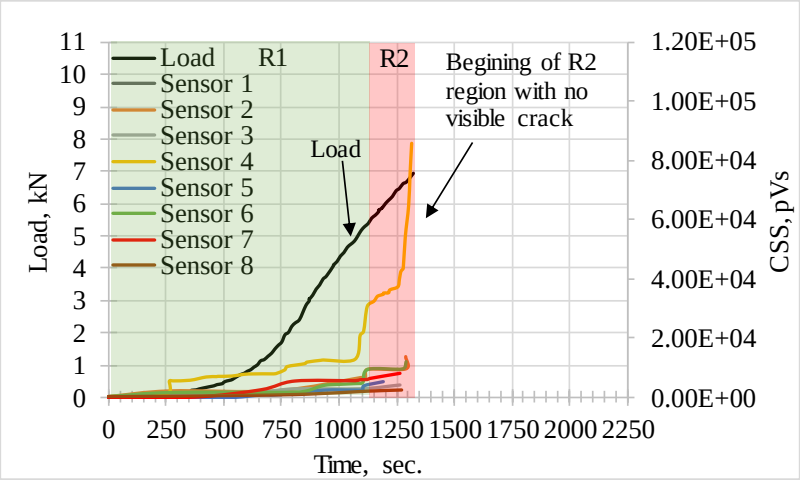

(a') B60 specimen- zoom in of a

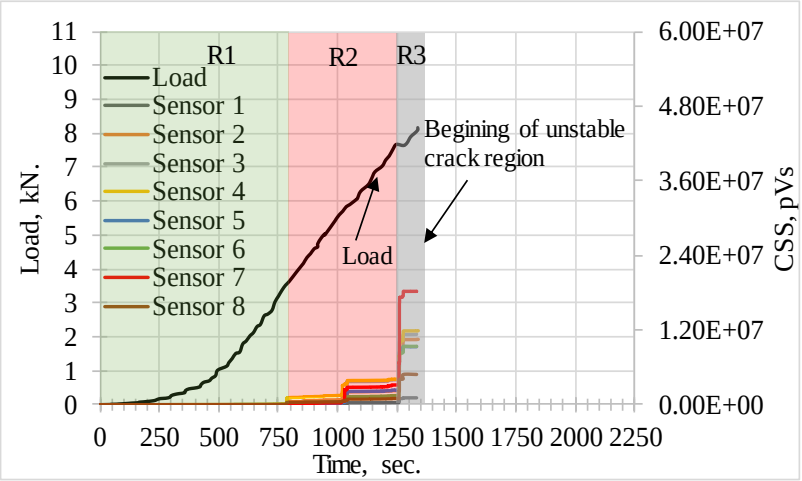

(b) B80 specimen

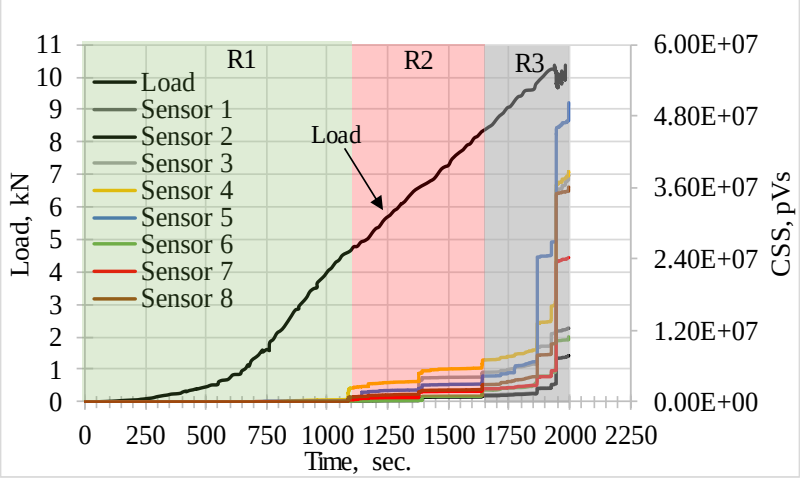

(c) B100 specimen

Figure 3.6 CSS and load versus time

To investigate the properties of AE signals for each assigned mechanism, statistical analysis was conducted on the AE features in each region. The features used were signal strength, counts, duration, amplitude, rise angle value, and average frequency. The averaged feature values are shown in Table 3.2.

Table 3.2 Feature statistics of AE data subsets

Specimen	Time period (sec)	Signal subset	Signal strength (pVs)	Counts	Duration (μs)	Amplitude (dB)	RA value (μs/dB)	Average frequency (kHz)	Number of AE hits
B60	0-1118	R1	3440	3	50	34	0.33	271	52
	1118-1383	R2	2390	5	69	35	0.56	446	48
B80	0-785	R1	2462	5	57	36	0.08	230	200
	785-1260	R2	10989	13	235	38	0.10	196	1674
	1260-1342	R3	48113	38	585	41	0.16	150	829
B100	0-1088	R1	7950	17	288	38	0.12	172	346
	1088-1642	R2	15600	22	357	39	0.17	141	2019
	1642-1998	R3	146000	51	621	45	0.20	141	1224

The average signal strength, counts, duration, amplitude, and rise angle value of AE data in region R1 are lower than regions R2 and R3 for both the B80 and B100 specimens, indicating that the attributed mechanism, microcrack initiation and formation, generates low energy signals at the beginning of the test up to formation of the first visible crack. As the load increases, formation and extension of cracks and micro-cracks followed by unstable crack growth generates higher energy signals. No clear difference of AE

features was observed between the R1 and R2 regions for the B60 specimen as no visible cracks were seen. A parameter-based method using the average frequency versus rise angle value (RA) has been reported to identify cracking mechanisms in concrete structures [29-35]. The two indices are calculated using equations 3.1 and 3.2. The literature indicates that tensile cracks tend to have low RA value and high average frequency with shear cracks being the opposite.

RA = Rise time / Maximum amplitude ……..…….... (3.1)

Average frequency = Counts / Duration ……..……. (3.2)

As shown in Table 3.2, the R1 region has higher average frequency and lower RA value than the R2 and R3 regions (B80 and B100 specimen), which indicates that at the beginning of the compression tests tension cracking occurred, followed by mixed and shear cracks modes.

3.5.4 X-ray micro-CT scanning

Internal imaging using micro-CT scanning was pursued to investigate assumptions discussed in the previous sections. Visualization of two-dimensional images of a specimen surface or thin slices can be obtained through optical or electron microscopy. However, these approaches cannot be used to make a conclusion about the original three-dimensional object in most cases [36]. Landis et al. [37] applied a high-resolution 3D scanning technique called X-ray microtomography to measure internal damage and crack growth in very small mortar cylinders, diameter and thickness of 4 mm (0.15 in), loaded in compression. They found that under increasing load, changes in internal damage can be measured using 3D image analysis techniques. Elaqra et al. [10] used CT image analysis to observe defects of mortar specimen under different compressive loads. They found that

on a meso-scale, X-ray tomography can be used to understand and quantify the general relationship between stress level and crack development in the mortar material. Other techniques such as Magnetic Resonance Imaging (MRI) have been used for 1D, 2D and 3D imaging of cement paste [38-41]. Jaffar et al. [40] discussed the advantages and limitations of imaging mechanically cracked cement paste using MRI. Their results indicated that to obtain high resolution images, the sample size must be very small, about 0.3 mm^3 (1.8e-5 in^3), and the scan time fairly long.

To produce the three-dimensional information, very thin slices are cut to be visualized under the light microscope, then the results of two-dimensional information are interpolated to produce a three-dimensional structure model. This method is slow and not reliable because of the sample preparation technique that can result in a loss of 3D information. In an X-ray (radiography) system, the depth information is mixed, while in an X-ray (tomography) system, complete three-dimensional object structures can be visualized and measured [36]. For these reasons, micro-CT scans were performed using the Burker SkyScan 1176 scanner at Clemson University to visualize micro-cracks and cracks of pre-loaded cement paste specimens. The scans were conducted with a 90 kV, 278 mA X-ray source and a pixel size of 35 µm. During scanning the source-detector pair rotates over 360° with step of 0.7°, and at each position, the shadow image or transmission image was acquired. The reconstruction produced 4651 cross-sectional slice images along the height of the specimen with a size of 1476 by 1476 pixels. The vertical separation between each slice was 0.033 mm (0.001 in). The total time required for scanning and reconstruction was about 3.45 hrs. for each specimen. Figure 3.7 summarizes all actions

and steps to generate the cross-sectional data, and Figure 3.8 shows the scanner and the specimen position in the scanner.

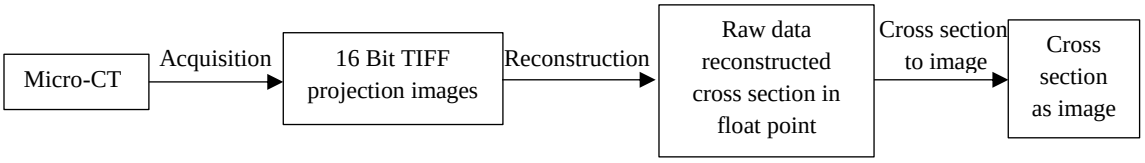

Figure 3.7 Steps of generating the cross-sectional data [36]

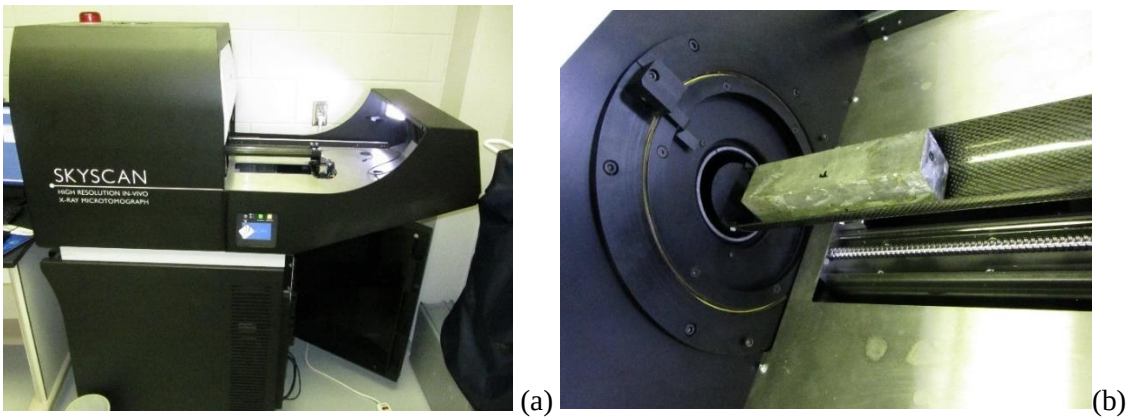

Figure 3.8 X-ray micro-CT scanning: (a) the Burker SkyScan 1176 scanner, (b) specimen position in the scanner

Figure 3.9 shows an example of the slice data at the same cross-sectional plane (at 76.2 mm (3 inches) from the top or from the loading platen surface) of the B0 (control specimen), B60 and B80 specimens. There were no observed micro-cracks or cracks in the B0 specimen, while micro-cracks in the B60, and cracks and micro-cracks in the B80 specimen were detected. Figures 3.10 and 3.11 show micro-CT scan images at different cross-sectional planes of the B60 and B80 specimens respectively. As discussed previously, there were no visible surface cracks in the B60 specimen, and Figure 3.10 shows only internal micro-cracks at different cross-sectional planes. This helps to explain the source of AE data detected during loading (R1 region in Figure 3.4a). Wider and longer cracks were seen in the B80 specimen as the load was higher than the B60 specimen. Some

cracks could be seen by the naked eye on the surface (Figure 3.5b) while others were internal micro-cracks and observed only through the micro-CT scan (Figure 3.11). This also illustrates the reason for detecting more AE data in the B80 than the B60 specimen as shown in Figure 3.4. The bottom right of each image in Figures 3.9, 3.10 and 3.11 represents a zoom in of the selected area.

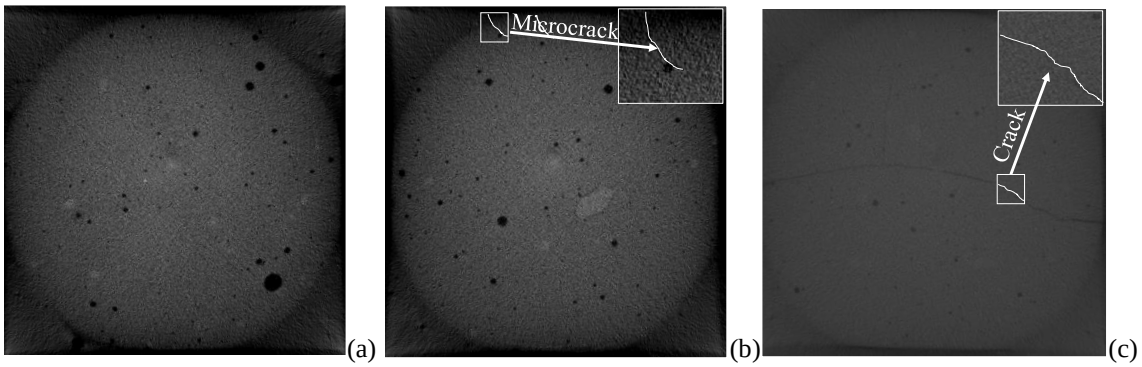

Figure 3.9 Micro-CT scan images of single specimen plane (38.1 mm × 38.1 mm) of (a) B0, (b) B60 and (c) B80 specimen

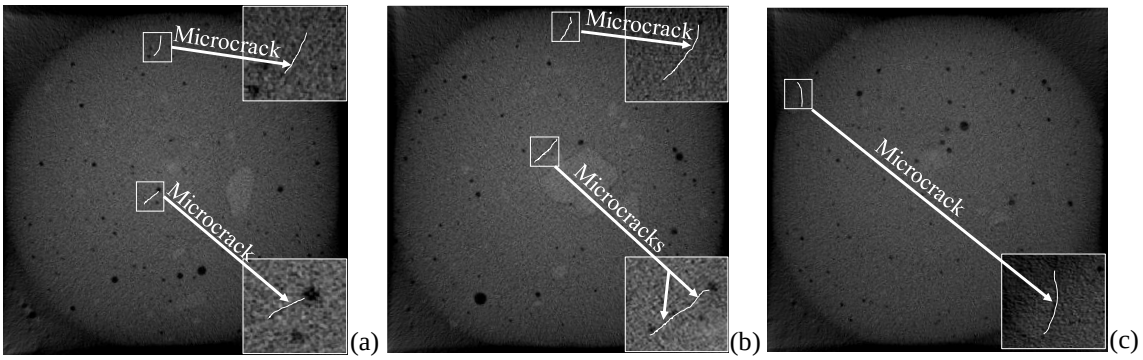

Figure 3.10 Micro-CT scan images at same load but different cross-sectional planes (38.1 mm × 38.1 mm) from the top of B60 specimen: (a) at 16.2 mm (0.64 in), (b) at 64.6 mm (2.5 in) and (c) at 142.5 mm (5.6 in)

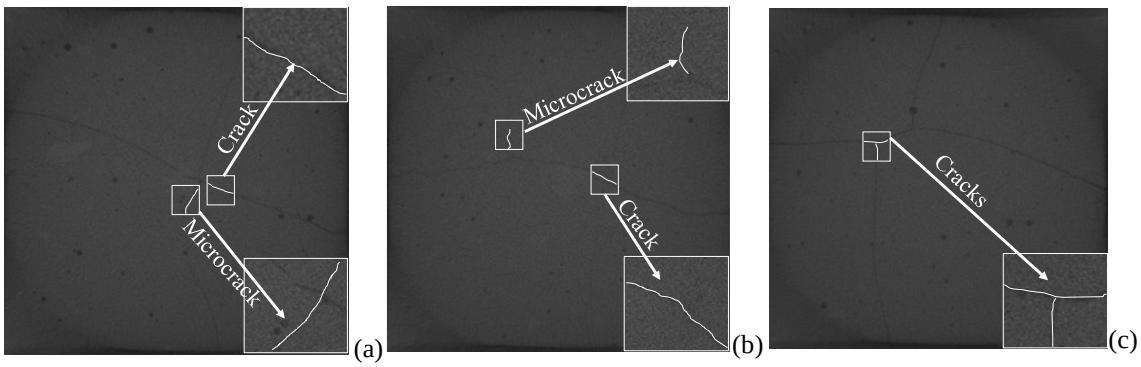

Figure 3.11 Micro-CT scan images at same load but different cross-sectional planes (38.1 mm × 38.1 mm) from the top of B80 specimen: (a) at 25.4 mm (1.0 in), (b) at 59 mm (2.3 in) and (c) at 142.5 mm (5.6 in)

3.5.5 Classification of crack growth using pattern recognition

Pattern recognition was used to cluster the AE data from the B100, B80, and B60 specimens into three signal subsets for each specimen; S1, S2, and S3 for the B100 specimen; T1, T2 and T3 for the B80 specimen; and U1, U2 and U3 for the B60 specimen. Twenty-two features were derived from the AE signals using NOESIS software (AE data analysis pattern recognition & neural networks software). Some were calculated based on the time domain such as amplitude and duration, and others were calculated based on the frequency domain such as frequency centroid. Figure 3.12 shows some of the time domain and frequency domain features. The correlation matrix and correlation hierarchy diagram (Figure 3.13) were employed for selecting the most appropriate features for clustering the data. Low-correlated features can be a good option to use in pattern recognition. Among all features, three low-correlated features were selected for clustering including; energy (*a measure of the area under the rectified signal envelope*), partial power1, PP1 (*power related to the first frequency band width (10-82.5 kHz)*), and Rise Angle value (RA) (*Equation 3.1*). Before post-processing of the data, the feature vector was normalized. A unit variance method was utilized as a normalization technique. Furthermore, principle component

analysis (PCA) was implemented. This method presents the data in a new space with orthogonal axes using eigenvectors of the feature correlation matrix [42]. Therefore, the data was projected into the new axes, made by PCA, with the highest variance. Finally, an unsupervised pattern recognition method was conducted to cluster the data into the subsets. A learning vector quantizer (LVQ) unsupervised neural net in NOISIS was employed as a clustering method. This is a type of "Kohonen" neural net, conceptually similar to the K-Means algorithm [42]. Three resulting clusters for each specimen are shown in Figure 3.14 in the PCA space. The pattern of clusters for the B60, B80 and B100 specimens is similar in the PCA space. Moreover, reasonable discrimination was observed between the signal subsets.

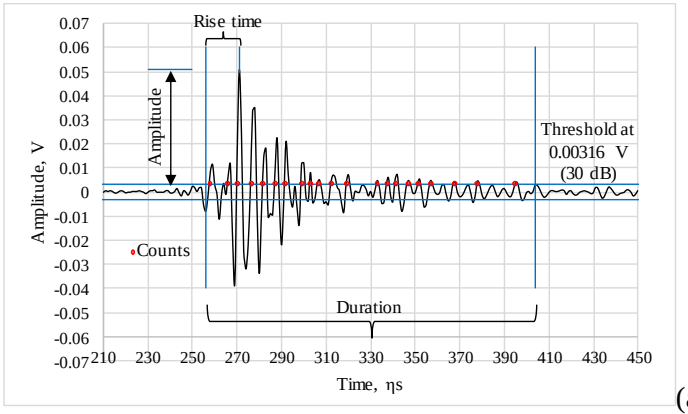

(a)

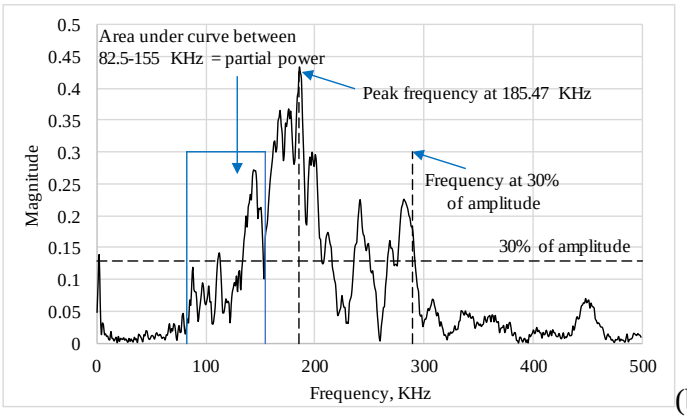

(b)

Figure 3.12 Sample of real signal in: (a) time domain, and (b) frequency domain

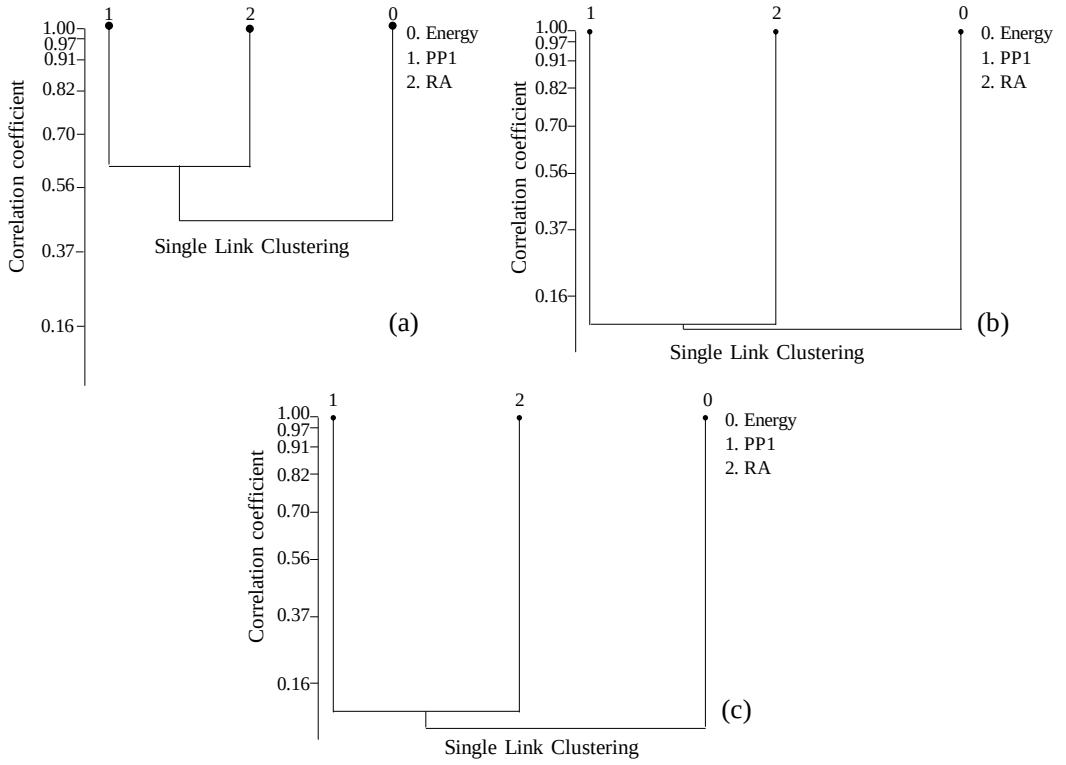

Figure 3.13 Correlation hierarchy diagram for three uncorrelated features: (a) B60 specimen, (b) B80 specimen and (c) B100 specimen

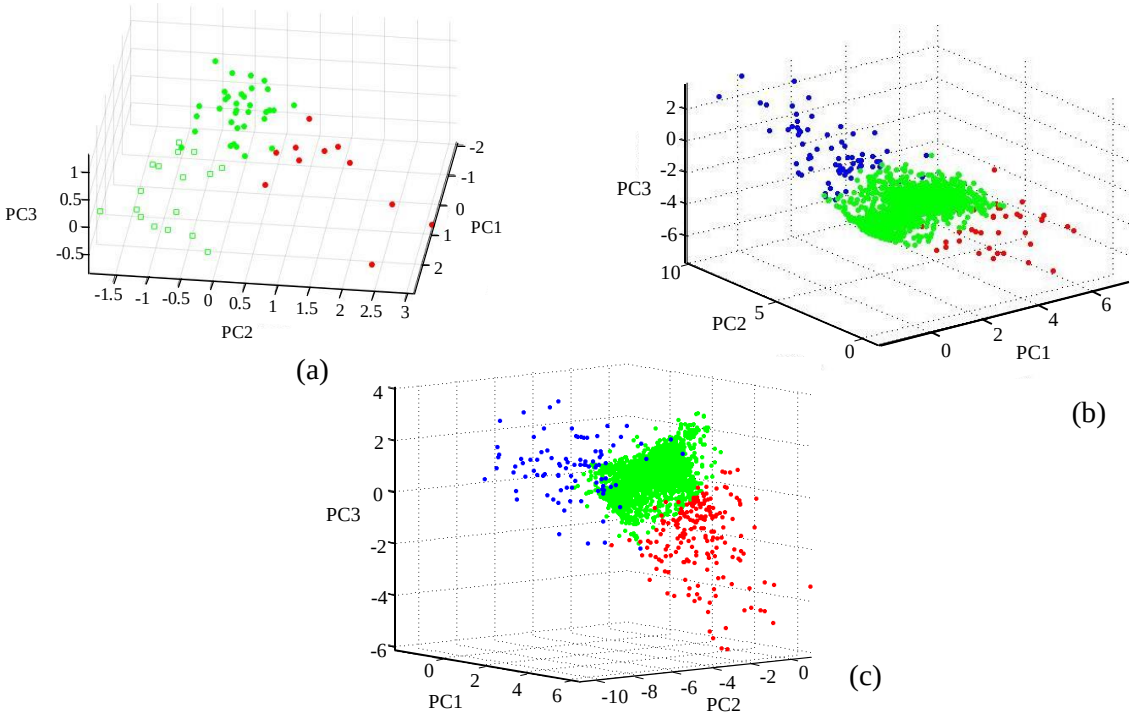

Figure 3.14 AE data clusters in principle component coordinates, a: B60 specimen, b: B80 specimen, c: B100 specimen

Figures 3.15, 3.16 and 3.17 show the amplitude of hits and uniaxial compression loading values versus time for the B100, B80, and B60 specimens. As shown in Figure 3.15, signal subsets S1 and S2 occurred mostly at the end of the loading, at 92% and 75% respectively. The highlighted rectangular area at the end of loading depicts the unstable region for crack formation (R3 in the previous section shown in Figures 3.4 and 3.6). The written percentages in the highlighted rectangular box are ratios of the number of hits for each cluster, occurring in the corresponding time interval, to the whole number of the hits in the related cluster. Most signal subsets S1 and S2 appeared in the highlighted rectangular region. Therefore, these signal subsets should share the characteristics of the assigned mechanisms which are prominent in that time interval. According to the AE data analysis represented by the amplitude and signal strength parameters discussed in the previous section (R3 region), and observations during the experiment, the highlighted rectangular region for S1 and S2 signal subsets represents unstable crack formation and propagation of microcracks (when three-inch crack length was observed and propagated to the whole specimen length). Signal subset S3 did not concentrate at the end of the loading but was distributed more uniformly than signal subsets S1 and S2. Most of the AE activities pertained to signal subset S3 (about 90%). Therefore, the potential assigned mechanism should possess the stated characteristics which are repetitive occurrences within the test period. The attributed mechanism may be micro-crack initiation and growth, which can be expected to occur repetitively over time and appear more than other mechanisms.

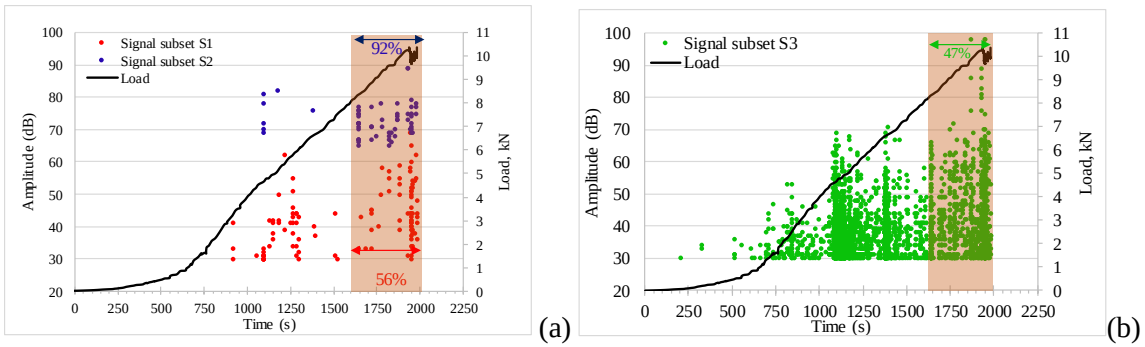

Figure 3.15 Amplitude distribution versus time for the clusters of B100 specimen, a: Signal subsets S1 and S2, b: Signal subset S3

For the B80 specimen, an identical procedure was used for assigning the possible mechanisms. The highlighted rectangular region represents the final stage of loading. This region is associated with the beginning of unstable crack formation (three-inch crack length was observed at the beginning of this stage). The crack growth network was not completed as the load was halted at 80% of expected ultimate capacity. Micro-crack and crack propagation and coalescence are expected as the prominent mechanisms in this region. Signal subsets T1 and T2 concentrate at the end of loading, and their attributed hit percentages (61% and 66%) are much higher than signal subset T3 (33%) in the highlighted region. As for signal subsets S1 and S2, they can be assigned to the potential mechanisms such as micro-crack and crack propagation and coalescence. On the other hand, signal subset T3 is more uniformly distributed in terms of time and quantitatively much than the other signal subsets. Potential damage mechanisms are micro-crack and crack formation. Micro-crack formation is expected to occur more often and in a larger amount in comparison to other mechanisms. In addition, micro-CT images at the end of the B80 specimen test showed micro-cracks and cracks distributed along the specimen with differing lengths and directions (Figure 3.11).

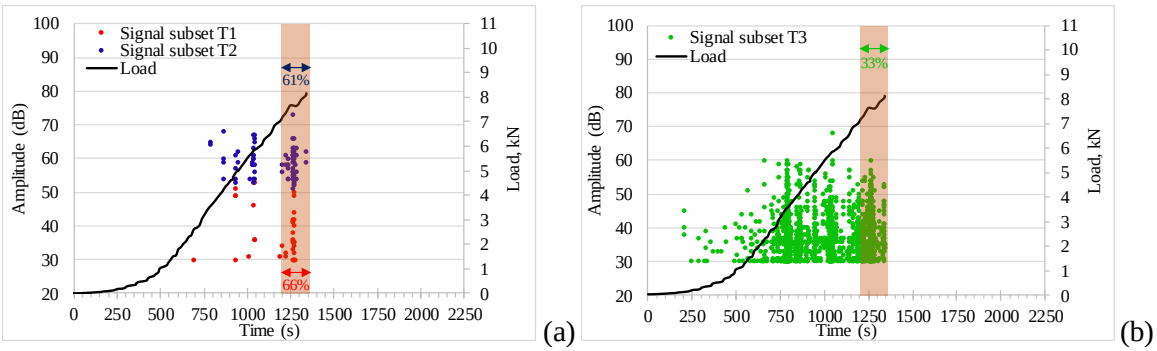

Figure 3.16 Amplitude distribution versus time for the clusters of B80 specimen, a: Signal subsets T1 and T2, b: Signal subset T3

Although less AE data was collected from the B60 specimen (Figure 4), the same clustering procedure for the B80 and B100 specimens was used. Three signal subsets U1, U2, and U3 were clustered as shown in Figures 3.14 and 3.17. Signal subset U1 is concentrated at the end of the loading curve (starting at 1,118 seconds from the beginning of the test) and the attributed hit percentage (100%) is higher than signal subsets U2 and U3 (50% and 25%) in the highlighted region. This region corresponds to the jump in cumulative signal strength at the end of the test (Figure 3.6). In addition, signal subset U1 coincides with the occurrence of part of signal subsets S1 and S2 for the B100 specimen and T1 and T2 for the B80 specimen. The later subsets were previously assigned to the micro and macro-crack propagation and coalescence mechanisms. Since only micro-cracks were formed in the B60 specimen according to the micro-CT images (Figure 3.10), the only related potential mechanism for this subset is micro-crack coalescence. Signal subsets U2 and U3 were distributed more uniformly during the loading, therefore, the potential mechanism for these signal subsets is micro-crack initiation. Micro-CT images indicated that at the end of the B60 specimen test, there were only micro-cracks distributed along the specimen having differing lengths and directions (Figure 3.10).

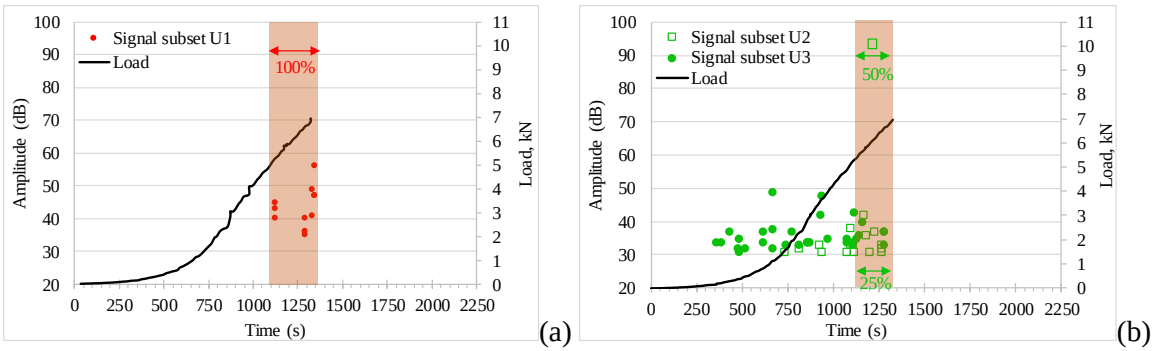

Figure 3.17 Amplitude distribution versus time for the clusters of B60 specimen, a: Signal subset U1, b: Signal subsets U2 and U3

3.6 Conclusion

This study summarizes an experimental approach to detect and classify active crack growth in cement paste specimens. AE data was utilized to guide the investigations and the additional insight was provided by micro-CT scanning at differing levels of ultimate capacity. Conclusions are as follows:

- AE signal parameters such as amplitude and cumulative signal strength were valuable parameters for correlation of mechanical damage and AE activity. Abrupt increases in both parameters correlated to the occurrence of significant damage in the specimens.
- Cumulative signal strength was a useful parameter for detecting crack initiation and progression. Three different mechanisms were defined and assigned, depending on changes in the slope of cumulative signal strength curve. The mechanisms were microcrack initiation and formation, extension of micro-cracks, and unstable crack extension and coalescence.
- Unsupervised pattern recognition showed to be suitable techniques to aid in discrimination between the AE data based on relationships between signal subset

features. The AE data was separated into three signal subsets and fracture mechanisms were then assigned.

- Time of occurrence and statistical criteria were beneficial for assigning potential mechanisms to the signal subsets because different damage mechanisms are more likely to occur in specific time intervals.
- Unstable crack formation and the propagation of micro-cracks was assigned to two signal subsets concentrated near the end of the loading, while micro-crack initiation and formation was assigned to the signal subset distributed throughout the test period for the B80 and B100 specimens.
- Micro-crack coalescence was assigned to a signal subset occurred near the end loading, while micro-crack initiation was assigned to signal subsets distributed throughout the test period of B60. Substantiation of these mechanisms was provided through images obtained through micro-CT scanning, showing only internal micro-cracks distributed along the specimen length.

Finally, the findings were in line with the expectations, however, more tests should be conducted (e.g. three specimens per loading level) to generate more data and observe the signal properties.

3.7 Acknowledgment

This research is based upon work supported by the U.S. Department of Energy Office of Science, Office of Basic Energy Sciences and Office of Biological and Environmental Research under Award Number DE-SC-00012530.

3.8 References

[1] Hlobil, M., Šmilauer, V., & Chanvillard, G. Micromechanical multiscale fracture model for compressive strength of blended cement pastes, Cement and Concrete Research, 83, (2016) 188-202.

[2] Choi, S., & Shah, S. P. Fracture mechanism in cement-based materials subjected to compression, Journal of Engineering Mechanics, 124 (1998) 94-102.

[3] ASTM, ASTM E1316-10b: Standard Terminology for nondestructive examinations, (2013).

[4] Pour-ghaz, M., Spragg, R., Castro, J., Weiss, J. Can acoustic emission be used to detect alkali silica reaction earlier than length change?, 14th Int. Conf. Alkali-Aggregate React. (2012) 1-10.

[5] Olaszek, P., Swit, G., & Casas, J. Proof load testing supported by acoustic emission: an example of application, In Bridge Maintenance, Safety, Management and Life-Cycle Optimization: Proceedings of the Fifth International IABMAS Conference, Philadelphia, USA, 11-15 July 2010 (p. 133). CRC Press.

[6] ElBatanouny, M. K., Ziehl, P. H., Larosche, A., Mangual, J., Matta, F., & Nanni, A. Acoustic emission monitoring for assessment of prestressed concrete beams, Construction and Building Materials, 58 (2014a) 46-53.

[7] Anay, R., Cortez, T. M., Jáuregui, D. V., ElBatanouny, M. K., & Ziehl, P. On-site acoustic-emission monitoring for assessment of a prestressed concrete double-tee-beam bridge without plans, Journal of Performance of Constructed Facilities, 30 (2015) 04015062.

[8] Wu, K., Chen, B., & Yao, W. Study on the AE characteristics of fracture process of mortar, concrete and steel-fiber-reinforced concrete beams, Cement and Concrete Research, 30 (2000) 1495-1500.

[9] Sagar, R. V., Prasad, R. V., Prasad, B. R., & Rao, M. V. M. S. Microcracking and fracture process in cement mortar and concrete: a comparative study using acoustic emission technique, Experimental Mechanics, 53 (2013) 1161-1175.

[10] Elaqra, H., Godin, N., Peix, G., R'Mili, M., & Fantozzi, G. Damage evolution analysis in mortar, during compressive loading using acoustic emission and X-ray tomography: effects of the sand/cement ratio, Cement and Concrete Research, 37 (2007) 703-713.

[11] Puri, S., & Weiss, J. Assessment of localized damage in concrete under compression using acoustic emission, Journal of materials in civil engineering, 18 (2006) 325-333.

[12] Haneef, T. K., Kumari, K., Mukhopadhyay, C. K., Rao, B. P., & Jayakumar, T. Influence of fly ash and curing on cracking behavior of concrete by acoustic emission technique, Construction and Building Materials, 44 (2013) 342-350.

[13] Calabrese, L., Campanella, G., & Proverbio, E. Use of cluster analysis of acoustic emission signals in evaluating damage severity in concrete structures. Journal of Acoustic Emission, 28 (2010) 129-141.

[14] Calabrese, L., Campanella, G., & Proverbio, E. Use of acoustic emission data clustering to identify damage mode in concrete structures. In Nondestructive Testing of Materials and Structures. Springer, (2013) 329-334.

[15] Farhidzadeh, A., Mpalaskas, A. C., Matikas, T. E., Farhidzadeh, H., & Aggelis, D. G. Fracture mode identification in cementitious materials using supervised pattern recognition of acoustic emission features, Construction and Building Materials, 67 (2014) 129-138.

[16] Doan, D. D., Ramasso, E., Placet, V., Zhang, S., Boubakar, L., & Zerhouni, N. An unsupervised pattern recognition approach for AE data originating from fatigue tests on polymer-composite materials, Mech. Syst. Signal Process. 64–65 (2015) 465-478.

[17] Li, L., Lomov, S. V., Yan, X., & Carvelli, V. Cluster analysis of acoustic emission signals for 2D and 3D woven glass/epoxy composites, Compos. Struct. 116 (2014) 286–299.

[18] Li, L., Swolfs, Y., Straumit, I., Yan, X., & Lomov, S. V. Cluster analysis of acoustic emission signals for 2D and 3D woven carbon fiber/epoxy composites, J. Compos. Mater. 50 (2016) 1921-1935.

[19] McCrory, J. P., Al-Jumaili, S. K., Crivelli, D., Pearson, M. R., Eaton, M. J., Featherston, C. A., ... & Pullin, R. Damage classification in carbon fibre composites using acoustic emission: A comparison of three techniques, Compos. Part B Eng. 68 (2015) 424-430.

[20] Monti, A., El Mahi, A., Jendli, Z., & Guillaumat, L. Mechanical behavior and damage mechanisms analysis of a flax-fibre reinforced composite by acoustic emission, Compos. Part A Appl. Sci. Manuf. 90 (2016) 100-110.

[21] Anastasopoulos, A. Pattern recognition techniques for acoustic emission-based condition assessment of unfired pressure vessels, Energy. 23 (2005) 318-330.

[22] Rahman, R. O. A., Rakhimov, R. Z., Rakhimova, N. R., & Ojovan, M. I. Cementitious materials for nuclear waste immobilization, John Wiley & Sons, (2014) pp. 230.

[23] Phung, Q. T., Maes, N., Jacques, D., De Schutter, G., & Ye, G. Investigation of the changes in microstructure and transport properties of leached cement pastes accounting for mix composition, Cem. Concr. Res. 79 (2016) 217-234.

[24] Assi, L., Soltangharaei, V., Anay, R., Ziehl, P., & Matta, F. Unsupervised and supervised pattern recognition of acoustic emission signals during early hydration of Portland cement paste, Cem. Concr. Res. 103 (2017) 216-225.

[25] ASTM International, ASTM C305: Standard practice for mechanical mixing of hydraulic cement pastes and mortars, Am. Soc. Test. Mater. (2011) 13-15.

[26] AEwin software version e4.30, Mistras Group Inc. (2004). http://www.physicalacoustics.com/by-product/aewin/

[27] Li, Z., & Shah, S. P. Localization of moikrocracking in concrete under uniaxial tension, ACI Mater. J. 91 (1994) 372-381.

[28] Landis, E. N., & Shah, S. P. The influence of microcracking on the mechanical behavior of cement based materials, Adv. Cem. Based Mater. 2 (1995) 105-118.

[29] Shiotani, T. Application of the ae improved b-value to quantitative evaluation of fracture process in concrete-materials, Journal of acoustic emission 19 (2001) 118-133.

[30] Ohtsu, M. Okamoto, T., Yuyama, S. Moment tensor analysis of acoustic emission for cracking mechanisms in concrete, Aci Struct. J. 95 (1998) 87-95.

[31] Ohno, K., Ohtsu, M. Crack classification in concrete based on acoustic emission, Constr. Build. Mater. 24 (2010) 2339-2346.

[32] Ono, K., Ohtsu, M. A generalized theory of acoustic emission and green's functions in a half space, Journal of Acoustic Emission 3 (1984) 27-40.

[33] Aggelis, D.G. Classification of cracking mode in concrete by acoustic emission parameters, Mech. Res. Commun. 38 (2011) 153-157.

[34] Aggelis, D. G., Mpalaskas, A. C., Ntalakas, D., & Matikas, T. E. Effect of wave distortion on acoustic emission characterization of cementitious materials, Constr. Build. Mater. 35 (2012) 183-190.

[35] ElBatanouny, M. K., Larosche, A., Mazzoleni, P., Ziehl, P. H., Matta, F., & Zappa, E. Identification of Cracking Mechanisms in Scaled FRP Reinforced Concrete Beams using Acoustic Emission, Exp. Mech. 54 (2014b) 69-82.

[36] BURKER, SkyScan 1176 In vivo X-Ray Microtomography Instruction Manual, 2011. http://www.bruker.com/

[37] Landis, E. N., Nagy, E. N., Keane, D. T., & Nagy, G. Technique to Measure 3D Work-of-Fracture of Concrete in Compression, J. Eng. Mech. 125 (1999) 599-605.

[38] Beyea, S. D., Balcom, B. J., Bremner, T. W., Prado, P. J., Cross, A. R., Armstrong, R. L., & Grattan-Bellew, P. E. The influence of shrinkage-cracking on the drying behaviour of White Portland cement using Single-Point Imaging (SPI)., Solid State Nucl. Magn. Reson. 13 (1998) 93-100.

[39] Bogdan, M., Balcom, B. J., Bremner, T. W., & Armstrong, R. L. Armstrong, Single-Point Imaging of Partially Dried, Hydrated White Portland Cement, J. Magn. Reson. Ser. A. 116 (1995) 266-269.

[40] Jaffer, S. J., Lemaire, C., Hansson, C. M., & Peemoeller, H. MRI: A complementary tool for imaging cement pastes, Cem. Concr. Res. 37 (2007) 369-377.

[41] Young, J. J., Szomolanyi, P., Bremner, T. W., & Balcom, B. J. Magnetic resonance imaging of crack formation in hydrated cement paste materials, Cem. Concr. Res. 34 (2004) 1459-1466.

[42] Mistras Group Hellas ABEE, NOISIS, Advanced Acoustic Emission Data Analysis Pattern Recognition and Neural Networks Software for Acoustic Emission Applications, 11th Edition, 2012. http://www.mistrasgroup.gr/

Chapter 4

Damage Mechanisms of Cement Paste Prisms Under Compression Using Acoustic Emission and Fracture Mechanics Approaches [2]

[2]Anay, R., Soltangharaei, V., Assi, L., & Ziehl, P. Damage mechanisms of cement paste prisms under compression using acoustic emission and fracture mechanics approaches. To be submitted to the journal of *Construction and Building Materials* (2019).

4.1 Abstract

In previous work, acoustic emission (AE) monitoring during compressive loading was employed to investigate microcrack formation and coalescence in cement paste specimens [1]. Three distinct stages of crack behavior were identified based on AE data parameter analysis and experimental observations. Different damage mechanisms were assigned to these stages including microcrack initiation, crack extension, and unstable crack growth. To identify the the correlation between damage mechanisms and AE activity, theoretical predictions on crack propagation were made based on fracture mechanics approaches and the finite element method in conjunction with experimental observations. The fracture toughness of cement paste was determined using the two parameter fracture model based on the experimental results of a three-point bending test. Stress intensity factor (SIF) of mode I, KI, was calculated using the finite element model of cement paste prism under compression and compared to its critical value or fracture toughness (FT) to define the stage of unstable crack growth. The results showed that KI passed the FT of cement paste when unstable crack propagation was observed based on AE data analysis, while it was less than the FT when the first visible crack was initiated and propagated in a stable manner. This work shows that AE and the fracture mechanics approach are complementary methods to characterise damage sites in cement-based materials.

Keywords: Acoustic emission; cement paste; damage mechanism; facture mechanics; finite element

4.2 Introduction

Concrete is a quasi-brittle material. Several factors such as the binder type, aggregate type, extent of the interfacial transition zone, and air content play a significant

role in its compressive strength. In cement-based materials, micro-cracking initiates soon after hydration and continues under applied loading. Additional cracks form and eventually coalesce and propagate through failure as the load increases. Because cement paste is the binder of cementitious materials, insight into detection of microcrack initiation and growth of cement paste will help with understanding the corresponding behavior of mortar and concrete. More details about the motivation to devote our focus to cement paste can be found in [1].

Nondestructive approaches such as acoustic emission (AE) have been employed to investigate microcrack initiation and damage evaluation of concrete, mortar, and cement. AE, the focus of this study, is a technique that is being used increasingly in the field of structural integrity assessment defined by the American Society of Testing and Materials, ASTM E1316 [2] as ‘‘the class of phenomena whereby transient elastic waves are generated by the rapid release of energy from localized sources within a material”. In the last two decades, the feasibility of AE techniques has been investigated for condition assessment and structural health monitoring of concrete structures. The method can be used for detecting microcracks that develop during loading as well as those caused by concrete material degradation such as the corrosion of steel in concrete [3, 4], alkali silica reaction [5, 6], or a combination of the two. AE waveforms can be used to extract parameters based on the time domain such as amplitude, rise time, duration, signal strength, counts [2], and others based on frequency domains such as frequency centroid. These types of parameters have been previously utilized to provide insight to failure mechanisms at varying stress levels in cement-based materials [7].

Different stages of damage growth in concrete and cementitious materials have been defined based on AE data analysis and verified by several methods including mechanical response during loading, X-ray tomography, and SEM micrographs of the fracture surfaces. The micro-cracking activity and fracture behavior of concrete and cement mortar on notched three-point bending specimens were investigated by Sagar et al. [8]. The AE statistical parameters were used to identify and characterize the various stages of micro-cracking activity. The parameters included (1) the occurrence rate of event and energy counts, (2) amplitude distribution (b-value) and its stress-induced changes, and (3) cumulative energy or event counts. Three distinct stages of microcrack activity were observed in both concrete and mortar including initiation, stable growth, and nucleation prior to final failure. In the other study, the stress–strain response of concrete cylinders under compression was divided into five different zones [9]. These zones were identified based upon mechanical and acoustic emission characteristics. The zones identified are dispersed microcracking, uniform microcracking, nonuniform damage with the beginning of stiffness degradation, localized damage, and continued compression damage zone to failure.

Other studies have used different techniques to verify the damage mechanisms assigned to AE data recorded during compression. X-ray tomography was used to identify the mechanisms of damage and the fracture process during compressive loading on mortar specimens [10]. 3D X-ray tomography image analysis was employed to observe defects of mortar specimens under different compressive loads. It was reported that X-ray tomography, strain gauges data, and acoustic emission can be used to better understand and quantify the general relationship between stress levels and crack development in the mortar

material. Four different stages of damage mechanisms were defined: 1. local crack closure, 2. linear-elastic behavior, 3. stable crack growth, and 4. unstable crack growth. In the other study, crack growth behavior of plain and fly ash concretes during uniaxial compression testing was investigated using AE along with the support of SEM micrographs of the fracture surfaces [11]. Three distinct stages of AE activity in both concretes were observed. They are: crack closure/microcracking, steady crack propagation, and unstable crack propagation.

Since the crack formation and growth in cementitious materials is one of the major mechanisms affecting the strength as well as the durability of the materials and structures, investigation of fracture mechanical properties is significant. In general, material separation is better described by energy principles rather than by stress or strain [12]. The toughness estimated by the area under the stress-strain curve of the material cannot be used as a true material property. Furthermore, when designing and analyzing large structures such as dams, bridges, and nuclear reactors that behave in a brittle manner, a fracture mechanics approach is very beneficial [12].

The studies on determining the fracture properties of concrete were first conducted by Kaplan in 1961 [13]. His study was based on the linear elastic fracture mechanics (LEFM), which proposes a single parameter; the critical stress intensity factor K_{IC}. However, several experimental investigations conducted in the 1970s showed that LEFM for quasi-brittle materials such as concrete is no longer valid [14]. This is due to the presence of a relatively large inelastic zone in front of and around the tip of the main cracks in concrete which are ignored by LEFM [15]. Since then, various non-linear fracture mechanics models have been proposed to determine the fracture toughness of concrete

materials including the fictious crack model [16], the crack band model [17], the two-parameter model [18, 19], the size-effect model [20], the effect crack model [21-24], and the double-K fracture model [25-27]. The goal of each model is to determine the critical crack extension, which depends on the structural size because of its tendency to converge with the initial crack length as the size increases [20]. For this reason, at least two fracture parameters are required for concrete fracture. Different beam sizes, water to cement ratio, and notch to depth ratio have been employed to measure the fracture toughness of cement paste using several fracture models. Most of the research on this subject is summarized and compared with the results of this study in Table 4.1.

In this study, fracture mechanics approaches, including the two-parameter fracture model by Jenq and Shah [19] and finite element method in conjunction with experimental observations, were utilized to identify the correlation between damage mechnisims and AE activity defined in previous work [1]. The stress intensity factor (SIF) was calculated and compared to its critical value or fracture toughness (FT), to define the stage at which a crack grows in an unstable manner.

4.3 Objective

In previous work [1], an investigation of micro-crack formation and coalescence in cement paste specimens under compression was performed to identify three distinct stages of crack behavior based on AE data parameters analysis and experimental observations. The objective of this study is to identify the correlation between previously defined damage mechnisims and AE activity. This goal was approached through using experimental and theoretical investigation on cement paste specimens based on the fracture mechanics

approach. The two-parameter fracture model by Jenq and Shah [19] and finite element method in conjunction with experimental observations were utilized.

Table 4.1 Comparison of the critical stress intensity factor (Fracture toughness, K_{IC}) of cement paste

TPB beam size, mm (in)	Water/Cement weight ratio (other additives)	Notch to depth ratio, a_o/d	K_{IC}, MPa.m$^{0.5}$ (psi.in$^{0.5}$)	Fracture model	Reference
375×75×50 (15×3×2)	0.3	Not reported	0.76 (691)	ASTM E399-374, 1974	Strange and Bryant, 1979 [28]
188×38×25 (7.5×1.5×1)			0.6 (546)		
125×25×25 (5×1×1)			0.6 (546)		
60×12×12 (2.4×0.48×0.48)			0.55 (500)		
900×225×84 (36×9×3.375)	0.45 (fine agg./cement ratio = 0.5)	1/3	0.65 (595)	Two-parameter	Jenq, and Shah, 1985 [19]
600×150×56 (24×6×2.25)			0.59 (544)		
300×75×28 (12×3×1.125)			0.6 (547)		
160×40×40 (6.4×1.6×1.6)	0.55	0.4	0.27 (245)	Double-K	Xu, and Zhu, 2009 [29]
	0.45		0.36 (327)		
	0.4		0.43 (391)		
280×70×70 (11.2×2.8×2.8)	0.45		0.31 (282)		
400×100×100 (16×4×4)	0.55		0.35 (318)		
	0.45		0.37 (336)		
	0.4		0.51 (464)		
160×40×40 (6.4×1.6×1.6)	0.2 (2% superplasticizer, and 1% defoamer/c)	0.5	0.51 (464)	RILEM	Hu, et al., 2014 [30]
152×38×38 (6×1.5×1.5)	0.5	1/3	0.54 (494)	Two-parameter by Jenq and Shah [19]	Current study

4.4 Experimental Work

4.4.1 Materials and specimen

Cement paste specimens were made using Portland cement Type I/II with water to cement weight ratio of 0.5 and prepared according to ASTM C305 [31]. The mixtures were then cast in 38.1mm × 38.1mm × 152.4 mm (1.5 inch × 1.5 inch × 6 inches) acrylic

molds and vibrated for ten seconds. After 24 hours, the specimens were taken from the molds and put in lime water for 28 days.

4.4.2 Experimental test setup

Three-point bending beam specimens with a loading span-to-depth ratio (S/D) of three were used to measure the fracture properties of hardening cement paste (Figure 4.1). A 12.7 mm (0.5 in) notch length with width (N) of 1.3 mm was introduced into the specimens using a water-cooled saw machine. The length of the notch was calculated based on the RILEM standard [32], which requires a notch to depth ratio of close to 30 percent. The tests were performed on a closed-loop servo-hydraulic testing machine under displacement control with a rate of 0.018 mm/min. A pair of knife edges was glued to the two sides of a notch performed on the lower surface of the beam. A clip gauge from Epsilon was used to record the crack mouth opening displacement (CMOD) during the test. The test setup with supports details are shown in Figure 4.1.

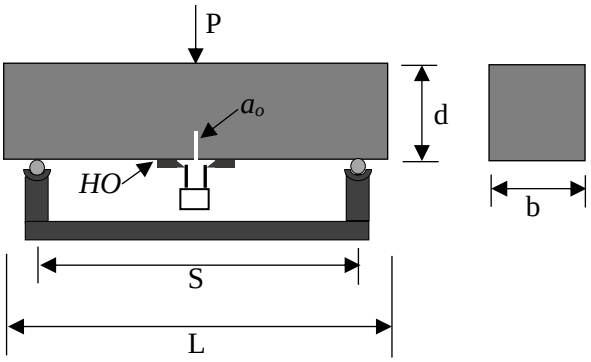

Parameter	Value, mm (in)
S	114.3 (4.5)
L	152.4 (6)
d	38.1 (1.5)
a_o	12.7 (0.5)
b	38.1 (1.5)
HO	1.5 (0.06)

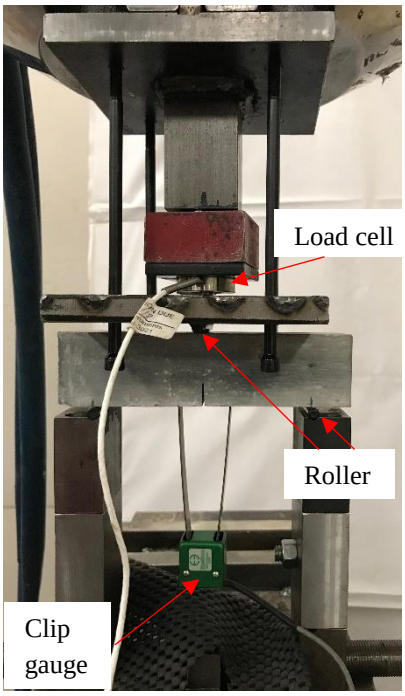

Figure 4.1 Experimental setup

4.5 Experimental Determination of Fracture Parameters

The two-parameter fracture model proposed by Jenq and Shah [19] was used to determine the mode I fracture toughness, K_{Ic}, (critical value of stress intensity factor) of cement paste specimens from the experimental results. First, the specimens were monotonically loaded up to maximum load. The applied load is then automatically reduced using failure detector command when the load as within 95% of maximum load and after the load passed the maximum load. Second, four quantities are measured from the recorded load versus the CMOD curve for a loading-unloading cycle (see Figure 4.2) including:

a) The compliances for the loading (C_i) and unloading parts (C_u),

b) The peak load, P_{max}, and

c) Total CMOD at P_{max}.

Young's modulus is then calculated from the initial slope of load-CMOD curve using equation 4.1. An iterative numerical approach is performed to determine K_{Ic} where an effective crack length, a_c (*a_c = initial crack length, a_o + stable crack growth at peak load*) is first assumed and verified only when the measured value of CMOD agrees with the calculated value according to equation 4.3 [19]. Once an effective crack length is obtained the K_{IC} is then calculated using equation 4.5.

$$E = \frac{6Sa_oV_1(\alpha_o)}{C_i d^2 b} \quad \ldots\ldots\ldots\ldots\ldots\ldots\ldots \quad (4.1)$$

Where, C_i is the initial compliance calculated from the load-CMOD curve (Figure 4.2), $\alpha_o = (a_o + HO)/(d + HO)$, a_o = crack length, S = span length, d = specimen depth, b = specimen thickness, HO = thickness of knife edges defined in Figure 4.1, $V_1(\alpha)$ = geometric function defined by:

$$V_1(\alpha_o) = 0.76 - 2.28\alpha_o + 3.87\alpha_o^2 - 2.04\alpha_o^3 + \frac{0.66}{(1-\alpha_o)^2} \quad \ldots\ldots\ldots\ldots \quad (4.2)$$

$$CMOD = \frac{6P_{max}\, S\, a_c V_1\left(\frac{a_c}{d}\right)}{d^2 bE} \ldots\ldots\ldots\ldots\ldots\ldots\ldots\ldots\ldots\ldots\ldots\ldots\ldots (4.3)$$

where, $V_1\left(\frac{\alpha_c}{d}\right) = 0.76 - 2.28\left(\frac{\alpha_c}{d}\right) + 3.87\left(\frac{\alpha_c}{d}\right)^2 - 2.04\left(\frac{\alpha_c}{d}\right)^3 + \frac{0.66}{\left(1-\frac{a_c}{d}\right)^2} \ldots\ldots\ldots\ldots (4.4)$

$$K_{IC} = 3(P_{max} + 0.5W)\frac{S\sqrt{\pi a_c}F(a_c/d)}{2d^2 b} \ldots\ldots\ldots\ldots\ldots\ldots\ldots\ldots\ldots\ldots\ldots (4.5)$$

where, *P*P_{max} = the peak load, $W = W_o S/L$, W_o = self-weight of the beam, and

$$F\left(\frac{a_c}{d}\right) = \frac{1.99-(a_c/d)(1-a_c/d)\left[2.15-3.93(a_c/d)+2.7(a_c/d)^2\right]}{\sqrt{\pi}(1+2a_c/d)(1-a_c/d)^{3/2}} \ldots\ldots\ldots\ldots\ldots\ldots\ldots (4.6)$$

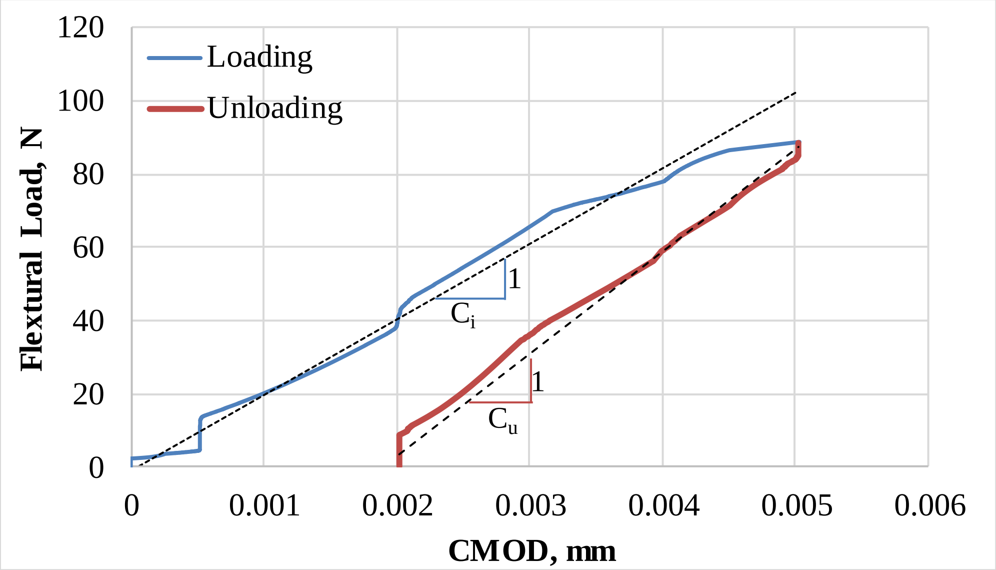

Figure 4.2 Load versus CMOD response of cement paste specimen under loading-unloading cycle

4.6 Results and Discussion

4.6.1 Classification of crack growth based on AE parameters [1]

The AE data recorded during loading up to failure (10.2 kN (2.3 kip) of the cement paste prism was analyzed for identification of the stages of the fracture process using AE parameters such as amplitude and signal strength. Microcracks initiated and propagated to

form visible cracks at the times referenced by the arrows shown in Figure 4.3a. In addition to the several bursts of AE activities highlighted by arrows, AE activity increased over time during testing, indicating that more micro-crack growth and coalescence occurred throughout the loading. The number of AE hits and associated CSS show clearly defined regions as seen in Figure 4.3. Three ranges of crack behavior, illuminated by changes in the slope of the cumulative signal strength curve, can be observed. Significant jumps in CSS compared with the previous stages were observed and used to distinguish between the divided regions (Figure 4.3b). The jump in AE event rate is attributed to the localization of micro-cracking and macro-cracking into a single critical crack [33, 34].

The first region (R1), represented by the early stage (elastic deformation stage), showed very little AE activity which can be assigned to micro-crack initiation (no visible crack was seen at this stage). As the load increased, the second region (R2), represented by the stable stage, showed increases in the AE activity due to formation of stable visible cracks. The maximum cracks lengths of approximately 0.85-1 inch were seen at the beginning of this stage and other one of 2 inches was observed within this region (Figures 4.4a to 4.4e). Therefore, this region can be assigned to the formation and extension of cracks and micro-cracks. The third region (R3), represented by the unstable stage, showed abrupt increases in AE activity (Figure 4.3). The maximum cracks lengths of approximately 2.5 and 3 inches were observed at the beginning and within this stage (Figures 4.4f and 4.4g) and propagated to the whole specimen length at the end of this region (Figures 4.4h). This region can be assigned to unstable crack extension and coalescence, leading to eventual failure.

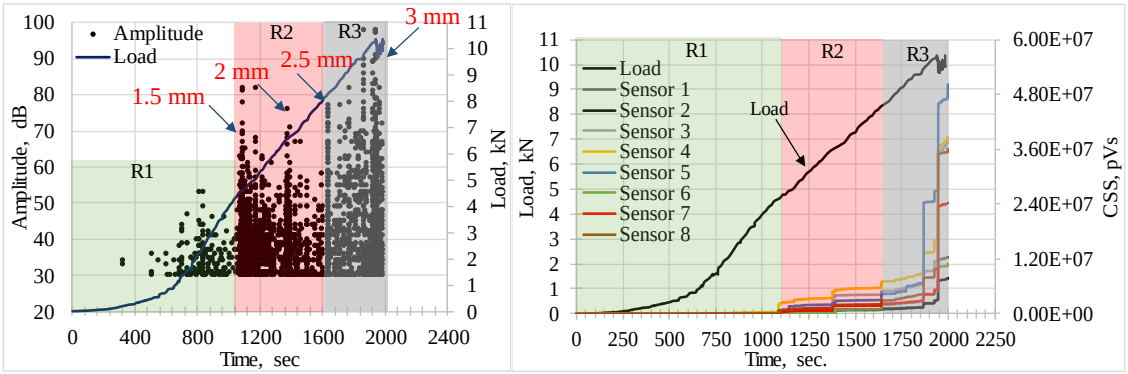

(a) amplitude and load versus time (b) CSS and load versus time

Figure 4.3: AE data activity versus load of specimen loaded to failure

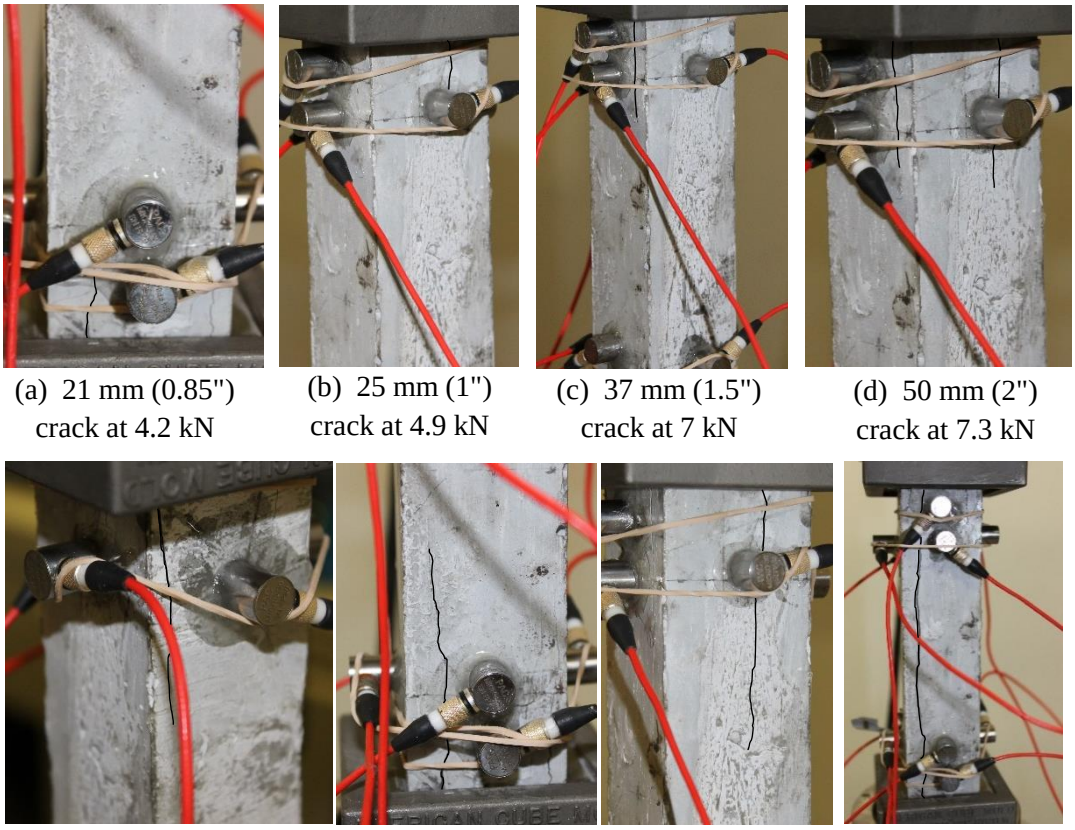

(a) 21 mm (0.85") crack at 4.2 kN

(b) 25 mm (1") crack at 4.9 kN

(c) 37 mm (1.5") crack at 7 kN

(d) 50 mm (2") crack at 7.3 kN

(e) 50 mm (2") crack at 7.4 kN

(f) 63 mm (2.5") crack at 8.6 kN

(g) 76 mm (3") crack at 9.3 kN

(h) 150 mm (6") crack at 10.2 kN

Figure 4.4 Crack initiation and propagation under varying compressive loads
(Note: crack lengths are approximated values, 1 MPa = 145 psi)

4.6.2 Three-point bending test results and fracture toughness calculation

The load versus CMOD graphs were created from the test results consisting of a linear elastic stage before crack initiation, a nonlinear stage of stable crack growth, and an unstable crack extension after the peak load. An example of load-CMOD curve recorded under monotonically increasing displacement control of cement paste specimen is shown in Figure 4.5.

For fracture toughness calculation, an average value of three specimens under loading-unloading cycle as explained in Figure 4.2 was used to calculate the fracture toughness reported in Table 4.2. Furthermore, the results were compared with the previous works (Table 1) to show the fracture toughness ranges of cement paste calculated based on different proposed models. Strange and Bryant [28] used cement paste with a w/c of 0.3 and different specimen sizes. Based on the ASTM E339-374, 1974 procedure [35], the calculated K_{IC} values ranged from 0.76 MPa.m$^{0.5}$ (691 psi.in$^{0.5}$) for large size specimens to 0.55 MPa.m$^{0.5}$ (500 psi.in$^{0.5}$) for small size specimens. The experimental results presented by Jenq and Shah [19] of notched beams with varying dimensions showed that the proposed two parameter fracture model is to be independent of beam size. The K_{IC} values varied from 0.65 MPa.m$^{0.5}$ (595 psi.in$^{0.5}$) for large size specimens to 0.6 MPa.m$^{0.5}$ (547 psi.in$^{0.5}$) for small size specimens using cement paste with a w/c of 0.45 and a s/c of 0.5. The double-K fracture parameter model was used by Xu and Zhu [29] to calculate the fracture toughness of cement paste having different w/c ratios and beam sizes. For the same w/c (i.e. w/c of 0.4) the values of K_{IC} were ranged from 0.51 MPa.m$^{0.5}$ (464 psi.in$^{0.5}$) for large size specimens to 0.43 MPa.m$^{0.5}$ (391 psi.in$^{0.5}$) for small size specimens. The Rilem procedure [32] was used by Hu et al. [30] to calculate the fracture toughness of cement paste with a w/c of 0.5 and superplasticizer of 1% of cement weight. The average value of

K_{IC} for three specimens with a w/c of 0.5 was 0.51 MPa.m$^{0.5}$ (464 psi.in$^{0.5}$). In this study, the average value of K_{IC} for three specimens was 0.54 MPa.m$^{0.5}$ (494 psi.in$^{0.5}$), which is comparable with previous works.

The fracture toughness shown in Table 4.2 is compared with the stress intensity factor calculated from the finite element method in the next section to identify the defined damage mechanisms reported in the previous study [1] based on AE data.

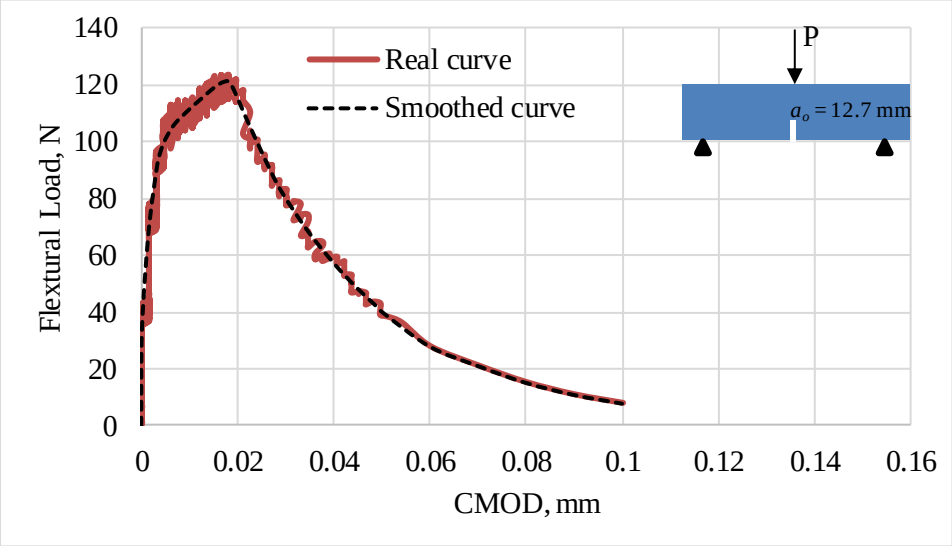

Figure 4.5 Load versus CMOD relationship

Table 4.2 Three-point bending testing results

Specimen number	**Critical crack length, a_c, mm (in)**	**Modulus of Elasticity, E, GPa (ksi), equation 4.1**	**Fracture toughness, MPa.m$^{0.5}$ (psi.in$^{0.5}$)**
S1	30.7 (1.2)	7.4 (1073.2)	0.53 (486)
S2	26.7 (1.0)	7.4 (1073.2)	0.57 (519)
S3	28.7 (1.1)	7.2 (1044.2)	0.54 (494)
Average	28.7 (1.1)	7.3 (1063.5)	0.54 (494)
SD	2	16.7	0.02
COV	0.06	0.01	0.03

4.7 Finite Element Model Setup

4.7.1 Geometry and material properties

The compression test of cement paste prisms was simulated using the Abaqus finite element program to determine the stress intensity factor along a predefined crack tip. First, a three-dimensional model of the prism was created as a whole "3D deformable extrusion solid" with dimensions of 38.1mm × 38.1mm × 152.4 mm (1.5 inch × 1.5 inch × 6 inches). Second, a linear elastic solid material was assumed, and the material properties were added, including modulus of elasticity, E = 1,059,000 psi (measured using TPB test as explained in the previous section) and Poisson's ratio, $\nu = 0.2$.

4.7.2 Boundary conditions and loading

Loading and boundary conditions were applied as they were tested experimentally. The bottom surface was modeled as a pinned support with restrictions in movement in every direction, X, Y and Z (global axes of the model), to eliminate rigid body motion while simulating the far-field boundary. While the top surface was restrained in X and Z directions. Loading was applied as a displacement boundary condition since the experimental testing was conducted based on displacement control testing at a rate of 0.1 mm/min. Four different levels of uniform downward displacement were applied on the top surface based on the divided regions defined previously in Anay et al. [1] which are referenced by arrows shown in Figure (4.3a) including:

- Displacement of 1.5 mm (0.06") at the beginning of the R2 region.
- Displacement of 2 mm (0.08") within the R2 region.
- Displacement of 2.5 mm (0.1") at the beginning of the R3 region.
- Displacement of 3 mm (0.12") at the end of the R3 region (end of the test at failure).

The loading, prism orientation, and support conditions are illustrated in Figure 4.6.

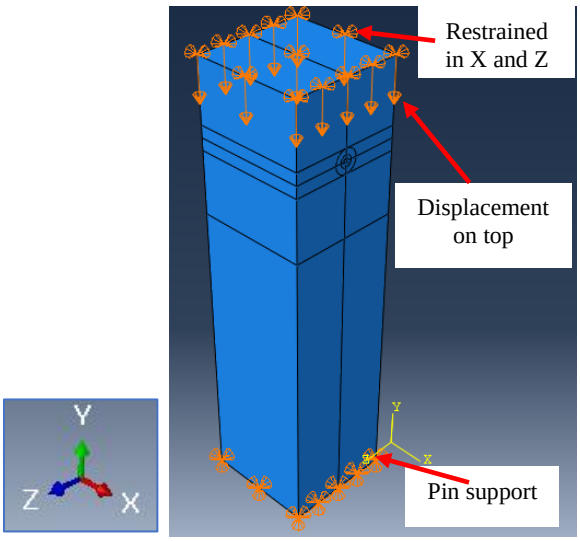

Figure 4.6 Model geometry and boundary condition

4.7.3 Mesh design

The mesh includes a seam (a face in a model that is originally closed but can open during an analysis) along the crack with duplicate nodes, which allows the crack to open when loaded. A singularity was included in the mesh by moving the midside nodes towards the crack tip (midside node parameter of 0.25 was used). The nodes at the same location at the crack tip were constrained to move together as a single node (collapsed element side, single node). A polar FEM mesh with a strong concentric refinement around the crack tip is effective for stationary cracks [36, 37]. Therefore, around the crack tip, the geometry was partitioned to map rings of elements for the contour integral calculations. Figure 4.7 shows the mesh pattern of the prism constructed in the FE models together with the closer view of elements near the crack front. At the crack tip, an element should have a size L that should be considerably below the validity range, r_K, of the K_I-dominated near field since r_K of the crack singularity is narrowly limited. In addition, enough elements should also be

distributed over the circumference to properly reproduce the angular distribution [36]. The range of r_K is $a/10$ to $a/50$, thus the following relations should be observed:

• element size at the crack tip: $L < a/20$ to $a/100$, where a is the crack length.

• number of elements/semicircle: $n > 6$ or $\theta < 30^{\circ}$.

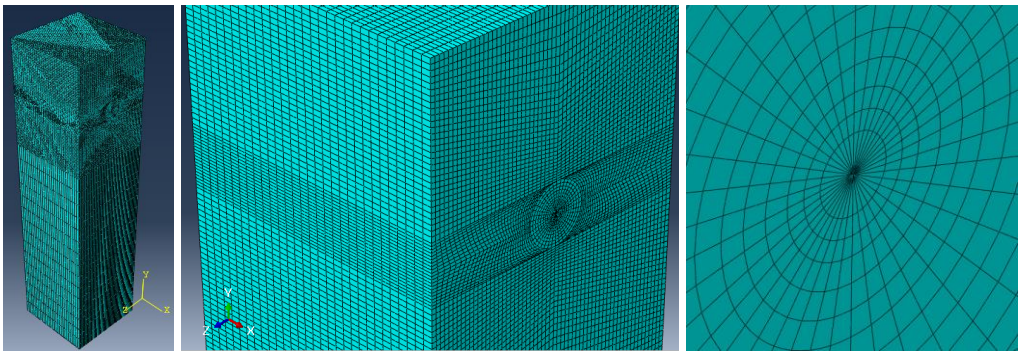

Figure 4.7 FEM with enlarged detail

Three domains can be distinguished based on the results of validity range r_K (Figure 4.8) [36]. At FEM erroneous domain (the elements very close to the crack tip), K_I falls too short in comparison to the exact value of K_I, and the singularity can only be characterized inaccurately, therefore the K_I values are neglected for the first one or two counters. At the mid-range (the elements inside crack singularity region), the quality of the FEM solution is enough, while outside the singularity region, ($r > r_K$) more solution is required in addition to the singularity.

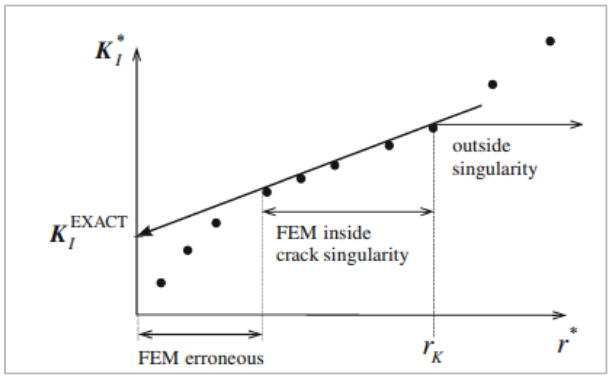

Figure 4.8 Validity range of FEM interpretation (at different r and constant θ) [36]

A refined mesh at the crack tip was used to obtain accurate results when analyzing the stress field around a crack tip, and to capture the strong gradients near the tip [37]. Then, the mesh was biased moderately toward the crack tip in the circular partitioned region surrounding the crack tip where the contour integrals are calculated (Figure 4.7). The diameter of the inner circular partition used to map the crack-tip mesh was 0.5 mm (0.02"), (Figure 4.9). Furthermore, mesh size analysis was performed to choose the best element size that provides reliable results within a convenient time in terms of stress intensity factors. Figure 4.10 shows that more than 20 elements along the crack front is enough to provide consistent SIFs. Therefore, 30 elements along the crack front was used such that the element size at the crack tip was 1.27 mm (0.05 in.) which is *a*/20, and the number of elements/semicircle was 20 ($\theta = 9^o < 30^o$).

When three-dimensional contour integrals are calculated, rings of brick elements must be used around the crack tip with wedge elements adjacent to the crack tip [37]. Therefore, specimen geometries were meshed by using a 20-node quadratic brick element, C3D20R (hexahedral elements) except for around the crack tip (inner tabular partition). Around the crack tip a 15-node quadratic triangular prism, C3D15 (Wedge element), was utilized to introduce a singularity at the crack tip.

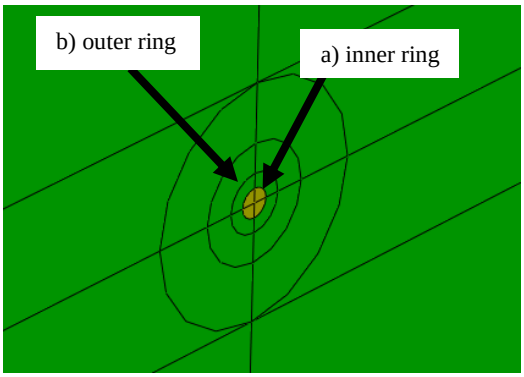

a) the smaller inner ring is swept meshed using wedge elements

b) the outer ring is meshed using hexahedral elements and the structured meshing technique

Figure 4.9: Partitions around the crack line

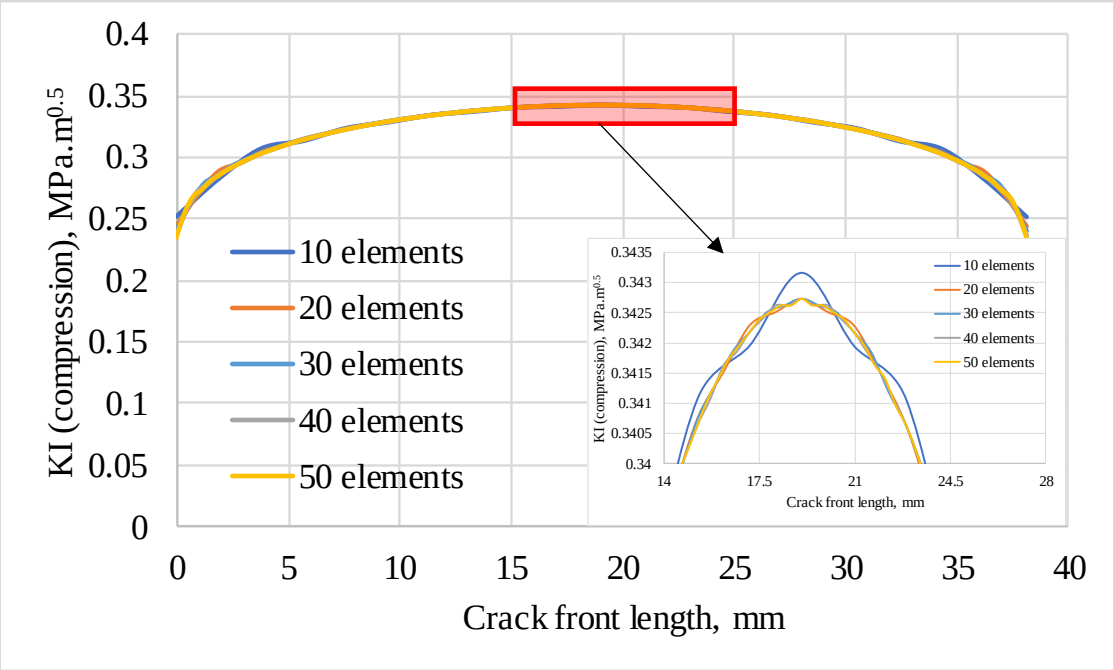

Figure 4.10 Mesh size analysis

4.7.4 Crack modeling

Stationary crack subjected to compression loads was defined since calculating the stress intensity factor is not required to model crack propagation. The crack is modeled as a seam since the crack surfaces in the unloaded state lie next to one another with no gap (Figure 4.11). The crack properties (length, direction and position) were defined based on the experimental observations. Several cracks with different lengths and locations were developed during the test (Figure 4.4), however only the first visible crack initiated at the beginning of the R2 region was selected for theoretical calculation (Figure 4.4b). The crack length was 25.4 mm (1") and 38.1mm (1.5") width.

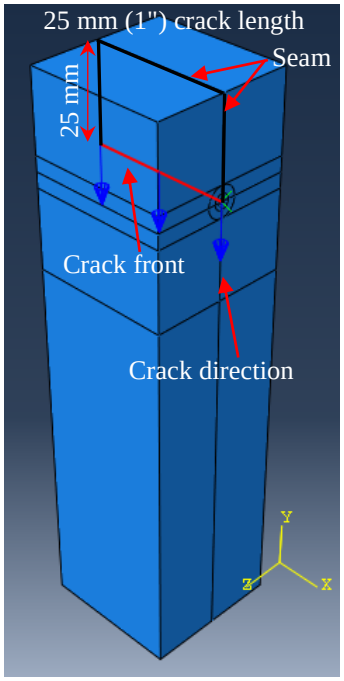

Figure 4.11 Partitioning the geometry
based on crack location and length

4.7.5 Finite element modeling results

The maximum stress intensity factors of mode I (KI) extracted from the ABAQUS at different levels of displacement are shown in Table 4.3. Figure 4.12 plots distribution of the stress intensity factors through the crack front of the specimen. At the time of the first visible crack initiation (beginning of the R2 region) and propagation (within the R2 region), the KI was less than the fracture toughness of cement paste. This indicates that within this region, cracks were initiated and propagated in a stable manner which approves the assigned damage mechanism to the R2 region based on AE data. While within R3 region to the end of the test, the stress intensity factor passed the fracture toughness. This specifies that R3 region represents unstable crack growth which supports the assigned damage mechanism to the R3 region based on AE data.

Table 4.3 Finite element results

	Beginning of R2 region	Within R2 region	Beginning of R3 region	End of R3 region
Time, sec	1080	1380	1638	2000
Load, kN (lb)	4.2 (959)	6.1 (1388)	8.2 (1851)	10.2 (2300)
Stress, MPa (psi)	2.9 (426)	4.2 (616)	5.6 (822)	7 (1022)
Displacement, mm (in)	1.5 (0.06)	2 (0.08)	2.5 (0.1)	3 (0.12)
Maximum Stress intensity factor, KI, MPa. $m^{0.5}$ (psi.$in^{0.5}$)	0.38 (352)	0.51 (470)	0.64 (587)	0.77 (705)
Fracture toughness, K_{IC}, MPa. $m^{0.5}$ (psi.$in^{0.5}$)	**0.54 (494)**			

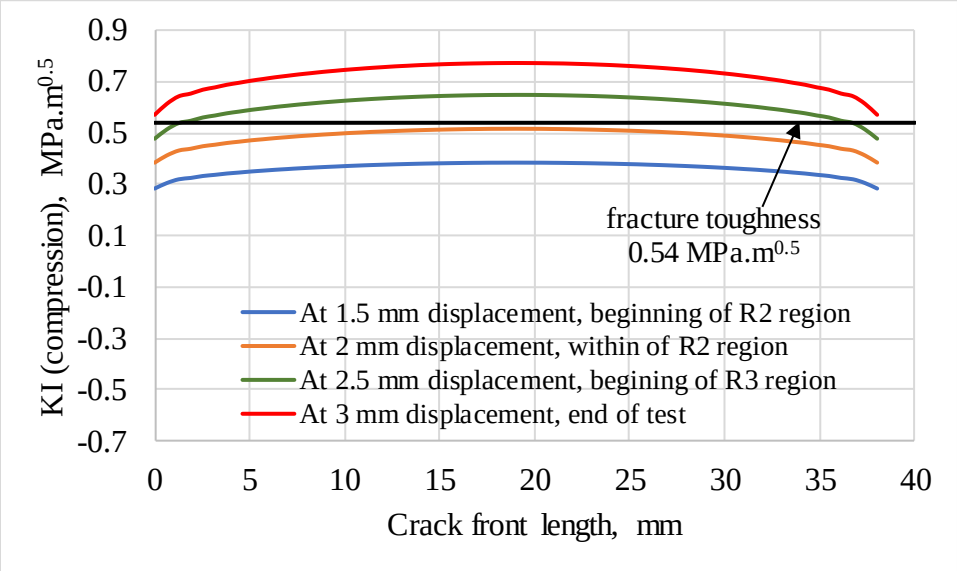

Figure 4.12 Stress intensity factors of mode I (KI) at the crack front of the specimen (1 MPa.$m^{0.5}$ = 910 psi.$in^{0.5}$)

4.8 Conclusion

In this study, fracture mechanics approaches, including the two-parameter fracture model by Jenq and Shah [19] and the finite element method in conjunction with experimental observations, were utilized to identify the correlation between damage mechnisims and AE activity defined in the previous work [1]. Stress intensity factor (SIF)

was calculated and compared to its critical value, fracture toughness (FT) to define the stage of unstable crack growth. Conclusions are as follows:

- The fracture mechanics approach and the finite element method in conjunction with experimental observations are effective tools to better describe the behavior of cementitious materials under compression.
- Microcrack initiation and extension defined by AE parameters analysis was verified since the stress intensity factor of mode I was less than the fracture toughness of cement paste (stable crack growth).
- Unstable crack propagation defined based on AE data was also verified since the stress intensity factor of mode I passed the fracture toughness value.
- This work shows that AE and the fracture mechanics approach are complementary methods to characterise damage sites in cement-based materials.

Finally, since the proposed strategy was applied on specimens loaded in compression, future research could include testing in tension while monitoring with AE.

4.9 References

[1] Anay, R., Soltangharaei, V., Assi, L., DeVol, T., & Ziehl, P. Identification of damage mechanisms in cement paste based on acoustic emission. Construction and Building Materials, 164, (2018) 286-296.

[2] ASTM, ASTM E1316-10b: Standard Terminology for nondestructive examinations, (2013).

[3] Abdelrahman, M. Assessment of damage in concrete structures using acoustic emission. Thesis, University of South Carolina, (2013) pp. 132.

[4] Ono, K. Application of Acoustic Emission for Structure Diagnosis. Konferencja Naukowa, (2010) pp. 317-341.

[5] Abdelrahman, M., ElBatanouny, M. K., Ziehl, P., Fasl, J., Larosche, C. J., & Fraczek, J. Classification of alkali–silica reaction damage using acoustic

emission: A proof-of-concept study. Construction and Building Materials, 95 (2015) 406-413.

[6] Soltangharaei, V., Anay, R., Hayes, N., Assi, L., Le Pape, Y., Ma, Z., & Ziehl, P. Damage Mechanism Evaluation of Large-Scale Concrete Structures Affected by Alkali-Silica Reaction Using Acoustic Emission. Applied Sciences, 8 (2018) 2148.

[7] Wu, K., Chen, B., & Yao, W. Study on the AE characteristics of fracture process of mortar, concrete and steel-fiber-reinforced concrete beams. Cement and Concrete Research, 30 (2000) 1495-1500.

[8] Sagar, R. V., Prasad, R. V., Prasad, B. R., & Rao, M. V. M. S. Microcracking and fracture process in cement mortar and concrete: a comparative study using acoustic emission technique. Experimental Mechanics, 53 (2013) 1161-1175.

[9] Puri, S., & Weiss, J. Assessment of localized damage in concrete under compression using acoustic emission. Journal of materials in civil engineering, 18 (2006) 325-333.

[10] Elaqra, H., Godin, N., Peix, G., R'Mili, M., & Fantozzi, G. Damage evolution analysis in mortar, during compressive loading using acoustic emission and X-ray tomography: effects of the sand/cement ratio. Cement and Concrete Research, 37 (2007) 703-713.

[11] Haneef, T. K., Kumari, K., Mukhopadhyay, C. K., Rao, B. P., & Jayakumar, T. Influence of fly ash and curing on cracking behavior of concrete by acoustic emission technique. Construction and Building Materials, 44 (2013) 342-350.

[12] Gdoutos, E. E., Konsta-Gdoutos, M. S., & Danoglidis, P. A., Portland cement mortar nanocomposites at low carbon nanotube and carbon nanofiber content: A fracture mechanics experimental study, Cement and Concrete Composites, 70 (2016) 110-118.

[13] Kaplan MF. Crack propagation and the fracture of concrete. J Am Concr Inst., 58 (1961) 591-610.

[14] Kesler CE, Naus DJ. Lott LL. Fracture mechanics – its applicability to concrete. In: Proceedings of the international conference on the mechanical behavior of materials, Kyoto, 1971, The Society of Material Science; 4 (1972) 113-24.

[15] Ince, R. Determination of concrete fracture parameters based on two-parameter and size effect models using split-tension cubes. Engineering Fracture Mechanics, 77 (2010) 2233-2250.

[16] Hillerborg A, Modeer M, Petersson PE. Analysis of crack formation and crack growth in concrete by means of fracture mechanics and finite elements. Cement Concr Res 6: (1976) 773-782.

[17] Bazant ZP, Oh BH. Crack band theory for fracture of concrete. RILEM Mater Struct 16(93): (1983) 155-177.

[18] Jenq Y.S., Shah S.P. A fracture toughness criterion for concrete. Eng Fract Mech 21(5): (1985a) 1055-1069.

[19] Jenq Y.S., Shah S.P. Two parameter fracture model for concrete. J Eng Mech 111(10): (1985b) 1227-1241.

[20] Bazant Z.P., Kazemi M.T. Determination of fracture energy, process zone length, and brittleness number from size effect with application to rock and concrete. Int J Fract. 44 (1990) 111–31.

[21] Swartz SE, Go CG. Validity of compliance calibration to cracked concrete beams in bending. Exp Mech. 24 (1984) 129-134.

[22] Swartz SE, Refai TME. Influence of size on opening mode fracture parameters for precracked concrete beams in bending. In: Shah SP, Swartz SE (eds) Proceedings of SEMRILEM international conference on fracture of concrete and rock. Houston, Texas, (1987) 242-254.

[23] Karihaloo BL, Nallathambi P. An improved effective crack model for the determination of fracture toughness of concrete, Cement Concr Res 19: (1989) 603–610.

[24] Karihaloo BL, Nallathambi P. Effective crack model for the determination of fracture toughness (KIc s) of concrete. Eng Fract Mech. 35 (1990) 637-645.

[25] Xu SL, Reinhardt HW. Determination of double−K fracture parameters in standard three-point bending notched beams, In: Mihashi H, Rokugo K (eds) Fracture mechanics of concrete structures, Proc. of FRAMCOS-3. Aedificatio, Freiburg, Germany, 1 (1998) 431-440.

[26] Xu SL, Reinhardt HW. Determination of double−K criterion for crack propagation in quasi-brittle materials, part II: analytical evaluating and practical measuring methods for three-point bending notched beams. Int J Fract. 98 (1999) 151-177.

[27] Xu SL, Reinhardt HW. A simplified method for determining double–K fracture parameters for three-point bending tests. Int J Fract 104 (2000) 181-209.

[28] Strange, P. C., & Bryant, A. H. Experimental tests on concrete fracture. Journal of the Engineering Mechanics Division, 105 (1979) 337-342.

[29] Xu, S., & Zhu, Y. Experimental determination of fracture parameters for crack propagation in hardening cement paste and mortar. International Journal of Fracture, 157 (2009) 33-43.

[30] Hu, Yu, Danni Luo, Penghui Li, Qingbin Li, and Guoqiang Sun. Fracture toughness enhancement of cement paste with multi-walled carbon nanotubes. Construction and Building Materials 70 (2014) 332-338.

[31] ASTM International, ASTM C305: Standard Practice for Mechanical Mixing of Hydraulic Cement Pastes and Mortars, Am. Soc. Test. Mater. (2011) 13-15.

[32] TC89-FMT, R. I. L. E. M. Fracture mechanics of concrete test methods. Mater Struct, 23 (1991) 457-460.

[33] Landis, E.N., Shah, S.P. The influence of microcracking on the mechanical behavior of cement based materials, Adv. Cem. Based Mater. 2 (1995) 105-118.

[34] Li, Z., Shah, S.P. Localization of Moikrocracking in Concrete under Uniaxial Tension, ACI Mater. J. 91 (1994) 372–381.

[35] ASTM E339-374. Standard method of test for plane-strain fracture toughness of metallic materials. ANSI/ASTM E399-374. American Society for Testing and Materials, Philadelphia, 1974

[36] Kuna, M., Finite elements in fracture mechanics. Berlin: Springer. (2013), pp. 447.

[37] Manual, Abaqus Users. Version 6.13-2. Dassault Systémes Simulia Corp., Providence, Rhode Island, USA (2013).

Chapter 5

On-Site Acoustic Emission Monitoring for a Prestressed Concrete BT-54 AASHTO Girder Bridge[3]

[3]Anay, R., Lane, A., Jáuregui, D., Weldon, B., Soltangharaei, V., and Ziehl, P. (2018). On-Site Acoustic-Emission Monitoring for Assessment of a Prestressed Concrete BT-54 AASHTO Girder Bridge. Submitted to *ASCE-Journal of Performance and Constructed Facilities, 01/3/2019*

5.1 Abstract

Acoustic emission (AE) data was investigated to better understand damage conditions in a three-span prestressed concrete girder bridge during a load test. The innovation lies in classification of crack extensions (stable or unstable) during the loading and holding processes. The gap in current literature addressed is a paucity of data and findings on bridges in operation and having inclined cracks. This manuscript addresses the collection and processing of AE signals recorded by piezoelectric sensors attached on two interior girders toward the obtuse corner of an exterior span of the bridge while under loading. Results showed signs of crack propagation beyond the existing cracks. Damage classification procedures based on AE data recorded during one loading and holding step provided an indication of diminishing crack extensions as the load hold was continued in one girder. Concurrently, signs of unstable crack propagation were shown in the other girder. The use of previously developed AE analysis methods to evaluate the condition of each girder is discussed. Finally, shear strength analysis using modified compression field theory (MCFT) was performed to place the results in context.

Keywords: Load testing; Nondestructive evaluation; Acoustic emission; Prestressed concrete bridges; Inclined cracking; Shear; Modified compression field theory; Bridge inspection; Condition state

5.2 Introduction

Because the detection and tracking of potential damage and assessing the influence of that damage on the condition of a structure are a part of the service life evaluation, methods should be developed to detect the onset of deterioration and enable the monitoring

of its growth. Consequently, this study addresses the on-site monitoring of a three-span, prestressed concrete BT-54 AASHTO girder bridge exhibiting diagonal cracks in four girders of the exterior spans. In this structure most of the cracks now extend past epoxy injection and some girders have developed new cracks. The main objective was to classify the state of crack extensions (stable or unstable) during the loading and holding process. A new condition rating criterion was investigated for use by bridge owners as a warning for action. Challenges remain for development of any criterion for existing structures experiencing different levels of damage, and more field tests are required.

Although laboratory specimens that are representative of in-service bridges have been tested under flexural and shear loadings and monitored using AE [1-5] only a few tests have been conducted on structures such as bridges that are in operation and have inclined cracks. The lack of available field data creates challenges in testing prestressed concrete girder bridges expected to fail in shear, which may be more sudden than flexural failure.

Several factors including the type of structure, inspection data related to the structure's existing condition, cost, availability, ease of installation, accuracy, and resources for data interpretation affect the selection of the most appropriate response measurements. Although visual inspection is primarily used in the United States by bridge owners to evaluate the condition of bridges, this method is poorly suited for identification of hidden defects and damage or those located in areas that are not easily accessible [6]. Alternatively, nondestructive evaluation (NDE) techniques have been performed in many industries to evaluate the properties of a material, component, or system without impairing its future usefulness or causing damage [7]. For the evaluation of shear strength conducted

in a laboratory or on-site, several types of NDE sensors and techniques have been used including Digital Image Correlation (DIC) [8, 9]; Demec Points [10, 11]; Linear Variable Differential Transformers (LVDTs) oriented at 90° to each other [12]; and Acoustic Emission (AE) [5, 13-15].

The term Acoustic Emission (AE) as used in this study is defined by the American Society for Testing and Materials ASTM E1316 as "transient elastic waves generated by a rapid release of energy from localized sources within a material" [16]. AE sensors are essentially piezoelectric crystals attached to the surface, which detect surface waves and convert them into electrical signals that are amplified and processed by associated data acquisition systems. AE monitoring has the potential to detect and quantify internal damage progression at the microscale level, making it useful for the detection and quantification of damage growth in real time. Moreover, it provides the capability to effectively monitor the internal condition of a structure under increasing loads and can potentially assist in establishing safe load limits [15, 17] and has been used to detect corrosion damage in posttensioned specimens with similar accuracy to conventional methods such as half-cell potential measurements [18]. One common challenge associated with AE monitoring and assessment is the proper interpretation of damage (e.g., crack growth events) and distinction from other sources, such as reflections from boundaries, wind-born debris, people walking, and tire friction.

On-site load tests of reinforced and prestressed concrete bridges in different states of deterioration have been performed and documented under regular traffic, dump trucks, and overloads using AE monitoring techniques [15, 19, 20]. The results of these tests indicate AE to be a well- suited method for evaluation of older bridges. In addition, Świt

[21] reported the application of AE for identifying active destructive processes and tracking their development during the routine operation of various structures including a steel bridge, steel columns supporting a structure for a cable car, a gas pipeline, and the My Thuan cable-stayed bridge. The recorded AE signals from each field test were grouped into classes to which various mechanisms were assigned based on the structure type.

Several methods have been proposed based on the Modified Compression Field Theory (MCFT) [22] to predict the shear strength of reinforced and prestressed concrete beams. Three approaches are presented in the AASHTO LRFD Specifications [23] including: a) direct calculation, specified in Article 5.8.3.4.2, b) an evaluation using tabularized values found in Appendix B5); and c) simplified procedure in Article 5.8.3.4.3 which is compatible with the concepts of ACI code 318-14 [24]. The MCFT, applied in this study, is a general model to predict the shear capacity of reinforced and prestressed concrete elements subjected to in-plane shear and normal stresses. The main objective is to place the AE results into context.

This study investigates a damage characterization approach for in-service bridges based on a key difference between the AE signals recorded during loading and holding steps. Furthermore, previously developed AE analysis methods were investigated to better understand results including 2D source location of AE events, intensity analysis, and AE signal parameter analysis.

5.2.1 Bridge description

The bridge evaluated in this study (NMDOT Structure #9130) is a three-span, continuous-for-live-load, prestressed concrete girder bridge. The length of span one is 15.2 m (50 ft), span two is 21.3 m (70 ft), and span three is 15.2 m (50 ft) (span three was

selected for load testing). Each span consists of four prestressed AASHTO Type BT-54 girders. The bridge is located in Guadalupe County, New Mexico, 0.32 km (0.2 miles) west of junction US-285/US-60 and US-54 near Vaughn, New Mexico. It is owned and maintained by the New Mexico Department of Transportation (NMDOT), was designed according to the AASHTO-LRFD Bridge Design Specifications, 1st edition [25], and constructed in 2002. The overall bridge width is 13.1 m (43 ft) while the roadway width is 12.2 m (40 ft) with a 30-degree skew. The beams are spaced 3.2 m (10.75 ft) apart and 0.8 m (32 in.) tall concrete barriers are present on the roadway edges, each with a width of 0.45 m (1.5 ft) (see Figure 5.1).

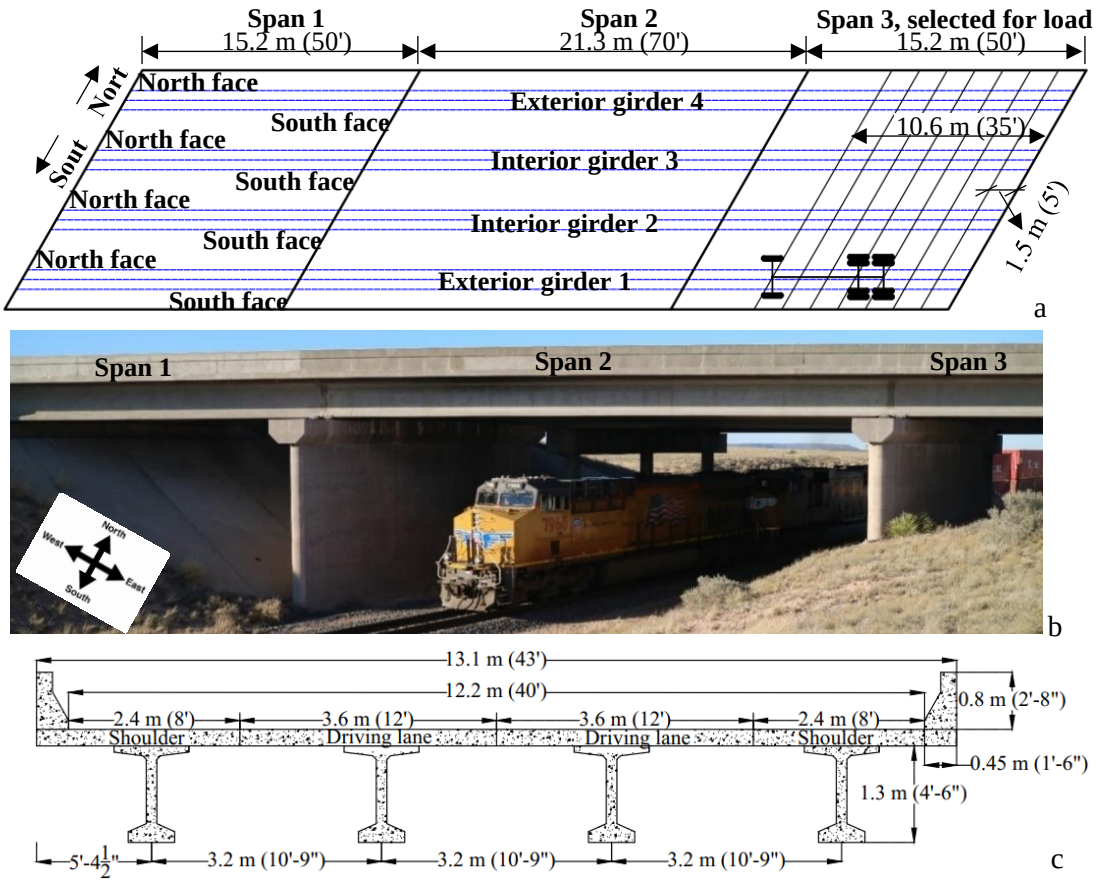

Figure 5.1 Bridge details, a: plan view; b: photograph of the bridge; c: cross section

5.2.2 Visual inspection

At the time of the load test (March 20, 2017), the most recent inspection had been performed on June 17, 2015 and the National Bridge Inventory (NBI) condition ratings were 6 for the deck (satisfactory condition), 5 for the superstructure (fair condition), and 7 for the substructure (good condition) (on the NBI rating scale, the best condition possible is a 9). The inspection report also contains the National Bridge Element (NBE) data for the 250 m or 820 linear feet (lf) of prestressed concrete girders; 146.3 m (480 lf) were assigned to condition state 1 (good condition), 91.5 m (300 lf) to condition state 2 (fair condition) due to patching, and 12.2 m (40 lf) to condition state 3 (poor condition) due to cracking (Table 5.1). The inspectors recommended continued monitoring of the cracking and epoxy injections, as well as a reduction of the inspection interval from two years to one year due to the cracks. Span three was selected for the load test since the girders showed more extensive cracking than span one and some cracks progressed further over the girder depth. Figure 5.2 shows the crack maps of interior girders in exterior span 3 and the maximum measured crack widths after load testing. In general, the interior girders showed more cracking than the exterior girders, particularly the interior girders closer to the obtuse corner (i.e., girder 2 of span three), which is expected since the load distribution is larger for these girders. This manuscript focuses on the AE data collected from the sensors attached on interior girders 2 and 3.

According to the AASHTO Manual for Bridge Element Inspection [26], National Bridge Element #109 (NBE 109) is defined as a pretensioned or post-tensioned concrete open web girder. Four condition states are defined for each type of defect including spalls/ delaminated/patched areas, exposed rebar and prestressing, cracking, and

efflorescence/rust staining. The condition state definitions for the crack defect (including the generalized distress and element commentary of the 2015 interim revisions) are shown in Table 5.1.

Table 5.1 Cracking defect-condition state definitions [26]

	Condition state 1 (Good)	**Condition state 2 (Fair)**	**Condition state 3 (Poor)**	**Condition state 4 (Severe)**
Definition	Insignificant cracks or moderate-width cracks that have been sealed (generalized distress) Width < 0.1 mm (0.004 in.)	Unsealed moderate-width cracks or unsealed moderate pattern (map) cracking (generalized distress) Width 0.1-0.23 mm (0.004-0.009 in.)	Wide cracks or heavy pattern (map) cracking (generalized distress) Width > 0.23 mm (0.009 in.)	The condition warrants a structural review to determine the strength or serviceability of the element or bridge; OR a structural review has been completed and the defects impact strength or serviceability of the element or bridge

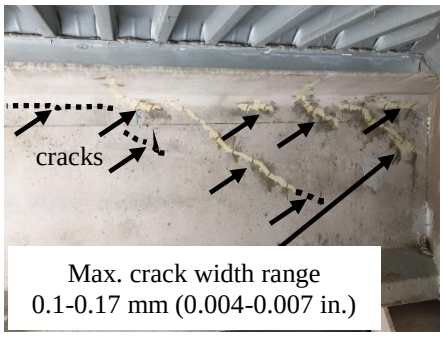

a) interior girder 2, South face

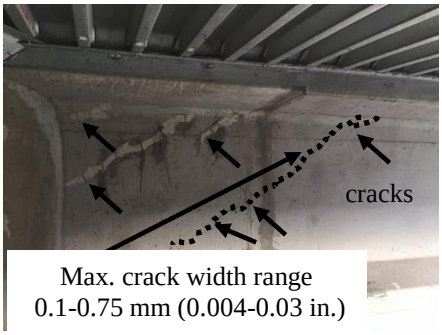

b) interior girder 2, North face

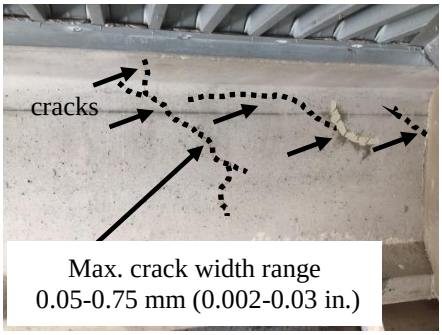

c) interior girder 3, South face

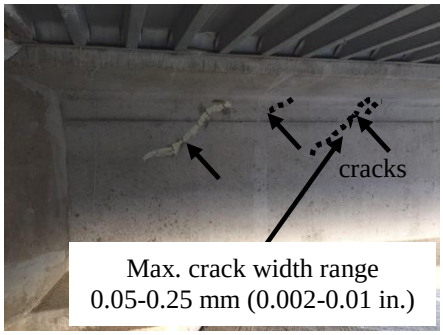

d) interior girder 3, North face

Figure 5.2 Crack maps in span 3

5.3 Experimental Program and Instrumentation

5.3.1 Instrumentation

Truck loading was applied to span three and two of the four girders in this span were instrumented with AE sensors (manufactured by MISTRAS Group, Inc., Princeton Junction, New Jersey). Two types of AE sensors were used; two were WDI (broadband) and fourteen were R6i (resonant), with an operating frequency range between 100 – 900 kHz and 40 – 100 kHz, respectively. Double bubble epoxy was used as a coupling agent to affix the sensors to the girders. All sensors were placed near the abutment of span 3 in the shear region/support areas surrounding the existing cracks in a general layout to cover the cracked areas. Eight sensors were attached on girder 2 (four sensors on each face) and eight sensors were attached on girder 3 (all on the south interior face). Figure 5.3 shows the AE sensor groups; the black circles refer to resonant sensors (e.g., 1R where the 'R' stands for resonant) and the black squares refer to broadband sensors (e.g., 6B where the 'B' stands for broadband). AE sensors were divided into groups named as shown in Table 5.2 and Figure 5.3. The overview of the sensor distribution is referenced in Figure 5.5 with different shapes, one shape for each sensor group. Two AE systems were used to collect the data including a Micro-II (8-channel) and DiSP (16-channel) system (both systems manufactured by MISTRAS Group, Inc., Princeton Junction, New Jersey). Strain transducers were also installed on the bottom flanges of all four girders in span three to guide the load test.

Table 5.2 AE sensor groups

Group number	Sensors numbers	Girder number	Girder face/Fig. 3
1	1R, 2R, 3R, 4R	Interior girder 2	South face/Fig. 3a
2	5R, 6B, 7B, 8R	Interior girder 2	North face/Fig. 3b
3	9R, 10R, 11R, 12R	Interior girder 3	South face/Fig. 3c
4	13R, 14R, 15R, 16R	Interior girder 3	South face/Fig. 3c

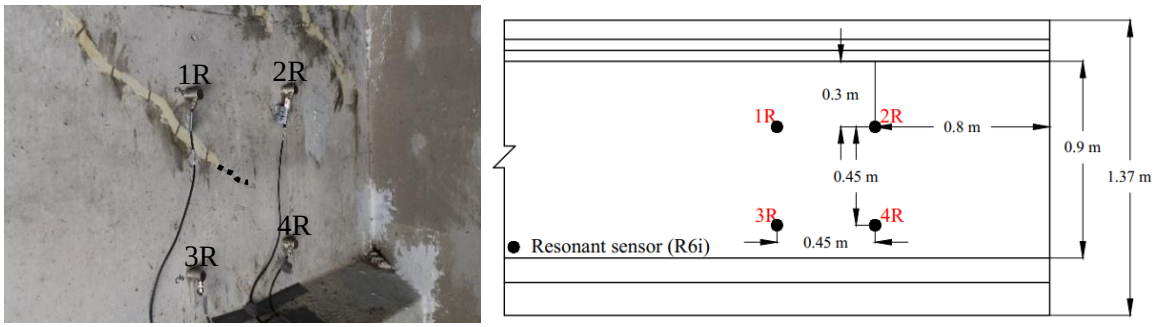

a) Girder 2-Group 1

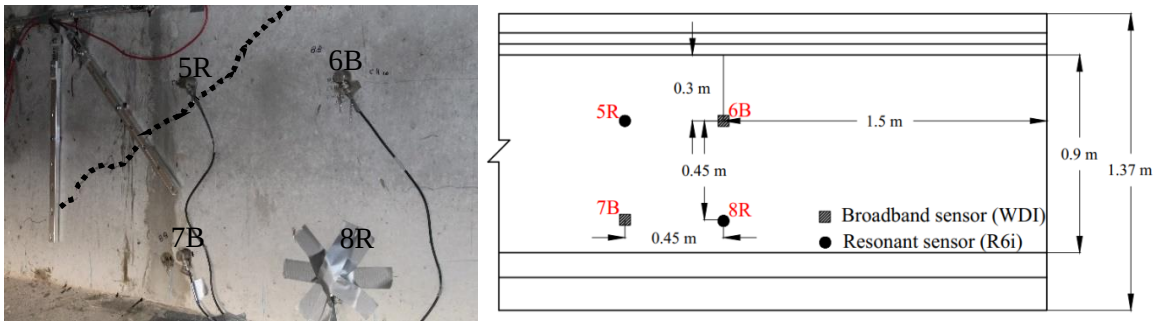

b) Girder 2-Group 2

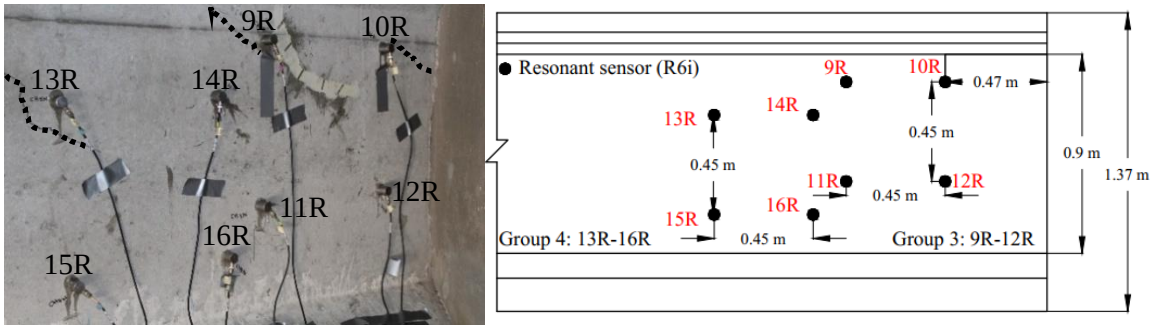

c) Girder 3-Groups 3 and 4

Metric (SI) conversion factors: 1 in. = 25.4 mm

Figure 5.3 Sensors groups

5.3.2 Load testing protocol

Two 9.14 m^3 (10 yd^3) trucks (71.2-kN (16-kip) front single axle, and 213.5-kN (48-kip) rear tandem axle, as shown in Figure 5.4) were used to load the bridge in ten load paths. The first five loading paths were applied in lane one (south driving lane) and paths six through ten were loaded in lane two (north driving lane). This manuscript focuses only

on loading paths over girder 2 and 3. Figure 5.5 shows sketches of the maximum loading paths on girders 2 and 3 respectively. The trucks were moved longitudinally in 1.52 m (5 ft) increments up to 10.6 m (35 ft), then to the final position of 15.2 m (50 ft) (the direction of loading is referenced by arrows in Figure 5.5). Single lane loading was simulated with one truck placed transversely at 3.34 m (10 ft-11.5 in) from the south barrier over interior girder 2 and two trucks placed back to back over the same girder (Figure 5.5a). This pattern was repeated for interior girder 3 (Figure 5.5b).

The response to the applied loads is affected by several factors including load type/distribution and boundary conditions. The bridge was designed based on the HS20-44 AASHTO LRFD-1996 truck loading, however, heavier loads are expected and allowed by NMDOT as shown in Table 5.3.

Table 5.3 Allowed moving load

No.	Permitted Bridge Moving Load	Max. truck weight, kN (kip)	Axle wheels weights, kip	Comment
1	Testing truck	284 (64)	16 24 24	Available at NMDOT
2	Design truck, HS 20-44	320 (72)	8 32 32	Design truck per AASHTO LRFD-1996
3	Overload truck 1	427 (96)	10 21.5 21.5 21.5 21.5	Historical overload
4	Overload truck 2	920 (207)	12 21.5 21.5 22 21.5 21.5 22 21.5 21.5 22	Historical overload
5	Sedan car	12-20 (2.8-4.5)	Based on car type	Regular traffic

For structural safety, careful preparations and structural analysis are required [27, 28]. Therefore, prior to testing, calculations were performed to determine that the bridge

would support the test trucks without exceeding the available moment and shear capacity. A simplified model of the bridge was created using RISA-2D structural analysis software [29]. Several truck loading cases were considered including an HS20 truck, a single test truck and two trucks back-to-back (applied during the actual test, see Figure 5.4), and historical overloads provided by NMDOT (see Table 5.3). Analysis results provided the maximum moments for each load case experienced over span three. The maximum moments were calculated at 40% of the span length [6.1 m (20 ft)] as this was the location where the strain transducers were placed during the load test. The available moment was found by subtracting the dead load moment from the cracking moment. The available strain for each girder, $\varepsilon_{available/girder}$, was then determined using equation 5.1 with single and multiple lane loading distribution factors, *DF*, provided by AASHTOWare Bridge Design and Rating software [30].

$$\varepsilon_{available/girder} = \varepsilon_{available} \times DF \qquad (5.1)$$

The available strain of 138 με resulted from this equation for interior girders was taken as the threshold during testing. Strains measured during the load test were closely monitored to not exceed the available strain. The maximum measured interior girder strains did not exceed the available strains making it unecessary to stop the loading before reaching the final positions (see Table 5.4). Further details for this criterion can be found in [31].

Table 5.4: Maximum measured strain at 40% of span length [32]

Load case	Maximum strain, με	
	Interior girder 2	Interior girder 3
One test truck	45	46
Two test trucks back-to-back	73	86

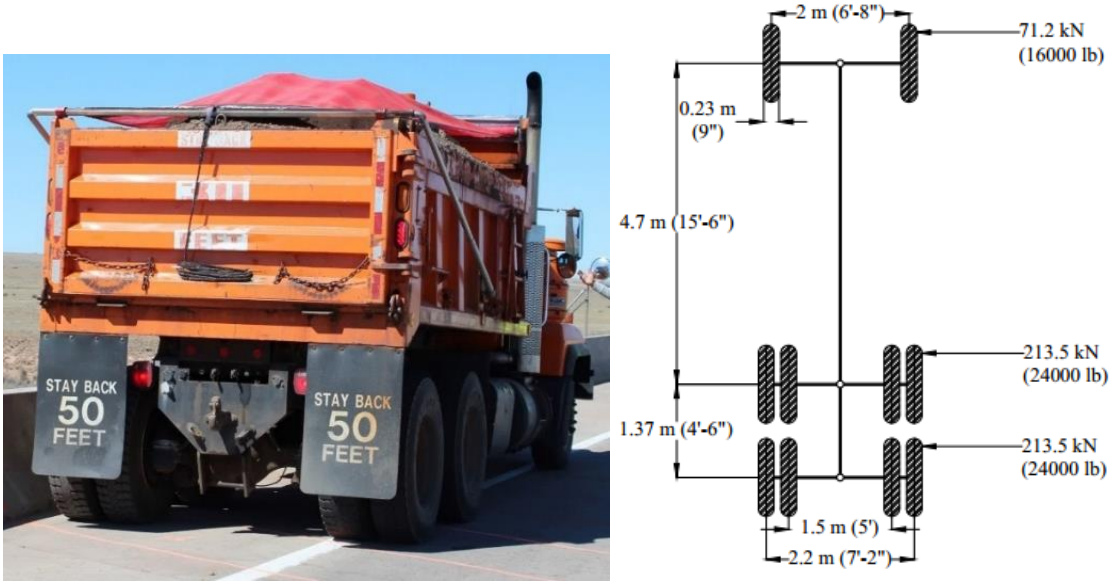

Figure 5.4 Dump truck axle spacing and weights

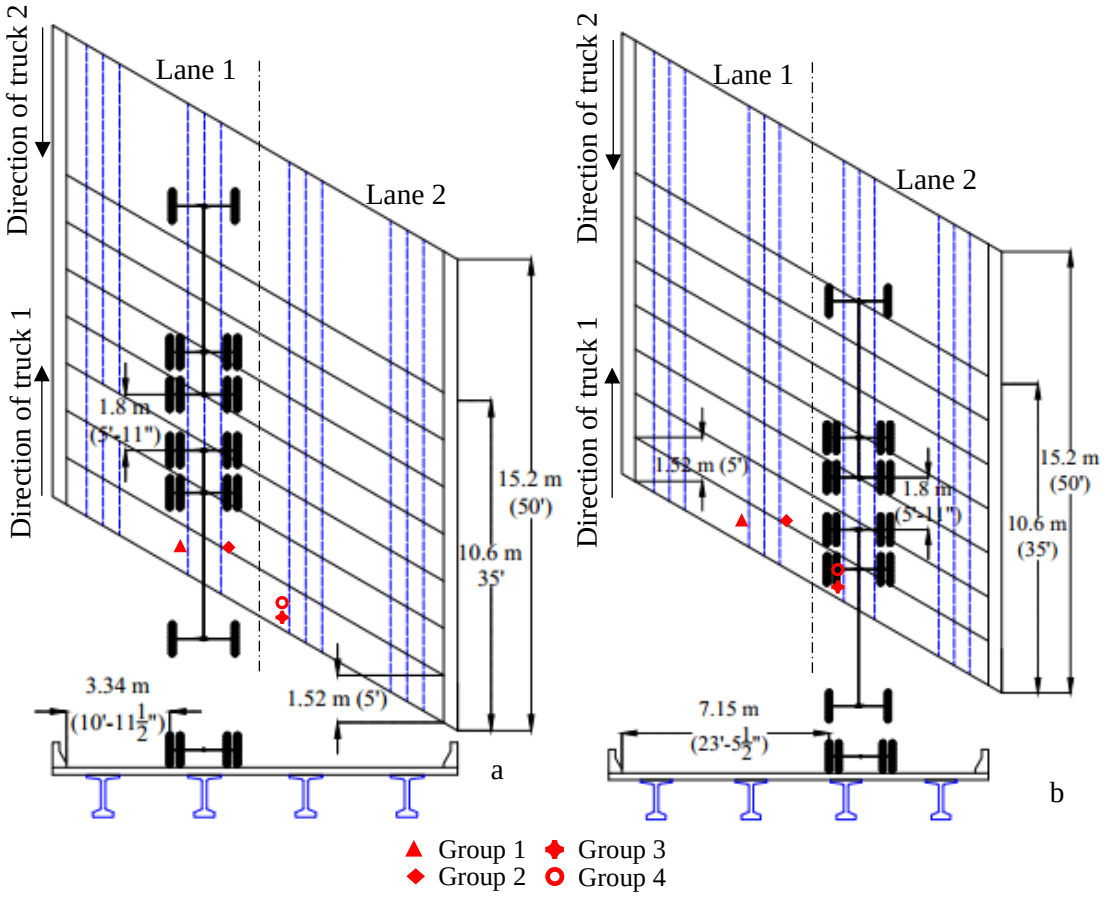

Figure 5.5 Two trucks back to back, a) on girder two, b) on girder three

5.4 Results and Discussion

5.4.1 Detection and Assessment of Active Crack Growth

Acoustic emission data was recorded and post-processed with AEwin software [33]. Results are discussed with respect to the maximum loading paths on interior girders 2 and 3. When the trucks were moved into position (referred to as 'loading'), AE signals with high signal strength were generally detected. When the trucks were parked to produce a desired effect (referred to as 'holding') the AE signal strength generally diminished with time. However, the rate of decay in the signals varied. Examples of one loading step and one holding step (highlighted regions) are shown in Figures 5.6-5.9. In these figures, only the data recorded when the rear axles reached the shear region is presented. The detection of visible (or nonvisible) crack growth is often related to AE signals having high signal strength and generally leading to sharp changes in the slope of the cumulative signal strength (CSS) curve [15, 34]. A relatively large number of high amplitude hits (i.e., amplitude exceeding 60 dB) and sharp changes in the slope of the CSS curve were observed in the AE data as the rear axles entered the shear region – potentially indicating the presence of crack initiation and extension (Figure 5.6 through Figure 5.9).

The level of AE activity was apparently affected by a previously applied injection of epoxy in the cracked girders. For example, more AE activity with higher signal strength was collected from sensors placed around a visible crack that had not been injected (Sensor Group 2, Figure 5.3b) than for a similar crack that had been injected (Sensor Group 1, Figure 5.3a), under the same load as shown in Figure 5.6. Prior investigators have speculated that sealing of cracks with epoxy injection may be effective in restoring the integrity of individual cracks [20]. Furthermore, under loading AE can be generated

through rubbing of the cracked surfaces [20], therefore friction between cracked surfaces and related AE may be affected by epoxy injection during loading.

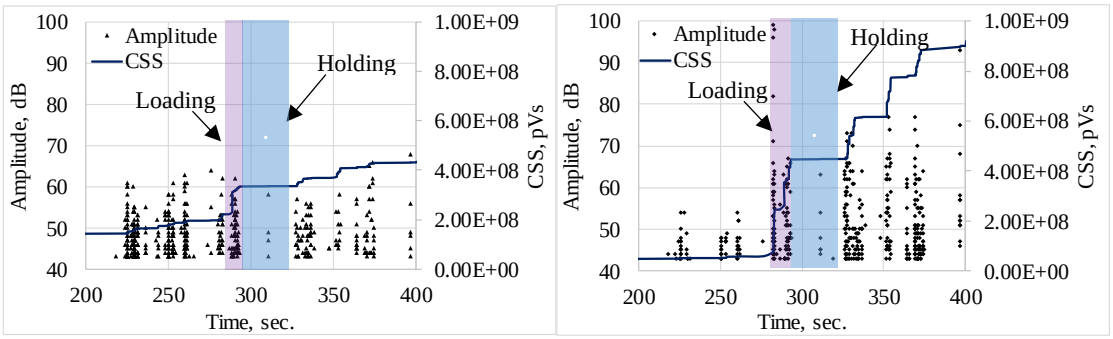

a) Sensor Group 1 – epoxy injected b) Sensor Group 2 – not epoxy

Figure 5.6 AE data activity for girder 2 (single truck)

The critical loading for all girders consisted of two trucks positioned back-to-back resulting in four axles near the abutment (shear area). All sensors recorded increased AE activity and slope changes in the CSS curve as the test continued (Figure 5.7). While the presence of epoxy injection affected the AE data for the case of a single truck, differences related to epoxy injection were less clear for two trucks back-to-back. This may indicate that epoxy injection is ineffective for more significant loading cases.

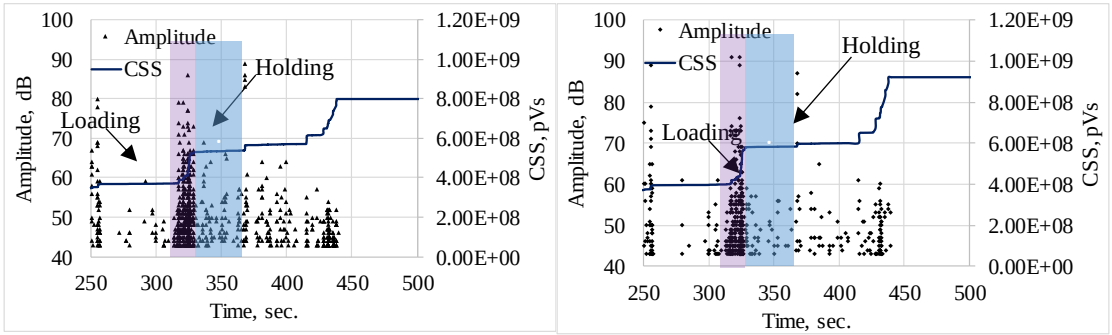

a) Sensor Group 1 – epoxy injected b) Sensor Group 2 – not epoxy injected

Figure 5.7 AE data activity for girder 2 (two trucks back-to-back)

Interior girder 3 was loaded the same as interior girder 2 (AE data is presented in Figures 5.8 and 5.9). Similar AE activity was collected from sensor Groups 3 and 4 as they

were installed close to the support and both groups surrounded existing cracks. A larger number of AE hits with higher signal strength was observed when two trucks were applied over interior girder 3 (Figure 5.9) when compared to one truck (Figure 5.8) when the rear axles entered the shear region.

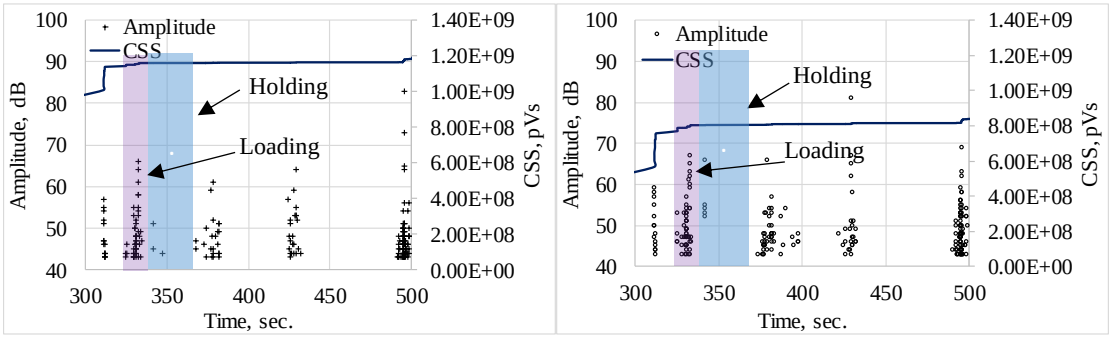

a) Sensor Group 3 b) Sensor Group 4

Figure 5.8 AE data activity for girder 3 (single truck)

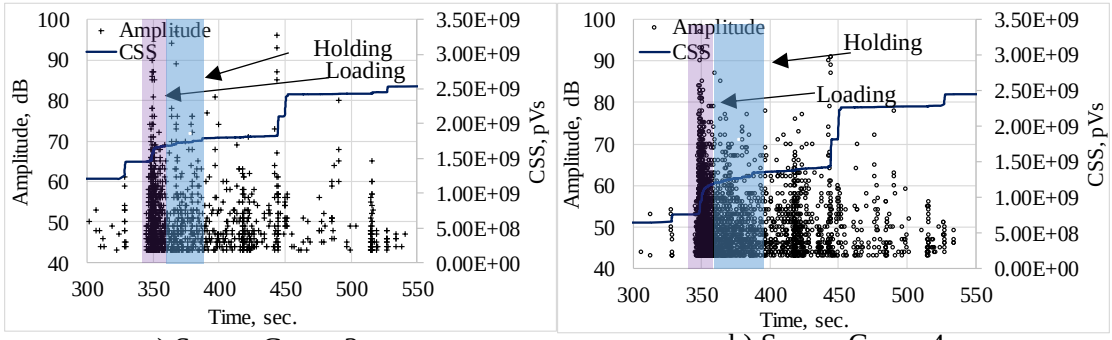

a) Sensor Group 3 b) Sensor Group 4

Figure 5.9 AE data activity for girder 3 (two trucks back-to-back)

When loadings were concentrated on interior girder 2, decaying AE activity in terms of numbers of hits and signal strength were observed during holding, suggestion minor progression of crack extension during the hold (Figures 5.6 and 5.7). However, loading with two trucks concentrated on interior girder 3 resulted in continuing AE activity during holding (Figure 5.9), indicating progression of crack extension during the holding period. This suggests unstable crack propagation and warrants further consideration.

A comparison of AE features was conducted between the loading and holding regions of interior girders 2 and 3 under the same load (two trucks back-to-back). Features investigated include amplitude, signal strength, rise time, and duration. Figures 5.10 and 5.11 indicate that amplitude, signal strength, and duration decay more dramatically for girder 2 than for girder 3, and the general trend noticed in the AE data during the hold for girder 3 warrants further consideration (for example long term monitoring of this region). The general decrease in rise time during the hold for both girders indicate that crack extension is more energetic during the loading phase.

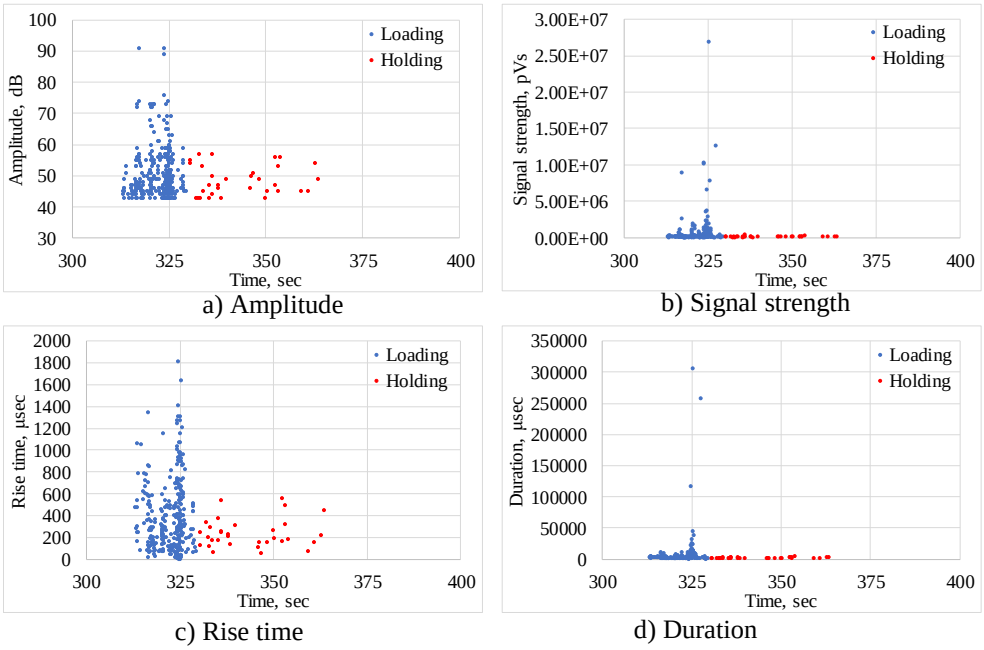

a) Amplitude b) Signal strength

c) Rise time d) Duration

Figure 5.10 AE data parameters for girder 2 (two trucks back-to-back)

5.4.2 Source localization of acoustic emission events

Source triangulation algorithms were utilized based on the time of flight feature in the AEwin software [33]. Wave speeds were determined on-site through 0.5 mm diameter pencil lead breaks conducted at different locations within the sensor grids. One challenge of on-site load testing with AE is controlling environmental noise including wind-born

debris, people walking, and tire friction in the case of a partially closed bridge. Therefore, background noise testing was collected prior to the actual load tests to establish an appropriate test threshold of 42 dB. The proper identification of wave reflections from cracks and structural boundaries is an important issue in source location. Source location of unfiltered data was first conducted and compared to the existing crack configurations to determine whether the results were reasonable and if filtering of the data was required. Source localization is challenging for a case such as the damaged girders described herein and very precise results are not expected. Rather, general trends in the data are of interest.

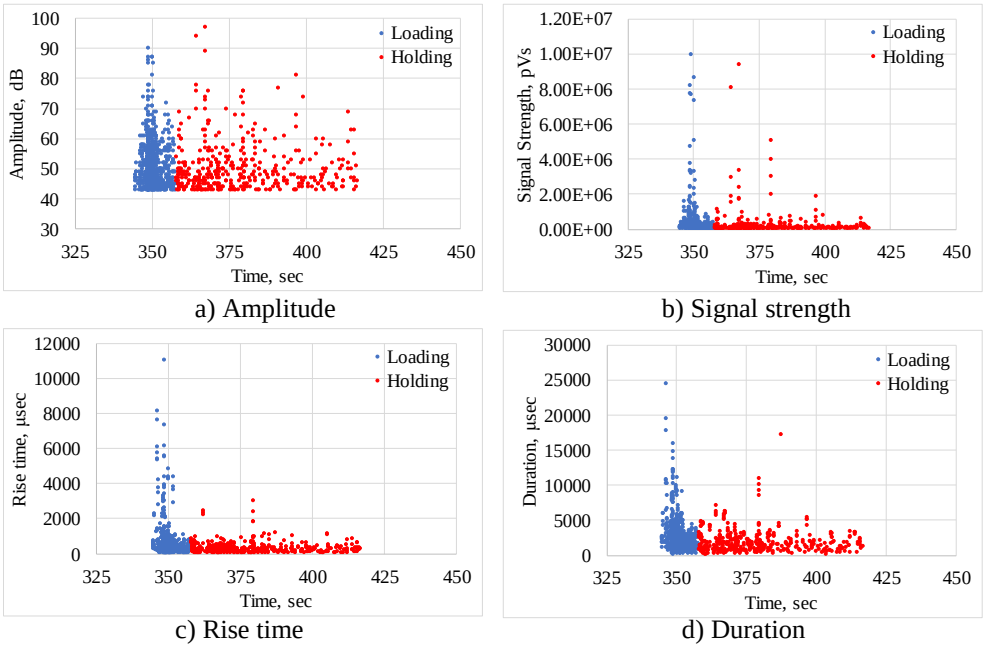

a) Amplitude b) Signal strength

c) Rise time d) Duration

Figure 5.11 AE data parameters for girder 3, two trucks back-to-back

Figure 5.12 shows the substantial amount of AE events collected during two trucks loading on girder 2 from each sensor group (detected during loading and holding). Figure 5.12a shows an inclined crack growth pattern between sensors 1R and 4R of interior girder 2, particularly away from the area of the previous epoxy injection. In Figure 5.12b, most AE events were observed to be near sensor 5R, where the visible cracks of interior girder

2 are located. The events recorded by all sensors suggest that the crack may also be progressing (or may have progressed) through the web of interior girder 2.

Under back-to-back loading on girder 3, Figure 5.13 shows source location events gathered from sensor groups 3 and 4 of girder 3 during loading and holding steps, some of which may be attributed to reflections. Figure 5.13a shows crack growth between sensors 9R and 10R on the top side of the girder web near the visible crack. Sensor 13R was also attached near a visible crack (Figure 5.13b). Many events were localized near sensor 13R and propagated on an incline toward sensor 16R.

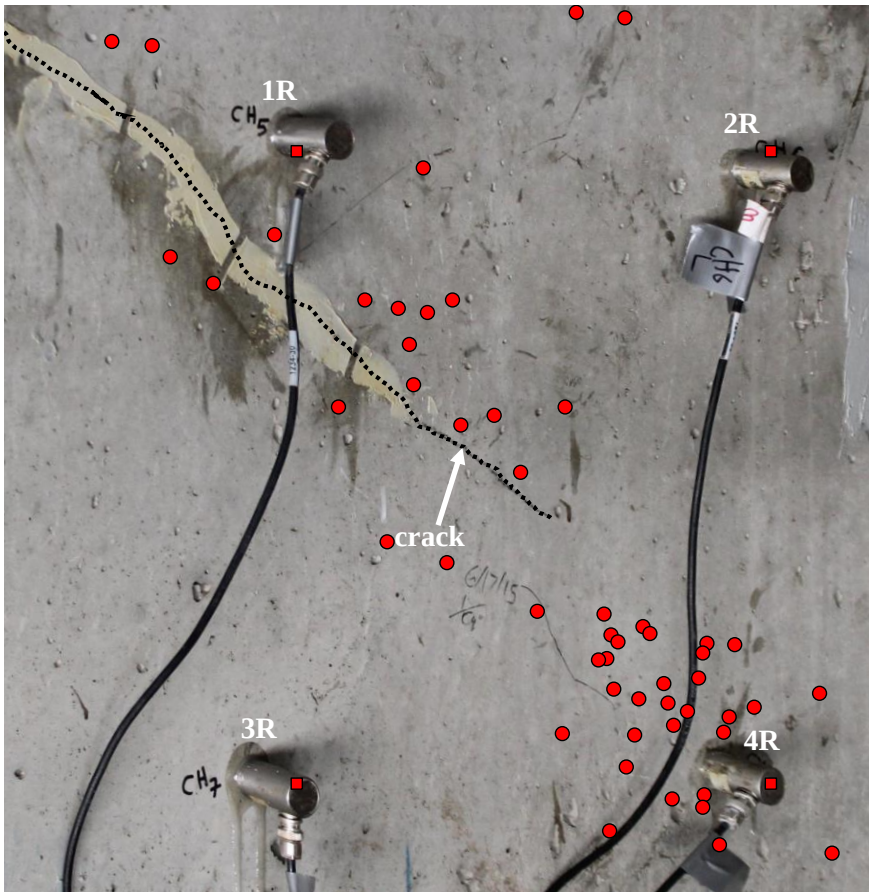

a) Sensor Group 1

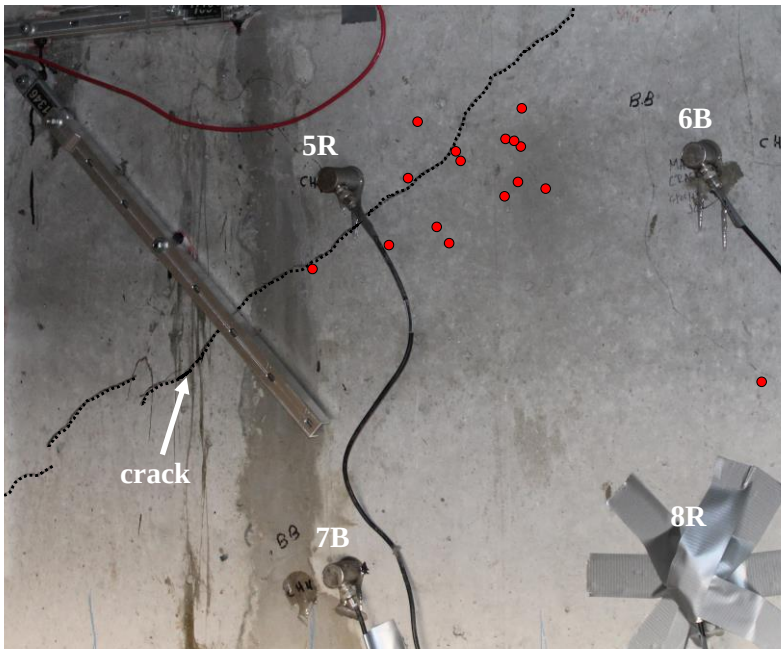

b) Sensor Group 2

Figure 5.12 AE source location for girder 2 during loading and holding, two trucks back-to-back

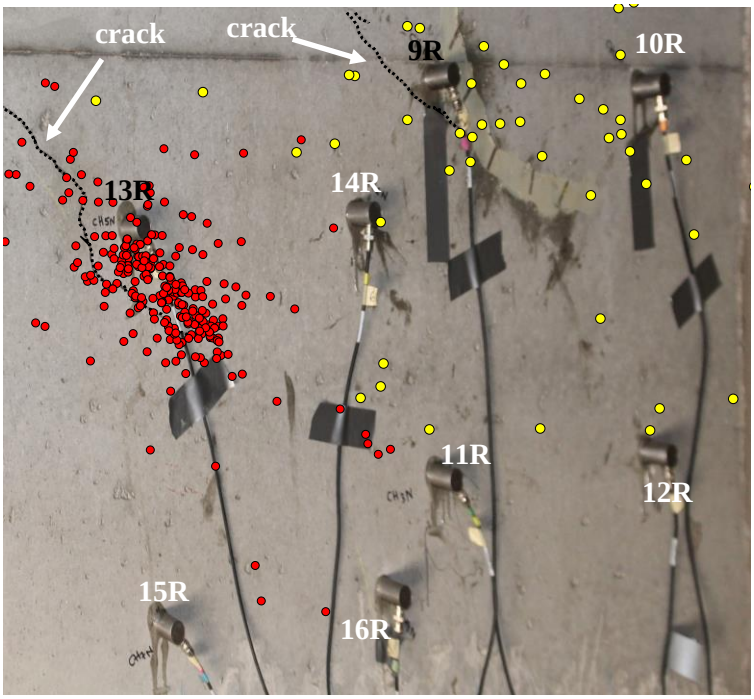

Legend: red dot - Sensor Group 4; yellow dot - Sensor group 3

Figure 5.13. AE source location for girder 3 during loading and holding, two trucks back-to-back

Source localization was also performed to investigate AE events during the highlighted holding regions shown in Figures 5.7 and 5.9 with two trucks back-to-back. Figure 5.14 shows that very few AE events were located during the holding period for interior girder 2. In contrast to this, for interior girder 3 a substantial number of AE events were detected and located during the load holding period, indicating crack extension and continuing damage as the load hold continued (Figures 5.14c and 5.14e).

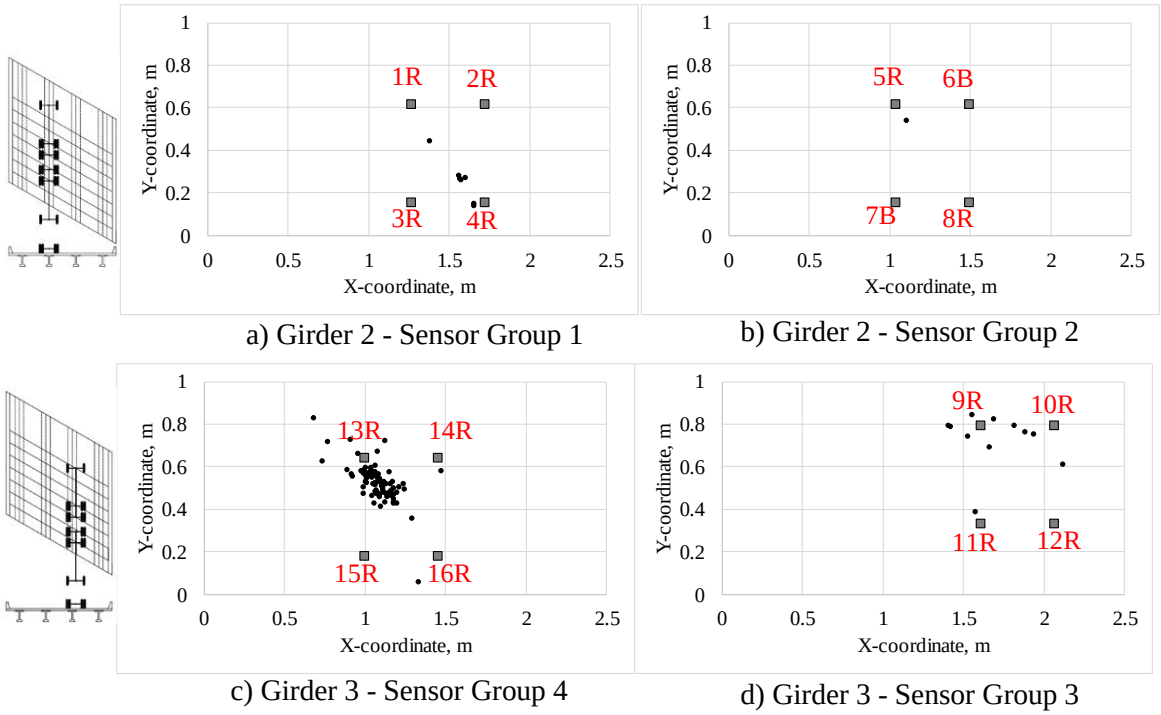

a) Girder 2 - Sensor Group 1

b) Girder 2 - Sensor Group 2

c) Girder 3 - Sensor Group 4

d) Girder 3 - Sensor Group 3

Figure 5.14 AE source location during load hold, two trucks back-to-back

5.4.3 Damage quantification using intensity analysis

Intensity analysis is a method originally developed to classify damage based on AE data in composite pressure vessels [35]. With this method, two parameters (historic index and severity) are calculated based on signal strength. Historic index, HI (t), given by Eq. 5.2a, is sensitive to the change in slope of the CSS curve with respect to time using a historical approach (ratio of the CSS of recent hits to the CSS from all hits). Severity (Sr)

is the average of the 50 events that have the highest signal strength given by Eq. 5.2b [19]. Tracking the changes of these two parameters over time provides an indication of the level of damage occurring in a structural element. The intensity analysis chart of AE activity is generated by plotting the severity values versus the maximum historic index (HI) [19]. Events related to increased damage plot toward the top right corner of the intensity analysis chart [1, 19]. Eqs. 5.2a and 5.2b for HI and severity are given below:

$$H(t) = \frac{N}{N-K} \frac{\sum_{i=K+1}^{N} S_{oi}}{\sum_{i=1}^{N} S_{oi}} \qquad (5.2a)$$

$$S_r = \frac{1}{50} \sum_{i=1}^{i=50} S_{oi} \qquad (5.2b)$$

where N = number of hits up to a specific time (t); S_{oi} = signal strength of the ith event; and K = the empirically derived constant that varies with the number of hits. The value for K that has been used in the literature is as follows [1, 15, 36]: (1) not applicable if $K = N \leq 50$; (2) $K = N - 30$ if $51 \leq N \leq 200$; (3) $K = 0.85N$ if $201 \leq N \leq 500$; and (4) $K = N - 75$ if $N \geq 501$.

The intensity analysis method was applied to evaluate the level of potential damage (i.e. crack growth) occurring in the shear region under the back-to-back truck paths over girders 2 and 3. Figure 5.15 shows that historic index and severity values approach the upper right corner of the charts indicating more damage for interior girder 3 in comparison to interior girder 2.

Historic index versus time was plotted for the critical load paths (two trucks back-to-back). Figure 5.16 shows that interior girder 3 had the highest historic index (numerical value of 16.2) and Table 5.4 shows the maximum values of the historic index for two trucks back-to-back. All loaded girders generally showed significant increases in the value of historic index when the rear wheels of a truck(s) entered the shear region as shown in the

highlighted regions in Figure 5.16. Interior girder 3 showed more damage (higher historic index) than interior girder 2, although interior girder 2 demonstrated more visible cracking.

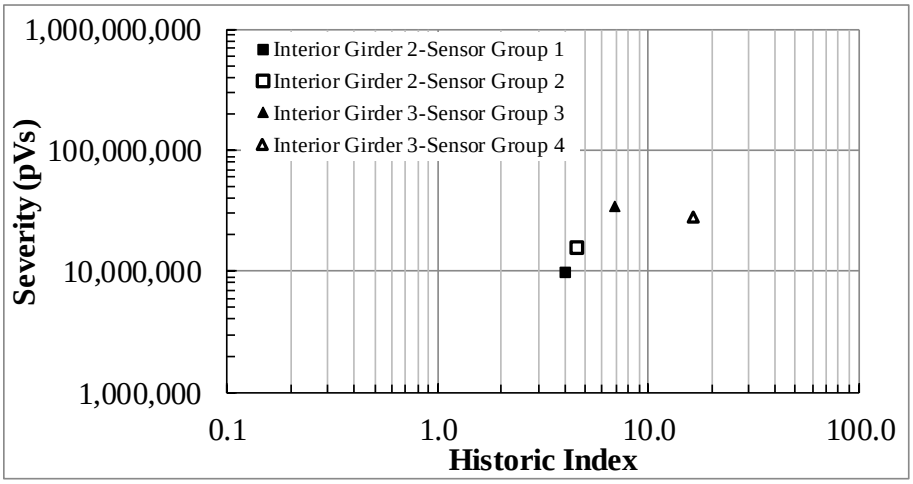

Figure 5.15 Intensity analysis for girders 2 and 3,
two trucks back-to-back, during loading and holding

As mentioned in the inspection report, the rating of the superstructure was 5 out of 9 (fair condition). To relate the AE data to the bridge condition, a rating method based on the historic index was developed for consideration (see Table 5.5). The basic idea is to expand the defect definitions given in the AASHTO Manual for Bridge Element Inspection (2013) for cracking of prestressed concrete members, particularly regarding crack propagation as opposed to the width of existing cracks. A proposed definition of each condition state is as follows: condition state 2 (fair) corresponds to a "crack that has self-arrested" while condition state 3 (poor) corresponds to an "identified crack that is not arrested but does not warrant structural review". It is implied that the state of cracking (i.e., self-arrested or not arrested) is determined using acoustic emission or another form of monitoring. For acoustic emission, in this case the condition states were most closely associated with historic index values recorded during loading and holding periods. Interior girder 3 was characterized as being in a more critical condition state (i.e., poor) as it has

higher HI values, and interior girder 2 was characterized as a less critical condition state (i.e., fair) (see Table 5.5). The continuing emission during a load hold, combined with a significant number of events located near an existing crack, stand out as potentially significant indicators for this girder that likely would not have been discovered in the absence of AE monitoring during the load test.

While this approach appears useful for the prestressed girders of the bridge under consideration, additional testing on similar bridges is needed to develop confidence in the approach.

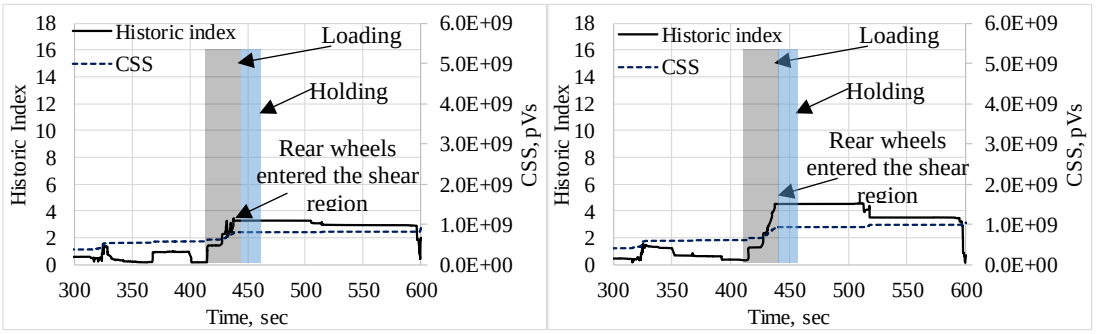

a) Interior girder 2-sensor group 1 b) Interior girder 2-sensor group 2

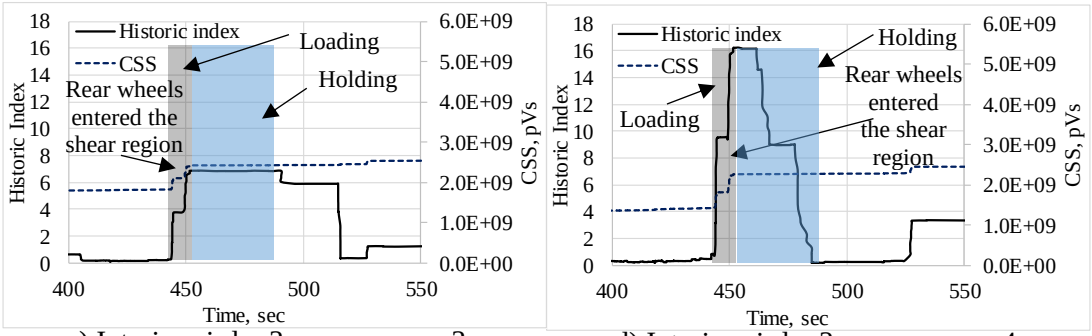

c) Interior girder 3-sensor group 3 d) Interior girder 3-sensor group 4

Figure 5.16 Historic index values, two trucks back-to-back

Table 5.5 Maximum values of historic index vs. condition state

Girder ID	Load	Sensor group	HI	Max. HI	Condition State	Description
Interior girder 2	Two trucks on girder 2	1	4.0	4.5	2 (Fair)	Crack that has self-arrested or has been arrested.
		2	4.5			
Interior girder 3	Two trucks on girder 3	3	6.9	16	3 (Poor)	Identified crack exists that is not arrested.
		4	16			

5.5 Shear strength evaluation of bridge girders

Shear strength evaluation of a BT-54 AASHTO girder was conducted to better understand how far the girders are from shear failure and under which load condition cracks are more likely to initiate and propagate. Percentages of applied shear to shear capacity due to vehicle loads allowed by NMDOT are discussed in this section. Results indicate that a crack is predicted to initiate under HS 20-44 truck loading and extend with increasing loading, which matches the observed conditions. Considerations for future action are discussed.

5.5.1 Methodology

Shear strength of a BT-54 AASHTO girder was predicted under vehicle loads allowed by NMDOT (see Table 5.3 and Figure 5.17) using the Response-2000 program developed at the University of Toronto by Evan C. Bentz [37]. The fundamental theory supporting the Response-2000 program is modified compression field theory (MCFT). Accuracy of the Response-2000 predictions has been verified with a database of 534 beams tested in shear including prestressed and reinforced sections, large footing-like sections, sections made with very high strength concrete and elements with unusual geometry [37].

First, the maximum shear force and moment of interior girders for the service and ultimate limit states were calculated at the critical section (h/2, where h is section height, specified by the AASHTO-LRFD Bridge Design Specifications, 1st edition [25]). Equation 5.3 and 5.4 show the corresponding load combinations.

$$Service\ load\ = 1.0\left(D + (LL + IM)\right) \quad (5.3)$$

$$Ultimate\ load\ = 1.25\ D + 1.4\ (LL + IM) \quad (5.4)$$

where *D* is dead load, *LL* is live load and *IM* is impact. The ultimate load cases were used to check the load effects induced by the passage of permitted overweight vehicles. In Table 6.A.4.5.4.2a-1 in the AASHTO Manual for Bridge Evaluation [26], the permit load factor equals 1.40 for special or limited crossings, single-trips, mixed with traffic, and the Annual Average Daily Traffic (ADTT) = 1000. This value is chosen based on the ADTT for the Vaughn Bridge which is approximately 750 (provided by NMDOT). The section dimensions, material properties, reinforcement details (Figure 5.18), and sectional loads (moment and shear) were then defined in the program.

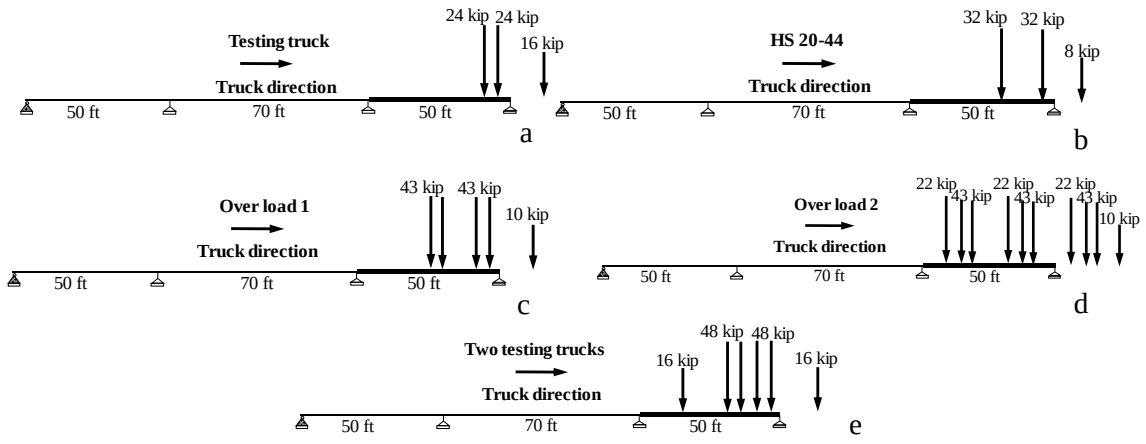

Metric (SI) conversion factors: 1 ft. = 0.0254 m, 1 kip = 4.448 kN

Figure 5.17 Load cases showing trucks positions causing maximum shear

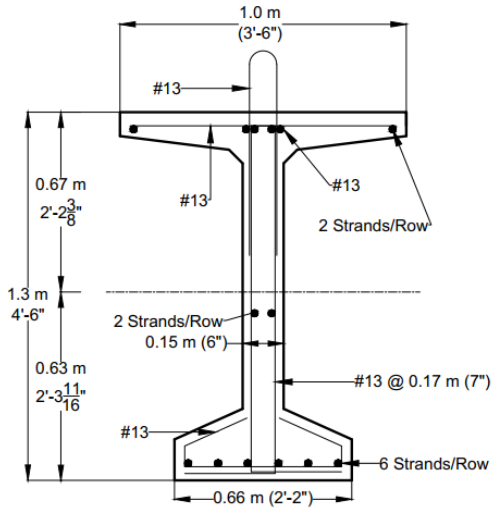

Figure 5.18 BT-54 AASHTO girder cross section details

5.5.2 Results and discussion

The calculated moment and shear under several load cases for the service and ultimate limit states are shown in Table 5.6. Figure 5.19 shows that the shear capacity (after application of the strength reduction factor of 0.9 based on AASHTO LRFD 2012, table 5.5.4.2.1) of the section is 1,136 kN (255.4 kip) which exceeds the applied shear for all service and ultimate load cases. The maximum shear force caused by the service condition of over load 2 and two test trucks back-to-back, and ultimate condition of over load 2 were about 51%, 55% and 70% of the shear capacity respectively.

The Response-2000 simulation considers that cracked reinforced concrete has a "smeared" tensile capacity. Figure 5.20 shows the principal tensile stress versus beam depth for the service load cases to evaluate the load level at which the cracks are expected to form. Once the principal tensile stress exceeds the maximum allowable tensile stress, the concrete is expected to crack. Figure 5.20a shows that under the service load condition of single test truck, crack initiation has not started; however, Figure 5.20b shows that crack

formation is imminent under HS 20-44 design truck loading. Therefore, heavier loads may lead to increases in cracking extension as illustrated in Figures 5.20c-5.20e, and as verified through visual inspection.

Table 5.6 Calculated moment and shear under different loading conditions

Load case	**Service load condition***		**Ultimate load condition***	
	Shear force, kN (kip)	Moment, kN.m (kip.ft)	Shear force, kN (kip)	Moment, kN.m (kip.ft)
Dead load + Testing truck	446 (100)	313 (231)	N/A	N/A
Dead load + HS 20-44 (design truck)	477 (107)	335 (247)	N/A	N/A
Dead load + Over load 1	545 (122)	381 (281)	731 (164)	511 (377)
Dead load + Over load 2	578 (130)	414 (306)	798 (179)	557 (411)
Dead load + Two testing trucks	629 (141)	439 (323)	N/A	N/A

*These values were calculated using equations 5.3 and 5.4

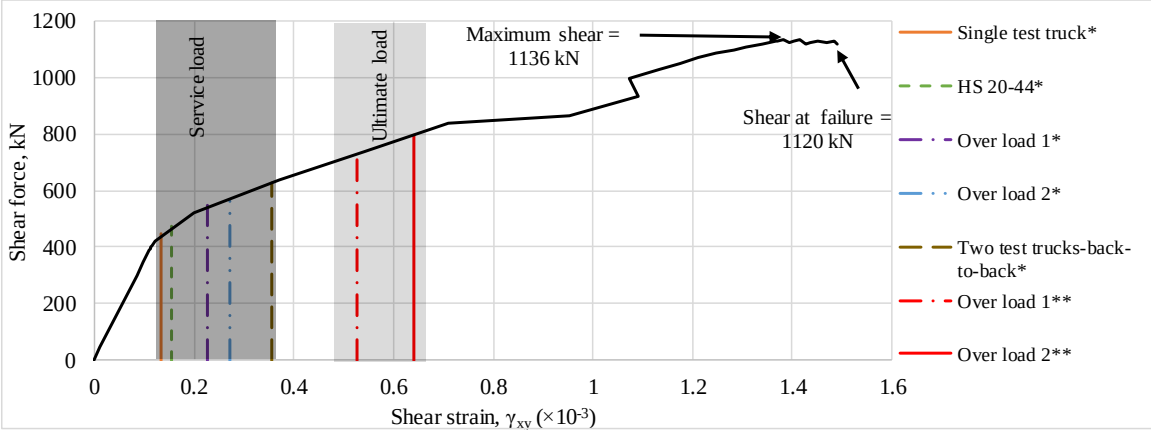

* Service condition, ** Ultimate condition

Figure 5.19 Shear force-shear strain response of the section under different load conditions

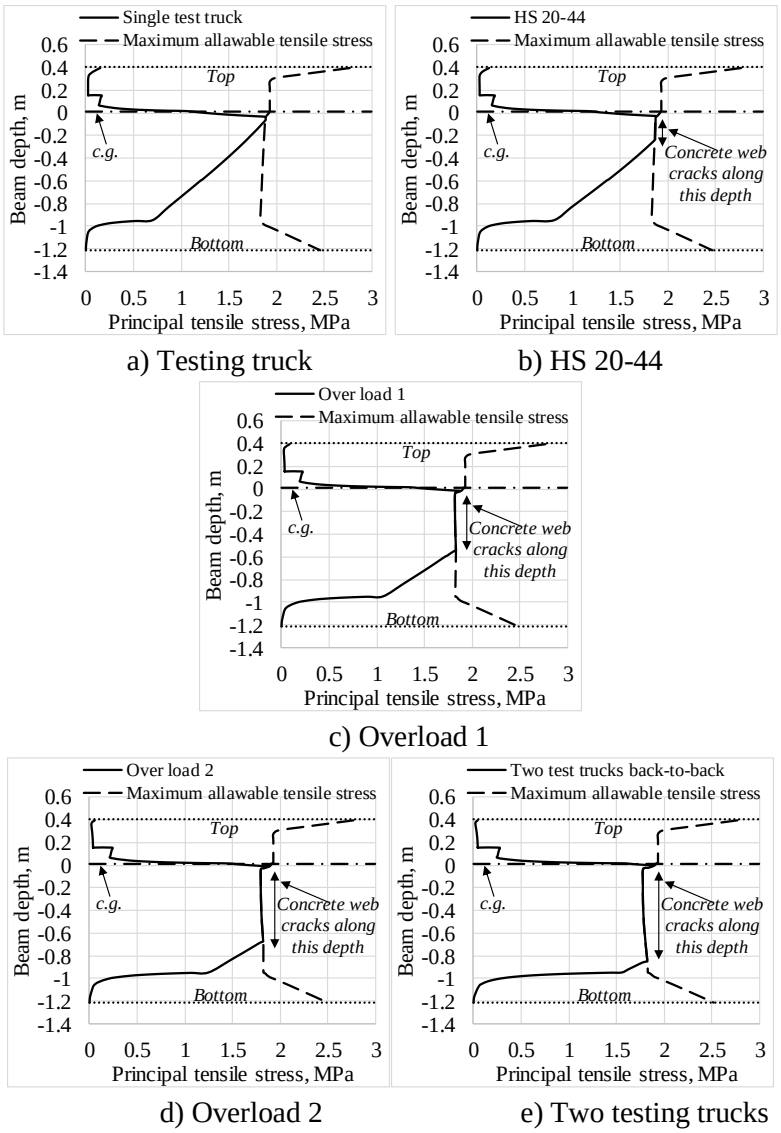

Figure 5.20 Principal tensile stress under service load cases

Based on the results discussed, AE provided insight into crack extension and classification which may be promising for structural health monitoring of existing structures having inclined cracks. Computational shear strength analysis provided additional insight and placed the test truck and other loads into context with regard to predicted shear failure.

5.6 Conclusion

This study demonstrates an application of load testing combined with an NDE technique (acoustic emission monitoring) to provide insight into the condition of an existing prestressed concrete BT-54 AASHTO girder bridge with pre-existing inclined cracks. A new damage characterization approach is discussed for classification based on acoustic emission data recorded during one loading and holding step. A key finding is that damage classification procedures provided an indication of unstable crack propagation in one girder during a load hold, warranting further consideration. Due to this finding, long-term monitoring may be considered to further evaluate crack growth under regular traffic loading to better understand the cause of further crack extension.

Primary conclusions are:

1. AE source localization algorithms were effective in data visualization (two-dimensional maps) that related to the visible crack profiles previously marked on the girders. In some cases, the crack extension was indicated in the acoustic emission data that was not visibly apparent.
2. To enable potential implementation of the findings, defect definitions based on those in the AASHTO Manual for Bridge Element Inspection were modified to incorporate acoustic emission data, arriving at a condition state of ‘poor’ for one girder, and ‘fair’ for the other.

5.7 Recommendations

1. Because the behavior of the bridge girders under actual traffic loading is likely to differ from the behavior observed during the load testing, it is recommended that

long-term acoustic emission monitoring be carried out over a period of one year. Due to the significant acoustic emission activity observed in girder 3, it is recommended that instrumentation be located primarily in the shear region of this girder.

2. For future load tests, it is recommended that crack opening gauges be installed in the shear areas for later correlation with acoustic emission data.
3. Further evaluation of the bridge girders is recommended in the future using short-term load testing under dump truck loading and long-term monitoring under actual traffic loading. Should the girders be strengthened in shear, it is recommended that the strengthened girders be monitored with acoustic emission during load testing to aid in assessing the effectiveness of the strengthening system.

5.8 References

[1] ElBatanouny, M. K., Ziehl, P. H., Larosche, A., Mangual, J., Matta, F., and Nanni, A., Acoustic emission monitoring for assessment of prestressed concrete beams." Construction and Building Materials, 58, (2014b) 46-53.

[2] Vidya Sagar, R., Raghu Prasad, B. K., and Sharma, R., Evaluation of damage in reinforced concrete bridge beams using acoustic emission technique, Nondestructive Testing and Evaluation, 27(2), (2012) 95-108.

[3] Schumacher, T., Higgins, C. C., and Lovejoy, S. C., Estimating operating load conditions on reinforced concrete highway bridges with b-value analysis from acoustic emission monitoring, Structural Health Monitoring, 10(1), (2011) 17-32.

[4] Shahidan, S., Pulin, R., Bunnori, N. M., and Holford, K. M., Damage classification in reinforced concrete beam by acoustic emission signal analysis, Construction and Building Materials, 45, (2013) 78-86.

[5] Tinkey, B. V., Fowler, T. J., & Klingner, R. E. (2002). Nondestructive testing of prestressed bridge girders with distributed damage (No. FHWA/TX-03/1857-2,).

[6] Hadzor, T. J., Barnes, R. W., Ziehl, P. H., Xu, J., & Schindler, A. K. (2011). Development of acoustic emission evaluation method for repaired

prestressed concrete bridge girders (Tech. Rep. No. FHWA/ALDOT 930-601-1). 238 Harbert Engineering Center. Auburn, AL, 36849.

[7] Cartz, L., Nondestructive Testing, ASM International.

[8] Küntz, M., Jolin, M., Bastien, J., Perez, F., and Hild, F., Digital image correlation analysis of crack behavior in a reinforced concrete beam during a load test, Canadian Journal of Civil Engineering, 33(11), (2006) 1418-1425.

[9] Yoneyama, S., Kitagawa, A., Iwata, S., Tani, K., and Kikuta, H., Bridge deflection measurement using digital image correlation, Experimental Techniques, 31(1), (2007) 34-40.

[10] De Silva, S., Mutsuyoshi, H., and Witchukreangkrai, E., Evaluation of shear crack width in I-shaped prestressed reinforced concrete beams, Journal of Advanced Concrete Technology, 6(3), (2008) 443-458.

[11] Zakaria, M., Ueda, T., Wu, Z., and Meng, L., Experimental investigation on shear cracking behavior in reinforced concrete beams with shear reinforcement, Journal of Advanced Concrete Technology, 7(1), (2009) 79-96.

[12] Jain, K., and Singh, B., Deformed steel fibres as minimum shear reinforcement—An investigation, In Structures, Vol. 7, (2016, August) 126-137.

[13] Ohno, K., and Ohtsu, M., Crack classification in concrete based on acoustic emission, Construction and Building Materials, 24(12), (2010) 2339-2346.

[14] ElBatanouny, M. K., Larosche, A., Mazzoleni, P., Ziehl, P. H., Matta, F., and Zappa, E., Identification of cracking mechanisms in scaled FRP reinforced concrete beams using acoustic emission, Experimental Mechanics, 54(1), (2014a) 69-82.

[15] Anay, R., Cortez, T. M., Jáuregui, D. V., ElBatanouny, M. K., and Ziehl, P., On-site acoustic-emission monitoring for assessment of a prestressed concrete double-tee-beam bridge without plans, Journal of Performance of Constructed Facilities, 30(4), (2015) 04015062.

[16] ASTM., Standard terminology for nondestructive examinations, ASTM E1316, West Conshohocken, PA., 2014.

[17] Olaszek, P., Swit, G., and Casas, J., Proof load testing supported by acoustic emission: an example of application, in: Bridge Maintenance, Safety, Management and Life-Cycle Optimization, Proceedings of the 5th International IABMAS Conf., Philadelphia, USA, 11-15 July 2010.

[18] Appalla, A., ElBatanouny, M. K., Velez, W., and Ziehl, P. (2015). Assessing corrosion damage in posttensioned concrete structures using acoustic emission. Journal of Materials in Civil Engineering, 28(2), 04015128.

[19] Golaski, L., Gebski, P., and Ono, K., Diagnostics of reinforced concrete bridges by acoustic emission." Journal of acoustic emission, 20, (2002) 83-89.

[20] Hadzor, T. J., Barnes, R. W., Ziehl, P. H., Xu, J., & Schindler, A. K. (2011). Development of acoustic emission evaluation method for repaired prestressed concrete bridge girders (Tech. Rep. No. FHWA/ALDOT 930-601-1). 238 Harbert Engineering Center. Auburn, AL, 36849.

[21] Świt, G. Acoustic Emission Method for Locating and Identifying Active Destructive Processes in Operating Facilities, Journal of Applied Sciences, 8(8), 1295, (2018) 1-20.

[22] Vecchio, F. J., and Collins, M. P., The modified compression-field theory for reinforced concrete elements subjected to shear, ACI J., 83(2), (1986) 219-231.

[23] AASHTO, AASHTO Manual for Bridge Element Inspection. 1st Edition, with 2015 and 2018 Interim Revisions. Washington, DC. 2013.

[24] ACI Committee, American Concrete Institute, and International Organization for Standardization. Building code requirements for structural concrete (ACI 318-14) and commentary. American Concrete Institute. 2014.

[25] AASHTO, AASHTO-LRFD Bridge Design. Washington, DC. 1996.

[26] American Association of State Highway and Transportation Officials (AASHTO). Manual for Bridge Evaluation, 2nd Edition, Washington, D.C. 2011.

[27] Lantsoght, E. O., Koekkoek, R. T., van der Veen, C., Hordijk, D. A., and de Boer, A., Pilot Proof-Load Test on Viaduct De Beek: Case Study, Journal of Bridge Engineering, 22(12), (2017a) 05017014.

[28] Lantsoght, E. O., van der Veen, C., Hordijk, D. A., and de Boer, A., Development of recommendations for proof load testing of reinforced concrete slab bridges, Engineering Structures, 152, (2017b) 202-210.

[29] RISA-2D version 16.0.1 [Computer software]. Foothill Ranch, CA, RISA Technologies Inc.

[30] AASHTOWARE BRR 6.7. [Computer software]. AASHTOWare Bridge Design and Rating software.

[31] Aguilar, C. V., Jáuregui, D. V., Newtson, C. M., Weldon, B. D., & Cortez, T. M. (2015). "Load rating a prestressed concrete double T-beam bridge without plans by field testing." Transportation Research Record, 2522(1), 90-99.

[32] Lane, A. M. (2018). “Investigation of Crack Propagation During a Load Test on a Prestressed Concrete Bridge Using Acoustic Emission Sensors and Strain Transducers.” Master Thesis, New Mexico State University.

[33] AEwin version E4.30 [Computer software]. Princeton Junction, NJ, Mistras Group.

[34] ElBatanouny, M., Larosche, A., Ziehl, P., and Yu, L., Wireless acoustic emission monitoring on in situ decommissioning for nuclear structures, 8th Int. Conf. on Nuclear Plant Instrumentation, Control, and Human-Machine Interface Technologies (NPIC & HMIT), 8. 2012.

[35] Fowler, T., Blessing, J., and Conlsk, P., New directions in testing, In AECM-3: International Symposium on Acoustic Emission from Composite Materials. 3rd, Paris, France (1989) 16-27.

[36] Nair, A. and Cai, C. S., Acoustic emission monitoring of bridges: Review and case studies.” Engineering structures, 32(6), (2010) 1704-1714.

[37] Bentz, E. C., Sectional analysis of reinforced concrete members. PhD dissertation. Toronto: University of Toronto. 2000.

Chapter 6

Summary and Conclusions

6.1 Summary

Common forms of deterioration, such as cracking, in concrete materials are caused by the heterogeneous nature of concrete, its low tensile strength, and severe environments. The condition of the existing structures can be addressed through employing active structural health monitoring (SHM) and maintenance strategies. SHM provides useful information regarding the ability of the structure to perform its planned function when imperative aging and degradation resulting from operational environments or extreme events are taken into consideration. Recent advances in technology provide several different solutions for monitoring and assessing the condition of a structure's system. Among those solutions is acoustic emission (AE), a passive NDT technique that has the potential to detect and quantify internal damage growth at the microscale level in real time. Due to the high sensitivity of AE sensors, cracks can be detected long before they are visible. Moreover, under increasing loads, this method provides the capability to effectively monitor the internal condition of a structure and can potentially assist in establishing safe load limits.

This study focuses on addressing current gaps associated with AE monitoring in two ways. AE provides an ability to develop a methodology for detecting and classifying micro and macro cracks in cement-based materials and enables us to understand the direction from which they initiate and in which direction they expand. This is imperative for long-term assessments of concrete and reinforced concrete structures used in nuclear waste disposal systems. The second methodology that may be developed through the use of AE is the evaluation of the condition of pre-cracked structure elements. This is due to the ability to extrapolate results collected from load tests with which future damage may

be predicted. This application establishes the suitability of AE monitoring for field conditions and provides further insight for potential complications.

In the first study, AE monitoring during compressive loading was employed to investigate microcrack formation and coalescence in cement paste specimens having dimensions of 38.1mm × 38.1mm × 152.4mm (1.5 inch × 1.5 inch × 6 inches). Two sensors were attached on all faces except for the front face, which had two additional sensors as guard sensors for AE noise filtering. The specimens were loaded at different levels while AE data was recorded. Active crack growth was detected and classified using the AE parameters amplitude and cumulative signal strength. Three stages of crack behavior were observed; initiation of micro-cracking (non-visible crack stage); stable crack growth (one to two-inch crack length stage); and unstable cracking (three to six-inch crack length stage). Moreover, unsupervised pattern recognition approaches were investigated to separate AE data into clusters and assign a damage mechanism to each cluster. In addition, micro-CT scanning was employed to investigate the dimensional extent of micro-cracking and to correlate the images with AE data.

In the second study, theoretical predictions on crack propagation were made based on fracture mechanics approaches and the finite element method in conjunction with experimental observations to identify the correlation between damage mechanisms defined in the first study and AE activity. The fracture toughness of cement paste was determined using the two parameter fracture model based on the experimental results of a three-point bending test. Stress intensity factor (SIF) of mode I, KI, was calculated using the finite element model and compared to its critical value or fracture toughness to define the stage at which a crack grows in an unstable manner. The results showed that KI passed the FT

of cement paste when unstable crack propagation was observed based on AE data analysis, while it was less than the FT when the first visible crack was initiated and propagated in a stable manner.

The third study sumarizes the results of AE monitoring to evaluate the condition of a three-span, prestressed concrete girder bridge located in Guadalupe County, New Mexico during a load test. The 15-year-old bridge has inclined cracks in four girders of the exterior spans. Some cracks were injected with epoxy, however, most of the cracks extend beyond the epoxy regions, and some girders have developed new cracks. AE data was collected from sensors attached on two girders toward the obtuse corner of an exterior span under different levels of load. AE data analysis and a source location algorithm were applied to assess the response of the structure under load increases and during load holds. The results showed signs of crack propagation beyond the existing cracks and indicated that interior girder 3 experienced more damage accumulation during load testing than interior girder 2. Shear strength analysis using modified compression field theory (MCFT) was performed to place the results in context

6.2 Conclusions of Each Study

Several conclusions can be drawn from each of the studies.

6.2.1 Identification of damage mechanisms in cement paste based on acoustic emission

This study summarizes an experimental approach to detect and classify active crack growth in cement paste specimens. AE data was utilized to guide the investigations and the additional insight was provided by micro-CT scanning at differing levels of ultimate capacity. Conclusions are as follows:

- AE signal parameters such as amplitude and cumulative signal strength were useful for correlation of mechanical damage and AE activity. Abrupt increases in both parameters correlated to the occurrence of significant damage in the specimens.
- Cumulative signal strength was a valuable parameter for understanding crack initiation and progression. Based on changes in the slope of the cumulative signal strength curve, three different mechanisms were defined and assigned. Those were 1) microcrack initiation and formation, 2) extension of microcracks, and 3) unstable crack extension and coalescence.
- Unsupervised pattern recognition showed to be suitable techniques to aid in discrimination between the AE data based on relationships between signal subset features. The AE data was separated into three signal subsets and fracture mechanisms were then assigned.
- Time of occurrence and statistical criteria were beneficial for assigning potential mechanisms to the signal subsets because different damage mechanisms are more likely to occur in specific time intervals.
- Unstable crack formation and the propagation of micro-cracks was assigned to two signal subsets concentrated near the end of the loading, while micro-crack initiation and formation was assigned to the signal subset distributed throughout the test period for the B80 and B100 specimens.
- Micro-crack coalescence was assigned to a signal subset occured near the end loading, while micro-crack initiation was assigned to signal subsets distributed throughout the test period of B60. Substantiation of these mechanisms was

provided through images obtained through micro-CT scanning, showing only internal micro-cracks distributed along the specimen length.

Finally, the findings were in line with the expectations, however, more tests should be conducted (e.g. three specimens per loading level) to generate more data and observe the signal properties.

6.2.2 Experimental and theoretical investigation of fracture properties of cement paste prisms under compression

In this study, fracture mechanics approaches, including the two-parameter fracture model by Jenq and Shah [18] and the finite element method in conjunction with experimental observations, were utilized to identify the correlation between damage mechnisims and AE activity defined in the previous work [1]. The stress intensity factor (SIF) was calculated and compared to its critical value, fracture toughness (FT) to define the stage at which a crack grows in an unstable manner. Conclusions are as follows:

- The fracture mechanics approach and the finite element method in conjunction with experimental observations are effective tools to better describe the behavior of cementitious materials under compression.
- Microcrack initiation and extension defined by AE parameters analysis was verified since the stress intensity factor of mode I was less than the fracture toughness of cement paste (stable crack growth).
- Unstable crack propagation defined based on AE data was also verified since the stress intensity factor of mode I passed the fracture toughness value.
- This work shows that AE and the fracture mechanics approach are complementary methods to characterise damage sites in cement-based materials.

Finally, since the proposed strategy was applied on specimens loaded in compression, future research could include testing in tension while monitoring with AE.

6.2.3 On-site acoustic emission monotoring for assessment of a prestressed concrete BT-54 AASHTO girder bridge

This study demonstrates an application of load testing combined with an NDE technique (acoustic emission monitoring) to provide insight into the condition of an existing prestressed concrete BT-54 AASHTO girder bridge with pre-existing inclined cracks. A new damage characterization approach is discussed for classification based on acoustic emission data recorded during one loading and holding step. A key finding is that damage classification procedures provided an indication of unstable crack propagation in one girder during a load hold, warranting further consideration. Due to this finding, long-term monitoring may be considered to further evaluate crack growth under regular traffic loading to better understand the cause of further crack extension.

Primary conclusions are:

- AE source localization algorithms were effective in data visualization (two-dimensional maps) that related to the visible crack profiles previously marked on the girders. In some cases, the crack extension was indicated in the acoustic emission data that was not visibly apparent.
- To enable potential implementation of the findings, defect definitions based on those in the AASHTO Manual for Bridge Element Inspection were modified to incorporate acoustic emission data, arriving at a condition state of ‘poor’ for one girder, and ‘fair’ for the other.

APPENDIX A

COPYRIGHT PERMISSION